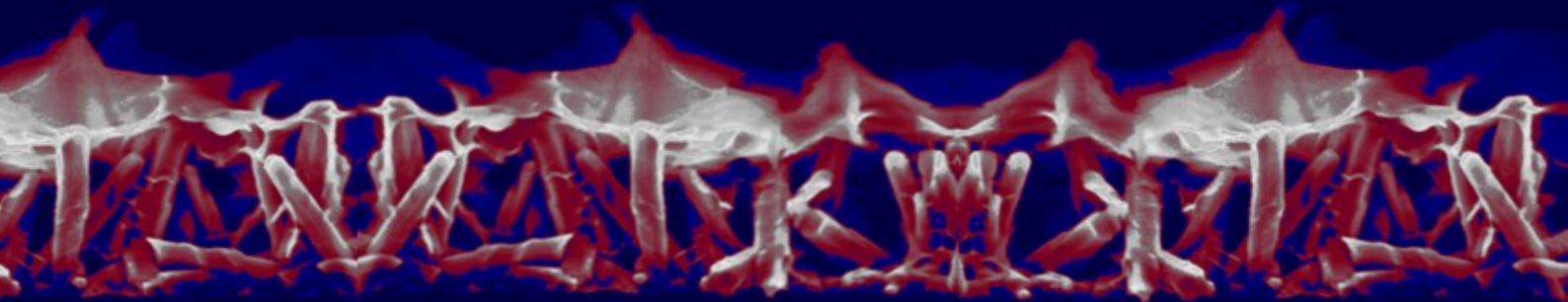**UNIVERSITÀ DEGLI STUDI DI CATANIA**

Dottorato di Ricerca in Scienza e Tecnologia dei Materiali - XXVIII ciclo

Vincenzina Strano

Low-cost ZnO nanostructures:

controlled synthesis and applications

Tutor: Prof.ssa M. G. Grimaldi
Supervisor: Dr. S. Mirabella
Coordinatore: Prof.ssa M.G. Grimaldi

UNIVERSITÀ DEGLI STUDI DI CATANIA

Dottorato di Ricerca in Scienza e Tecnologia dei Materiali - XXVIII ciclo

Vincenzina Strano

Low-cost ZnO nanostructures: controlled synthesis and applications

Tutor: Prof.ssa M. G. Grimaldi

Supervisor: Dr. S. Mirabella

Coordinatore: Prof.ssa M.G. Grimaldi

Tesi per il conseguimento del titolo

To my family

Cover

False colored SEM image in cross view of ZnO NWL/NR, a novel combined nanostructures obtained by chemical bath deposition with ZnO NWLs grown on top of ZnO NRs. More details can be found within the Summary of this thesis.

Low-cost ZnO nanostructures: controlled synthesis and applications

Vincenzina Strano

Ph.D. Thesis, University of Catania

Printed in Catania, December 2015

All have their worth and each contributes to the worth of the others.

from *The Silmarillion*

J. R. R. Tolkien

Contents

Introduction

Advances in nanotechnology is strongly dependent on research innovative nanostructured materials in nanostructure form. Multifunctional metal oxides have recently emerged as smart materials with a wide range of controllable properties leading to innovative device concepts. In particular, zinc oxide (ZnO) presents an unique combination of interesting properties such as non-toxicity, wide band-gap, high exciton binding energy at room temperature, piezoelectric behavior, high physical, chemical and mechanical stabilities [1]. Research on ZnO is an old story. In 1957, the New Jersey Zinc Company published a book entitled "Zinc Oxide Rediscovered" to promote the material's properties worthy to be further investigated [2]. Since then, ZnO have gained growing importance in the material science. In the last decade, ZnO nanostructures have been the focus of intensive studies, being an almost ideal systems both from a fundamental point of view (ease of nanostructuration, energy band bending, intrinsic and extrinsic defects, combination of polar and non-polar planes, …) and from the applications (energy harvesting devices, sensors, biomedical devices, lighting, …). Many methods, both physical and chemical, have been employed for the synthesis of nanostructured ZnO; however most of the synthesis methods involve expensive experimental set up and sophisticated equipment. One of the basic requirements for nanomaterials to become industrially viable is the low production cost alongside the possibility to supply large amount of non-toxic material. In this regard, wet-chemical synthesis approaches are very appealing, having the advantages of easy use, low cost, reduced process temperatures and potential for scaling up. On the other hand, these kinds of synthesis have the shortcoming of lack of a good control and reproducibly. Overcoming these limitations and ensuring a high degree of reliability represent important challenges for modern material science. Among the wet-chemical approaches, chemical bath deposition (CBD) has emerged as the

simplest and more versatile method for the synthesis of ZnO nanostructures. It is a chemical process, similar to an electroless deposition of solid phase from an aqueous solution. In this thesis, the attention is reserved to ZnO nanorods (NRs) and nanowalls (NWLs). ZnO NRs grown by CBD are among the most promising semiconducting nanostructures currently investigated for a wide range of applications. ZnO NWLs represent a new form of nanostructure with very large surface area, easy to synthesize by CBD on Al-covered substrate. Currently, some investigations have been focused on the microscopic mechanisms leading to the formation of ZnO NRs and NWLs, however some outstanding issues remain to be solved. A clearer comprehension of the growth mechanism in CBD and a better control of the synthesis are fundamental issues for taking full advantage of this technique. The work described in this thesis aims to deeper understand the mechanisms underlying the formation of ZnO NRs and NWLs under CBD conditions, attempting to clarify the role of synthetic parameters. Discerning their effects leads to enhance the control over the growth process. The potentialities of ZnO NRs and NWLs with optimized morphologies as critical components in technological solar cell, photocatalysis and sensing applications are also investigated.

The thesis is organized as follows:

The first chapter is devoted to a review of the basic physical properties of ZnO and its nanostructuration. A brief selection of the different promising applications of ZnO nanostructures is reported followed by detailed description of some chemical and physical approaches for the synthesis of ZnO nanostructures. In particular, a survey of the literature about the low-cost chemical bath deposition of ZnO nanorods and nanowalls is presented.

In the second chapter, a systematic investigation of the chemical bath deposition of ZnO NRs using an aqueous solution with zinc nitrate salt and hexamethylenetetramine (HMTA) is presented. An optimized procedure for reproducible synthesis and the growth kinetics are presented and discussed. In addition, an empirical study is reported evidencing the double

role of HMTA in the NRs growth mechanism. HMTA is shown to participate both as a supplier of OH^- ions and as a capping agent promoting the anisotropic growth. These two actions are not mutually exclusive, and the amount of HMTA in solution determines the key process variable. This result contributes as a step towards a better control of CBD synthesis.

In the third chapter the light scattering effects from ZnO NRs grown by CBD on flat and transparent substrate are examined, giving particular emphasis to forward light scattering efficiencies. ZnO NRs with different morphological features showed an high efficiency in forward diffusion of visible light. By analyzing and modeling the light scattering performances, a threshold in NRs length ($\sim 1\mu$) was identified over which the light scattering effect is enhanced. The applicability of ZnO NRs film as low-cost light diffuser layer upon crystalline silicon (c-Si) solar cell is also presented. An enhancement of the light-current conversion efficiency has been achieved for wavelengths longer than 600 nm, attributable to the scattering of light by NRs array.

The fourth chapter presents the main results about the synthesis and application of ZnO NWLs. In particular, the effects of the solution composition, pH, concentration of $Al(OH)_4^-$ and growth time on the quality of ZnO NWL films grown by CBD are examined. A prior oxidation of Al substrate is proposed as a new, easy and inexpensive route for enhancing the quality of ZnO NWLs. A self-screening model has been developed to explain the growth kinetics of ZnO NWLs. The promising results of ZnO NWLs as pH sensing material and as photocatalyst substrate are finally shown.

Chapter 1

ZnO: Properties, Synthesis and Applications

Low-dimensional ZnO structures have recently attracted more and more interest in scientific research. In the last years, ZnO nanowires and nanorods have been defined as the most representative one-dimensional nanostructures, together with silicon nanowires and carbon nanotubes. Indeed, the number of publications and the cross-referenced areas based on ZnO nanostructures are as large and important as literature in quantum computing, carbon nanotube, semiconductor thin films, and dark matter [3]. The reasons of this great interest can be also ascribed to the ease of growing nanostructures with noticeable performances and in a large number of intriguing shapes.

In this chapter the basic physical properties of ZnO are described. Then, a brief selection of the different promising applications of ZnO nanostructures is reported followed by detailed description of some chemical and physical approaches for the synthesis of ZnO nanostructures, with particular attention to low-cost chemical deposition of ZnO nanorods and nanowalls.

1.1   Fundamentals of ZnO

Zinc oxide (ZnO) is a II-VI inorganic semiconductor, relatively abundant in nature as mineral *zincite* and it is widely used in various industrial products as summarized in Figure 1.1 [1].

ZnO has been investigated as semiconductor material since the 1930s [4]. Between the beginning of the eighties and mid-nineties, the research on ZnO suffered a setback, partially due to the difficulty to achieve a robust *p*-type doping. Furthermore, at that time, the interest was directed to III-V semiconductors whose ambipolar doping and nanostructuring were already easy to obtain [5]. Conversely, in the last 20 years, ZnO has experienced a renewed interest in scientific research pushed by its great versatility in terms of synthesis methods for epitaxial layers and nanostructures and for related potential applications.
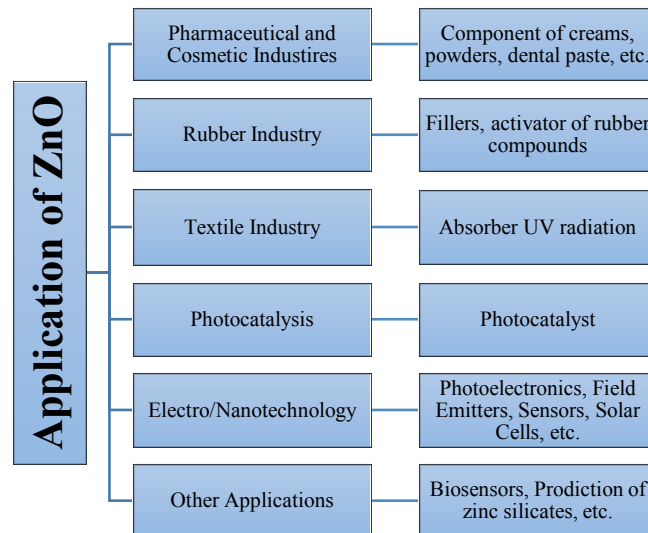
Figure 1.1: Industrial applications of ZnO. Scheme adapted from ref [1].

The new era for ZnO started in the field of optoelectronics, fueled by the impressive progress in developing efficient short wavelength emitters based on wide band-gap semiconductors. GaN based structures were the focus of

many work since GaN *p-n* junctions showed favorable performance as blue/UV diodes and lasers [6]. The need to find high quality, closely lattice matched substrate for GaN, stimulated the research on ZnO that provides a close match in addition to the possibility to grow large bulk single crystal [7]. Thereafter, not only the versatility of ZnO was revaluated but also new potentialities were defined [5, 8, 9].
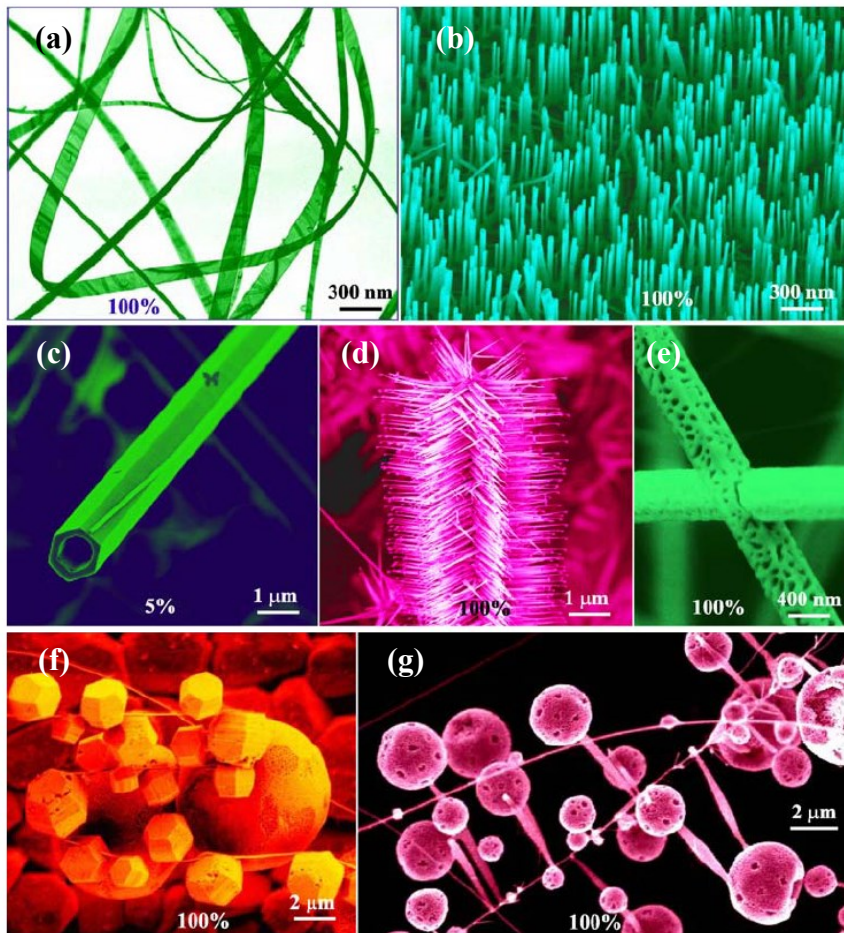
Figure 1.2: A collection of ZnO nanostructures: (a) nanobelt; (b) aligned nanowire arrays; (c) nanotubes; (d) array of propellers; (e) mesoporous nanowires; (f) cages and shell structures; and (g) hierarchical shell and propeller structure. The percentage in each figure indicates the purity of the as-synthesized sample for the specific nanostructure. Adapted from ref [10].

7

One of the most intriguing aspect of ZnO is the possibility to easily grow many different nanoscale forms. Figure 1.2 (a-g) reports a collection of ZnO nanostructures: nanobelt (NBs), aligned nanowires (NWs) and nanorods (NRs), nanotubes (NTs), nanopropellers, porous NRs and hierarchical nanostructures. Current research has been focused on these nano and micro scale structures, representing the fundamental building blocks of the modern physical science and engineering. The reduction in size provides the opportunity of developing new generation devices compared to conventional bulk materials. Table 1.1 lists several physical properties of wurtzite ZnO, most of which are pertinent also to low dimensional material, though it is know that the nanostructuring leads to effects - quantum confinement effect and enhanced surface states- affecting some important properties such as quantum transport and enhanced radiative recombination of carriers [11-14].

Properties	Value
Lattice Constant (300 K)	a=3.250 Å; c=5.207 Å
Density	5.606 g/cm^3
Melting Point	2248 K
Refractive index	2.008, 2.029
Band Gap Energy	3.44 eV - 3.37 eV
Exciton Binding Energy	60 meV
Effective Mass	0.24 (electron); 0.59 (hole)
Mobility	100-200 cm^2/Vs (electron); 5-50 cm^2/Vs (hole)

Table1.1: Physical and structural properties of wurtzite ZnO.

1.1.1 Crystallographic Properties of ZnO

Under ambient conditions, the crystal structure of ZnO is preferentially the hexagonal wurtzite with lattice parameters a=3.250 Å and c=5.207 Å [15] in which each Zn anion is surrounded by four O ions at the corners of a tetrahedron, and vice versa (Figure 1.3(a)).
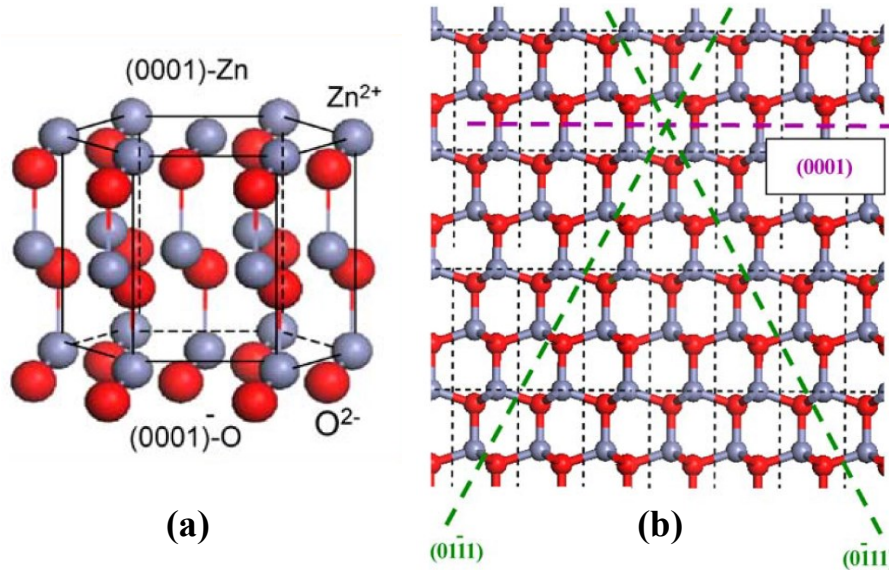
Figure 1.3: (a) Wurtzite Structure of ZnO. O atoms are shown as red spheres, Zn atoms as grey spheres. The unit cell is identified by black lines. (b) The projected structure of ZnO along *a*-axis, showing the $\{0001\}$ and $\{0\bar{1}11\}$ polar surfaces. Adapted from [10].

It is worth noting that for hexagonal crystals, four-indices (*hkil*) system, is used to indicate the crystallographic planes and direction, instead of usual three-indices (*hkl*) Miller notation. The index *i* is given by the $h+k+i=0$. This four-axis representation is called Miller-Bravais and it takes into account the crystal symmetry of hexagonal structure, avoiding that crystallographic equivalent planes are indicated with dissimilar indices. The tetrahedral coordination is typical of *sp³* covalent bonding nature, however ZnO, as the other II-VI compounds, has a strong ionic characteristic as demonstrated by its ionicity f_i=0.616, border value between covalent and ionic semiconductor [12]. This fraction of ionic binding is responsible for the large gap between the conduction and valence bands (ZnO energy bandgap E_g=3.44 eV, at low temperature) [5].

ZnO can also crystallize in cubic zinc blende, a metastable phase that can be made stable only by heteroepitaxial growth on cubic substrates,

9

and in rocksalt structure, high-pressure metastable phase [16]. All the crystalline forms of ZnO exhibits crystallographic polarity which contributes to many properties of ZnO, as piezoelectricity, and affects the growth mechanisms and the defect generation. In wurtzite ZnO structure, along the <0001> direction (*c*-axis), there is an alternation of Zn-terminated (0001) and O-terminated (000$\bar{1}$) polar planes. The {10$\bar{1}$1} planes of wurtzite ZnO are another group of polar planes with higher surface energy (see Figure 1.3(b)). Other common crystal faces terminations are the non-polar (11$\bar{2}$0) and (10$\bar{1}$0), both containing the same number of Zn and O atoms. Figure 1.4(a-c) reports some typical growth morphologies of ZnO one-dimensional (1D) nanostructures in which the non-polar planes (01$\bar{1}$0) and (2$\bar{1}$$\bar{1}$0) results maximized because of their lower surface energies. On the other hand, introducing planar defects parallel to the polar faces allows to grow structures dominated by polar surfaces, as in the case of nanobelt shown in Figure 1.4(d).
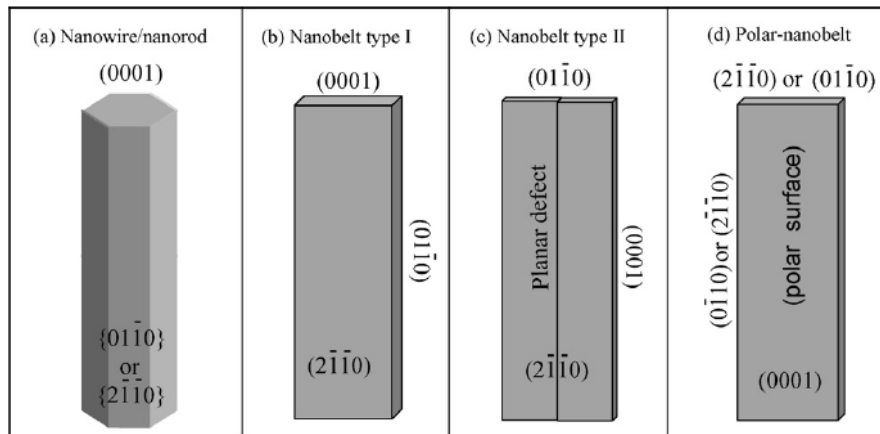

Figure 1.4: Typical growth morphologies of one-dimensional ZnO nanostructures and the corresponding facets [3].

10

1.1.2   Band Structure and Optical Properties

A precise knowledge of the band structure is crucial for understanding the potential applications of a semiconductor. Consequently, many studies, both theoretical and experimental ones, were devoted to calculate the band structure of ZnO [17-22]. The bottom of the conduction band (CB) is formed by the 4s levels of Zn^{2+} and the top of the valence band (VB) by O^{2-} 2p and Zn^{2+} 3d states. The early attempts to theoretically determine the electronic band structure ruled out the effects of Zn 3d states, considering them as core level, and the results were not in good agreement whit the experimental data. In 1995 a novel approach was proposed, consisting in incorporating an atomic self-interaction correction into usual local density approximation (LDA) [20]. The calculations, reported in Figure 1.5, showed that the maximum of VB and the minimum of CB energy values were obtained at Γ point k =0, which confirmed that ZnO is a direct band gap semiconductor.
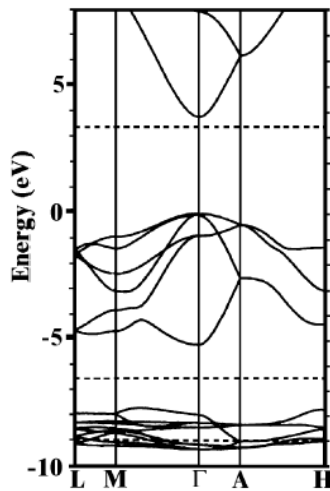
Figure 1.5: LDA bulk band structure of ZnO as calculated by using the self-interaction correction. The horizontal dashed lines indicate the measured gap energy and d-band width [20].

11

Moreover, the calculated value of the energy gap was 3.77 eV and it is the closest to the experimental one (E_g=3.37 eV at room temperature, [23]) until then. As mentioned above, such wide and direct bandgap of ZnO enables promising application in blue/UV range photonics as well as the large exciton binding energy (~60 meV) [7, 24] indicates an efficient excitonic emission even at room temperature (RT).

Typical room-temperature (RT) photoluminescence (PL) spectrum of ZnO consists of a UV emission band and, eventually, a broad visible emission band, as shown in Figure 1.6. Most of works suggested that the UV emission at RT originates from the radiative recombination of excitons [25-27], while some authors proposed that such emission can also contains the contributions related to unspecified localized state [28] and to the free-to-bound transitions [29].
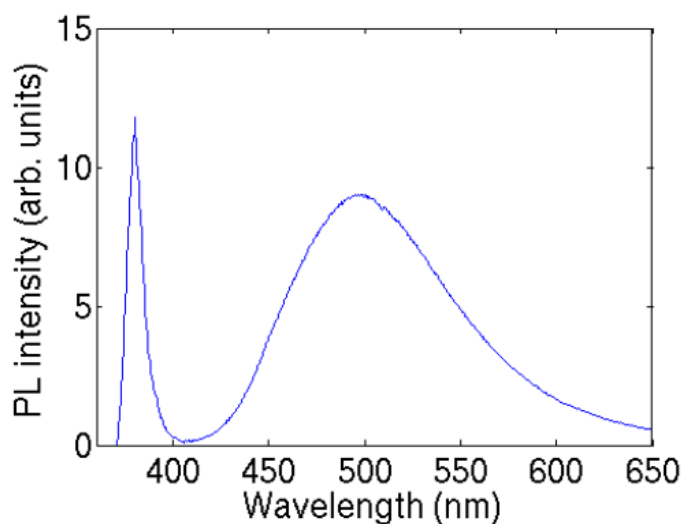
Figure 1.6: A typical room temperature PL spectrum of ZnO nanowires grown on a Si substrate using the vapor liquid solid technique at 890 ℃ [30].

The broader emission observed in the visible region of the spectrum is generally ascribed to impurities and different intrinsic defects, such as oxygen vacancies (V_o), zinc vacancies (V_{Zn}), zinc interstitials (Zn_i) and

oxygen interstitials (O_i). This visible band emission is, in particular, a typical optical feature of ZnO nanostructures. Shalish et al., analyzing the PL spectra of ZnO NWs grown by high temperature (~1000°C) chemical vapor deposition (CVD), demonstrated that this deep-level luminescence is mainly due to electronic states close to the surface. As a consequence, the reduction of the nanostructures size leads to an increase of the relative intensity of this emission. Figure 1.7 reports the PL spectra and scanning electron microscopy (SEM) images of the ZnO NWs with different diameters. The ratio between the UV and visible luminescence peak intensities changes with the size of the nanowires.
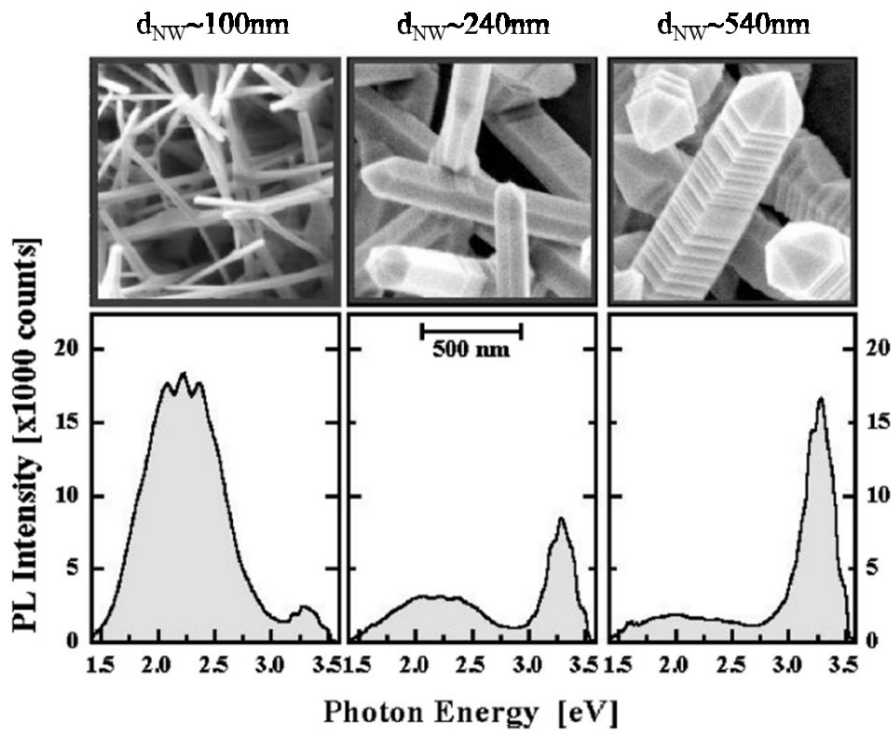
Figure 1.7: Photoluminescence spectra and related SEM images obtained from ZnO NWs grown by CVD with different diameter (d_{NW}). Adapted from [31].

However, the exact identity of the defects responsible for the visible emission band is still unclear and widely debated. Moreover, some variation

13

of the position of the UV peak was observed for different shaped nanostructures, as illustrated in Figure 1.8 [32]. One possible explanation for this variation may be the difference in surface-to-volume ratio entailing different defects concentration (defect density on the surface is higher than in the bulk [33]).
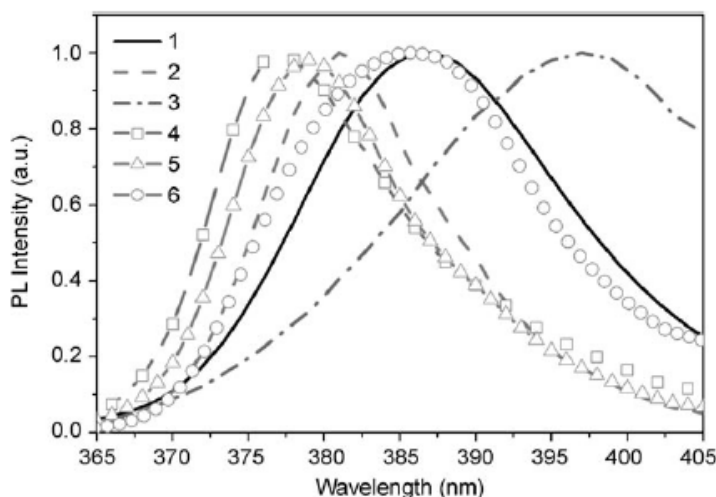
Figure 1.8: RT PL spectra in the UV range for different nanostructures: (1) Tetrapods, (2) Needles, (3) Nanorods, (4) Shells, (5) Highly faceted NRs, (6) Ribbons. Adapted from [32].

1.1.3   Electric and Piezoelectric Properties

As-grown ZnO shows *n*-type conductivity. For long time, the causes for this unintentional *n*-type doping were attributed to the presence of native defects as V_o or Zn_i [34,35]. However, more recent works have claimed that neither oxygen vacancies nor other point defects can contribute to *n*-type conductivity [8, 36]. In particular, several theoretical calculations, corroborated by experimental evidences, have shown that V_o is a deep level defect state (DLS) [37,38] and thus it cannot significantly contribute to *n*-type conductivity. Moreover, Kohan et al. [39] showed that theoretically both V_o and Zn_i have high formation energies in *n*-type ZnO. Further studies

14

proved that the inclusion of substitutional H (much more stable than interstitial H), acting as a shallow donor, is main responsible of the unintentional *n*-type doping. [40,41].

The electrical properties of ZnO, in terms of carrier concentration and mobility, are closely correlated to the method used to synthesize the material. The room-temperature electron mobility for bulk and thin film ZnO are in the range of 100-200 cm^2/Vs [42, 43], typically measured by Hall effect analysis. These values are close to the theoretical value of ~300 cm^2/Vs estimated by Monte Carlo simulations for the room temperature electron mobility of ZnO [44]. Electrical transport measurements were also performed on individual ZnO nanowires and nanorods [45]. Park et al. [46] reported on fabrication and electrical characteristics of high-mobility field-effect transistors (FETs) using a single ZnO nanorod, Figure 1.9, measuring an electron mobility of 75 cm^2/Vs.
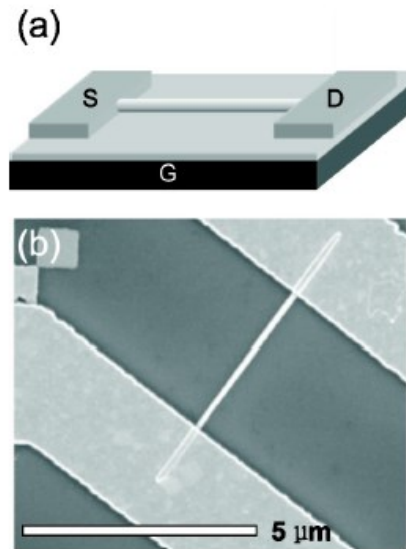

Figure 1.9: (a) Schematic and (b) SEM image of ZnO NR FET device [46].

The effect of surface states on the electron transport was eliminated by coating with polyimide known for the effective passivation effect in bipolar technology. After polyimide deposition, the field effect mobility of ZnO NR

FET was highly increased to 120-3100 cm^2/Vs with mean value of 680 cm^2/Vs [46]. These results indicate that the ZnO nanostructure based devices can have higher performance than their thin film counterpart. Although as-grown ZnO is *n*-type material, intentional *n*-type doping is required to increase the carrier concentration in view of electronic device applications. Al, Ga and In are the most common donor dopants for ZnO, giving rise to transparent conductive oxides (TCO) commonly employed in a large number of devices [47]. One of the major hindrance for fully exploiting ZnO in electronic and photonics technology is the difficulty of achieving a stable and reproducible *p*-type doping [8, 16]. Beyond the tendency toward *n*-type conductivity, the compensating effect from intrinsic defects and the small number of candidate for shallow acceptor represent severe limitations for *p*-doping of ZnO [8].

ZnO exhibit also a large electromechanical response caused by the lack of a center of symmetry in the unit cell. By exerting an external pressure, a lattice distortion is induced and the center of the negative charges will no longer coincide with the center of the positive charge, generating an electric dipole. The mechanism is outlined in Figure 1.10.
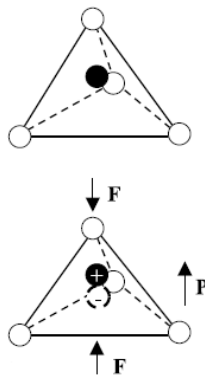
Figure 1.10: Schematics showing piezoelectric effect in tetrahedrally coordinated cation-anion unit [10].

An important parameter evaluating piezoelectric performance is the d_{33} piezoelectric coefficient. For ZnO the d_{33} value is about 9.9 pC/N for a bulk and 12.4 pC/N for an oriented film [48, 49] but these value can be improved by doping with transition metals atoms [50, 51]. Therefore, ZnO, especially

16

in nanostructural formats, has been used for building micromechanical devices, such as sensor, actuators and nanogenerators.

1.2   Applications of ZnO Nanostructures

The present renaissance of the scientific interest for ZnO is based on the wide range of promising applications in a large number of emerging areas. Several examples of energy harvesting and sensing devices based on ZnO nanostructures are briefly reported below.

1.2.1   Energy Harvesting Devices

The semiconducting and piezoelectric dual properties of ZnO may be exploited for applications in mechanical-energy conversion or in electrical power generation by solar cells. A shining example of electromechanical application of ZnO nanostructures is in piezoelectric nanogenerator [52]. By using zinc oxide nanowires arrays it has been possible to convert nanoscale mechanical energy into electrical energy (Figure 1.11). The aligned NWs are deflected with a conductive atomic force microscope tip in contact mode. The bending creates a strain field which causes, for piezoelectric effect, an electric field across the nanowires. This effect can be used in different application as in the case of wireless devices devoted to *in situ*, real-time biomedical monitoring and detection. Such devices should be self-powered and not dependent on a battery. Compared to conventional transducers based on piezoelectric thin films, the nanostructures not only might improve the general device performances (critical strain, flexibility, sensibility, operative lifetime) but also reduce the size of integrated nanosystem.
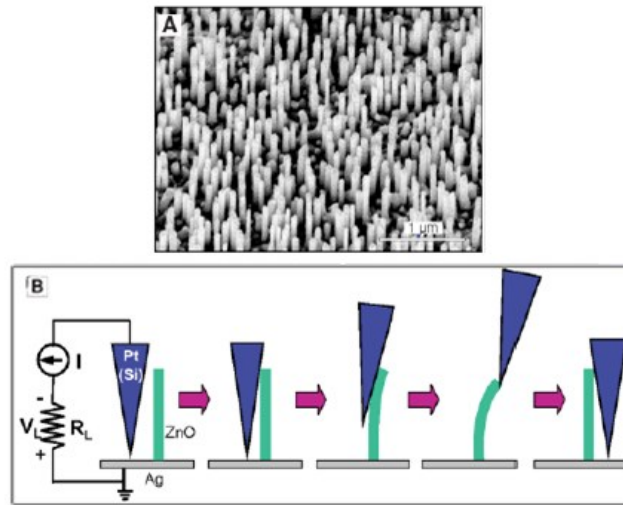
Figure 1.11: (a) SEM images of ZnO NWs, (b) Experimental setup for generating electricity by deforming a piezoelectric ZnO NW with a conductive AFM tip. The base of the NW is grounded and an external load R_L is applied, which is much larger than the resistance of the NW. Adapted from [52]

Zhu et al. [53] reported a flexible high output nanogenerator (HONG), based on a lateral ZnO nanowire (Figure 1.12). The generated electric energy was successfully used to power a commercial light-emitting diode (LED).
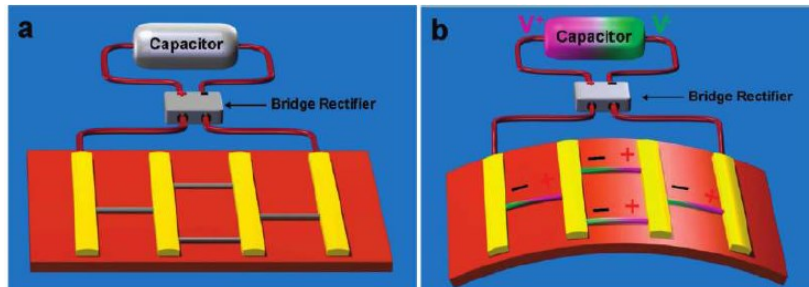
Figure 1.12: (a) Schematic of HONG's structure without mechanical deformation. Gold is used to form Schottky contacts with the ZnO NW arrays. (b) Output scaling-up when mechanical deformation is induced, where the "±" signs indicate the polarity of the local piezoelectric potential created in the NWs. Adapted from [53].

18

ZnO nanostructures are also suitable for photovoltaic application. The low reflectivity helps to optimize the light absorption, the high surface-to-volume ratio increases the charge separation probability and the effective electron transport along 1D structures enhances the charge collection. The potentialities ZnO nanostructures have been investigated in herojunction device as demonstrated by several papers published on n-ZnO/p-CuO$_2$ solar cells [54]. Moreover, considerable interest is focused on ZnO-based dye-sensitized solar cells (DSSCs) [55, 56], organic solar cells (OSCs) [57, 58], and hybrid organic-inorganic solar cells (HSCs) [59, 60]. These kinds of device represent promising approaches for inexpensive, large-scale solar energy conversion. In 2005, M. Law et al. first introduced a new version of the dye-sensitized cell in which the traditional nanoparticle film was replaced by a dense array of oriented ZnO nanowires [56], reaching a conversion efficiency η=1.2-1.5% (Figure 1.13).
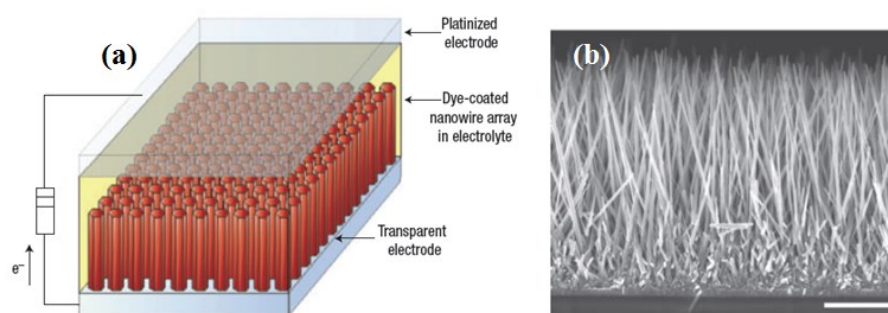
Figure 1.13: (a)Schematic diagram of ZnO NWs based dye sensitized cell. (b) SEM cross-section of ZnO NWs array on FTO. Scale bar, 5 μm. Adapted from [56].

In HSCs, ZnO nanostructures are widely used to replace the electron acceptor organic semiconductors used in pure organic solar cells. Inorganic semiconductors, ZnO in particular, have higher electron mobility and chemical stability compared to those of organic semiconductor. Moreover, the versatility of ZnO nanostructures has led to the application of ZnO in solar cells with different device architectures, as shown in Figure 1.14. The power conversion efficiencies are typically below 1%, much lower than

those related to fully OSCs. Mainly, this may be due to the limited polymer infiltration in ZnO nanostructure as well as low polymer/ZnO wettability. [59, 61].
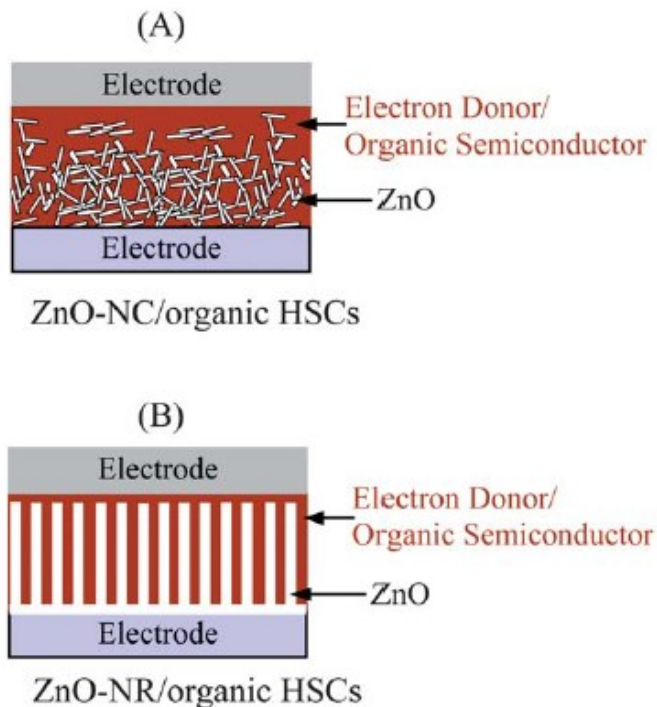
Figure 1.14: Schematic diagrams of ZnO nanostructures/organic semiconductor HSCs. (A) ZnO- nanocrystals (NC)/organic bulk heterojunction HSCs with randomly dispersed ZnO nanocrystals; (B) ZnO-NR/organic HSCs with vertically aligned ZnO nanorods. Adapted from [61].

Compared to ZnO/organic HSCs, the application of ZnO nanostructures as cathode buffer layer (CBL) or transparent electrode in OSCs are more promising [57, 62, 63]. ZnO films and nanostructures, by creating an Ohmic contact with the acceptor material, collect and extract electron carriers while block hole carriers. The improved carrier collection across the interface enhances the efficiency of the device.

20

1.2.2 UV Detection and Lighting

UV detection is another promising application of ZnO nanostructures. Photodetectors sensitive to UV radiation have a huge potential in spectroscopy, sensing device, astronomical studies and optical communications [64]. These technologies require the detection of UV light without the influence of visible or infrared light, in order to minimize the background signal and avoid erroneous detection. ZnO nanorods and nanowires, changing their electrical potential under UV irradiation, are particularly suitable for this purpose due to higher spatial resolution compared to thin film. The first individual ZnO-based nanowire photodetectors were reported by Kind *et al.* in 2002 [65]. The conductivity of the ZnO nanowires was extremely sensitive to UV light exposure (365 nm) and increases by a typically four to six orders of magnitude as shown in Figure 1.15.
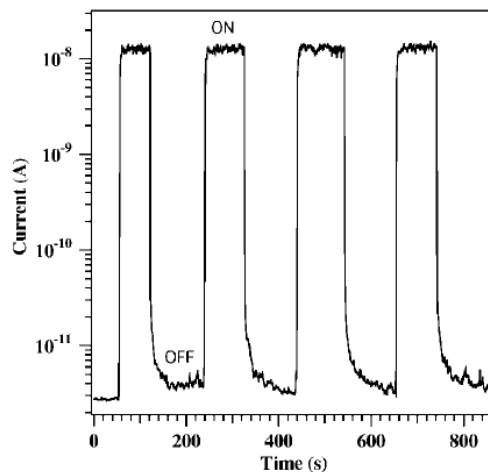
Figure 1.15: Reversible switching of a ZnO nanowire between low and high conductivity states when the UV-lamp (365 nm) was turned on and off. The bias on the nanowire is 1 V [65].

Many efforts were devoted to properly describe the mechanisms driving the UV sensing [8, 66]. It is generally supposed that atmospheric oxygen O_2 was

absorbed at the Vo sites on ZnO surface. Under UV illumination, electron-hole pairs are generated, holes migrate to the surface where O_2 desorption occurs. At the same time, the unpaired electrons contribute to enhance the conductivity. Recently, ZnO NRs grown by chemical bath deposition (CBD) within this PhD thesis work aimed to understand the role of the defect states with respect to O_2 desorption [67]. ZnO NRs exhibited two main PL peaks related to surface defects at 555 nm - originated from single ionized oxygen vacancy (V_o^+) - and 610 nm - due to V_o. In particular, the 555 nm PL intensity showed a transient in air ~20 s, which was correlated with the change in resistance under UV excitation, as shown in Figure 1.16. This correlation arises because O_2 desorption decreases the band bending and thus the concentration of V_o^+ states; simultaneously, charge separation reduces the sample resistance. On the other hand, the PL transient was suppressed in vacuum, because the depletion region is stable since O_2 desorption does not occur.
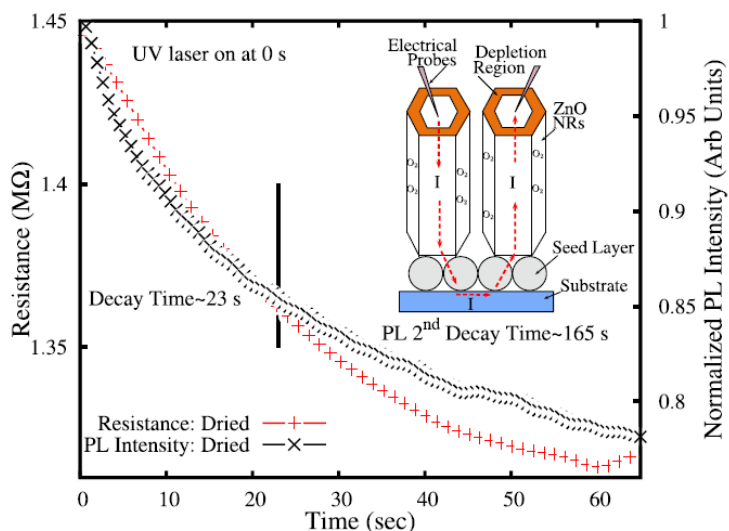
Figure 1.16: Comparison of the resistance and 555nm PL transient for ZnO NRs grown by CDB and dried in air at 100°C . Both transients have a decay time of 23 s. The inset represents the resistance measurement geometry. Adapted from [67].

ZnO nanostructures are attractive also for light emitting diodes (LED) and lasing in blue-UV spectral region. In 2001, room temperature UV

22

lasing in ZnO-nanowires was demonstrated [68]. Homojunction LEDs based on *p*-ZnO/*n*-ZnO structures are generally difficult to achieve due to the unavailability of high quality and stable *p*-type doping of ZnO. However, heterojunction LED using the combination of *n*-type ZnO with various *p*-type materials have been investigated [69].

1.2.3   Sensing

ZnO is widely employed also in chemical, gas and bio-sensing because it is particularly sensitive to the chemical environment. In particular, the nanostructures have the great advantages of high surface area over planar device configuration. The detection of gas is usually achieved using a conductometric gas sensor, since the adsorption of the gas on the sensor surface causes a change in its conductivity [70]. Hydrothermally grown ZnO NRs were widely studied for sensing different kinds of gas. Figure 1.17 reports the variation of the resistance of ZnO NRs exposed to H_2, NH_3 and CO [71].
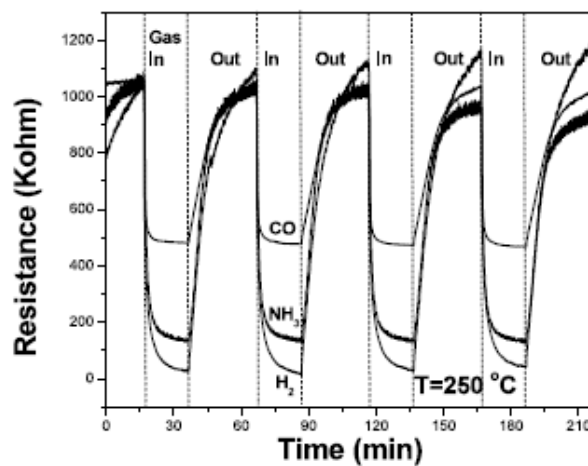
Figure 1.17: Resistance response curves of ZnO NRs gas sensor exposed to 200ppm H_2, NH_3 and CO, measured at 250 °C [71].

The basic working principle of a biosensor is shown in Figure 1.18. The sensing biomolecules need a support able to immobilize them and to enhance the electrochemical or optical signal transduction. Thanks to their biocompatibility, high isoelectric point (IEP= 9.5), chemical stability in the range of biological pH-values and strong binding properties, ZnO nanostructures is an excellent base matrix for biosensor devices [72]. Moreover, the increased sensing surface can allow single-molecule detection.
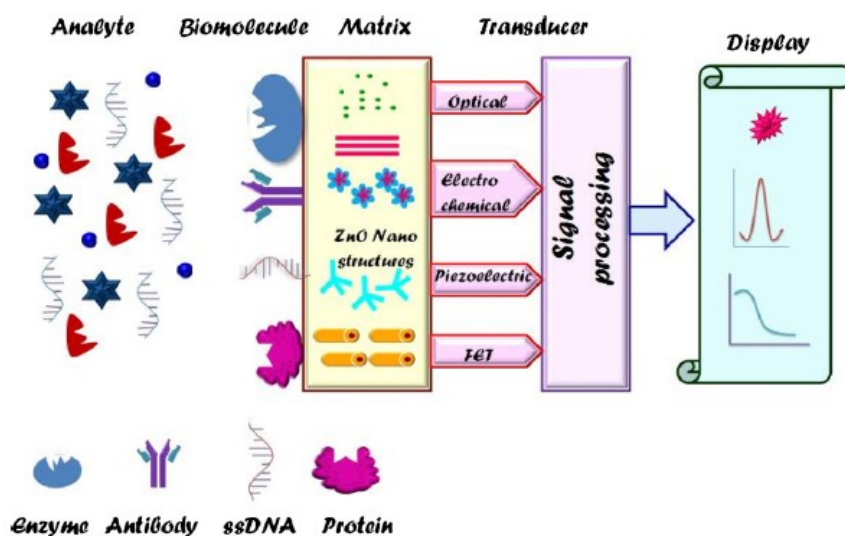
Figure 1.18: Schematic of biosensor assembly [72].

As example of ZnO nanostructures employed in biosensing, Figure 1.19 reports the SEM images of a selective intracellular glucose biosensor based on a tip coated with ZnO NWLs [73] whose monitoring capability was demonstrated by following the variation induced by insulin in the intracellular glucose concentration in human dipocytes and frog oocytes. For increased stability and selectivity, the sensing layer was functionalized by glucose oxides (GO) and protected by Nafion.
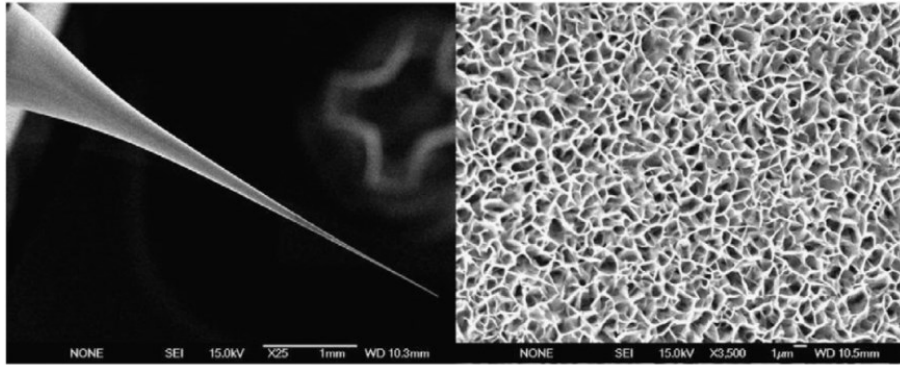
Figure 1.19: SEM images, with different magnification of the ZnO NWLs grown on an aluminum-coated glass capillary [73].

1.3   Synthesis of ZnO nanostructures

ZnO nanostructures can be synthesized by different techniques, including high temperature vapor phase deposition and low temperature solution routes, both methods based on "bottom up" approach.

1.3.1   Vapor Phase Synthesis Methods

Traditionally, the primary ways of growing ZnO nanostructures were the vapor-phase syntheses [69]. They can be categorized, based on the method used, as follows:

- *Physical Vapor Deposition* (PVD), including, among the others, thermal evaporation, sputtering, pulsed laser deposition (PLD), molecular beam epitaxy (MBE).

- *Chemical Vapor Deposition* (CVD), including organic chemical vapor deposition (MOCVD), metal organic vapor phase epitaxy (MOVPE), plasma-enhanced CVD (PECVD); most of them are based on vapor-liquid-solid (VLS) growth.

25

In general, the vapor phase synthesis method takes place in a vacuum chamber with a gaseous environment. Vapor species are first produced and then transferred and condensed onto the surface of a solid substrate. In PVD technology the material to be deposited is physically released from a source and transferred to a substrate with no chemical reactions during the process. CVD methods exploit the chemical reactions occurring between the vaporized material and the volatile precursor. Typically, the temperature involved in this kind of process ranges from 500°C to 1500°C.

The vapor-phase approaches mentioned so far have dominated the synthesis of ZnO based nanostructures. They allow to produce very high quality, single crystal ZnO nanostructures but several processing parameters such as temperature, pressure, gas species, flow rate, evaporation period must be accurately controlled. In addition, they require expensive equipment, and relatively high growth temperatures. Consequently, they do not meet the demand of cost effectiveness, often requested for disposable and massive production. Thus, many efforts have been made to developing simpler wet-chemical synthesis methods at lower temperature.

1.3.2　Solution Phase Syntheses Methods

Compared with high temperature vapor techniques, solution growth methods take the great advantages of low growth temperature (<300°C) allowing a greater choice of shape and type of substrates including flexible-stretchable substrate, fibers and temperature sensitive substrate like polydimethylsiloxane (PDMS) and Polymethyl methacrylate (PMMA) [30]. Figure 1.20 shows, as example, a flexible and fully rollable nanogenerator and a flexible plastic hybrid solar cell based on solution-derived ZnO nanorods. Other benefits are the simplicity of the experimental setup, the low costs of the process and the high potential in scalability. Obviously, there are also disadvantages. Chemical waste treatment needs to be addressed in view of future commercialization. In addition, the control of morphology of the nanostructures, using these techniques, is challenging due to the partial understanding of the whole process underlying the growth of nanostructures. Consequently, with respect to vacuum techniques, the solution based synthesis methods have the drawbacks of lack of good control over growth

26

kinetics and unsatisfactory reproducibility from one laboratory to another. Such problems can be even more severe when large scale production is attempted.
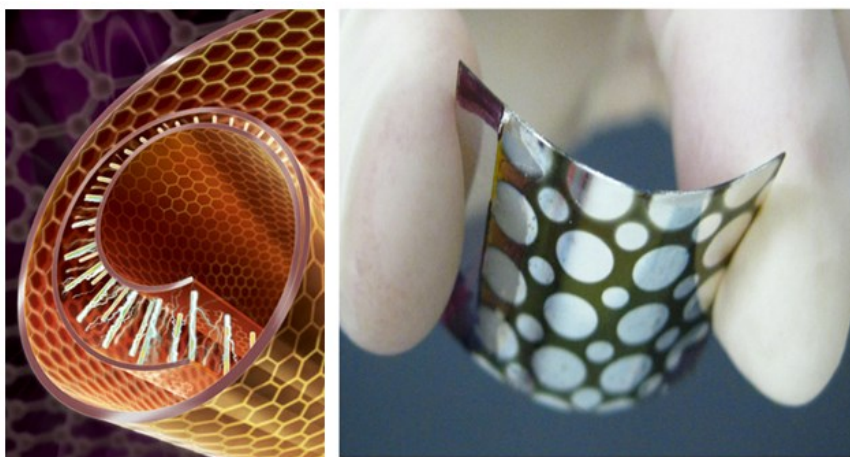
Figure 1.20: (a) Cover Picture of Advanced Material 18/2010 related to ref [74] representing a fully rollable transparent nanogenerators based on ZnO NRs growth by solution growth method on graphene transferred onto flexible polymer substrate. (b) Photograph of flexible plastic solar cell of conjugated polymer hybridized with ZnO nanorods. Circular patterns of silver are top electrodes. Adapted from [75].

The most common solution based synthesis approaches include the electrochemical deposition (ECD), the sol-gel synthesis and chemical bath deposition (CBD). Figure 1.21 illustrates the simplified schemes of these techniques.

ZnO nanostructure, like nanorods, nanotubes and nano-porous film [77, 78] can be deposited electrochemically from an aqueous solution of Zn salt in the presence of dissolved oxygen. The basic principle is the increase of the surface pH controlled by the electrochemical formation of hydroxyl ions (OH^-) in the reduction reaction of the oxygen precursor. This leads to a local supersaturation for ZnO precipitation which drives the formation of a zinc oxide film on the electrode surface. The three most commonly used oxygen precursors for this purpose include nitrate ions, dissolved molecular oxygen and hydrogen peroxide [30,79]. One advantage of this technique is

27

the improved nucleation density so that many substrates do not need a pretreatment to generate a seed layer. In addition, although doping of ZnO is a critical issue for aqueous methods, electrodeposition has been successfully employed for this purpose [80, 81].
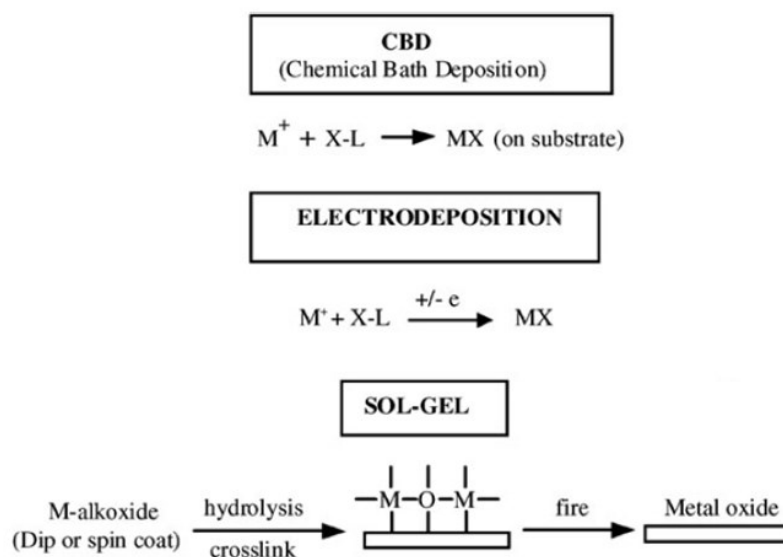
Figure 1.21: Schematic diagram of different techniques of solution deposition. M^+ refers to a cation (usually a metallic precursor); X-L a precursor compound where X is the non-metallic species (generally a group VI element) and L a ligand. Adapted from [76].

The sol-gel methods is the most used method in the synthesis of ZnO nanoparticles even if also thin film and nanorods with preferred crystallographic orientation have been synthesized with this method [82, 83]. The growth solution contains four different kinds of material: precursor, solvent, catalyst and stabilizer and the process generally involves different stages leading the monomers to agglomerate in nanoparticles. The properties of a particular sol-gel network are related to several parameters such as pH, temperature and time of reaction, reagent concentrations, catalyst nature and concentration, aging temperature and time, and drying process [84].

28

The chemical bath deposition is the simplest and most versatile among all the solution growth methods. It does not require the application of external potential, it is also suitable for insulating substrate and shows the highest deposition rate. Moreover, CBD well suits for large-area production. There is currently a vibrant research effort in developing controlled growth of ZnO nanostructures by CBD and the present thesis mainly focuses on the study and optimization of this technique. Chemical bath deposition has been employed to deposit films of metal sulfides, selenides and oxides since almost 150 years ago [Semiconductor by CBD2] but only recently, within the "nanotechnology revolution", it has emerged as powerful deposition technique. In general, CBD refers to the synthesis in solution involving, in the case of oxides deposition, the hydrolysis of metal cations. Figure 1.22 shows the number of publications as given by the information-service provider Thomson Reuters on 16th November 2015 by looking for "*ZnO and Chemical Bath Deposition*".
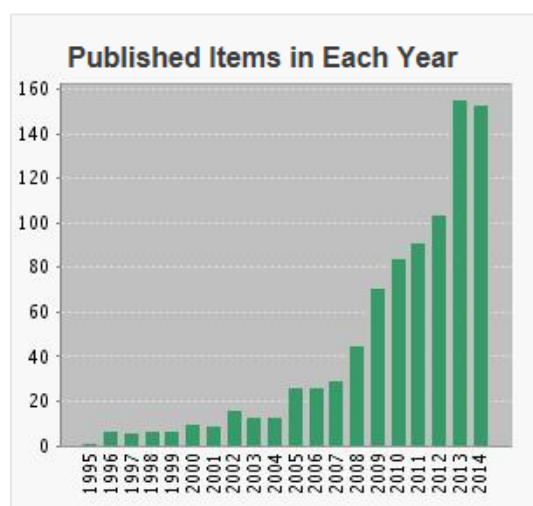
Figure 1.22: Published items per year related to ZnO and CBD.

The bibliometric data reflect the growing interest of the scientific community for this kind of synthesis for ZnO, confirmed also by the over 15000 citations from 1995 to 2014 (almost 3000 citations only in 2014).

However, the emerging trend has only a qualitative value, being underestimated by the variable nomenclature associated to CBD. Indeed, many different terms are used to denote CBD: chemical solution deposition, chemical deposition, electroless plating, liquid phase deposition and aqueous chemical growth. In the last years a general consensus has begun to favor the term CBD. In addition, the chemical bath deposition has many similarities with another type of synthesis named hydrothermal deposition, an aqueous solution method carried out using a closed bath inside a laboratory (or microwave) oven instead of open beaker on hotplate as in CBD (Figure 1.23). Hydrothermal synthesis involves process at low temperature aqueous solution and at high pressures. In general, the solubility of ZnO is greater under hydrothermal conditions and the growth is typically slower [85].
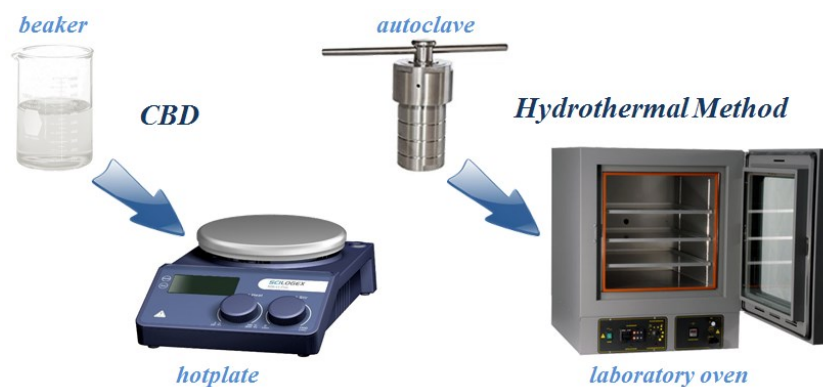
Figure 1.23: Schematic experimetal setup of CBD and hydrothermal method.

1.4   ZnO Nanorods: Key Features in CBD

ZnO NRs are of great of interest due to their quasi 1D structure. The most important requirements for ZnO NRs to become industrially viable are the synthesis reproducibility and the production costs. Low-cost CBD route allows to synthesize ZnO NRs with structural quality comparable with those produced by expensive gas-phase approaches [11, 69-70, 86]. In addition, recent scientific research has been able to solve critical issues that prevented

the deep understanding and good control of the chemico-physical mechanisms underlying the formation of ZnO NRs via CBD.

Many combinations of chemical precursors can be used for the synthesis of zinc oxide micro/nano rods via CBD [30, 85, 87, 88] but, undoubtedly, the most performing chemical procedure is that described by Vayssieres et al. in 2001 [89]. They achieved in the deposition of highly oriented ZnO NRs array on substrate by readapting an effective method for the formation of rod-like ZnO in homogeneous solution [90, 91].
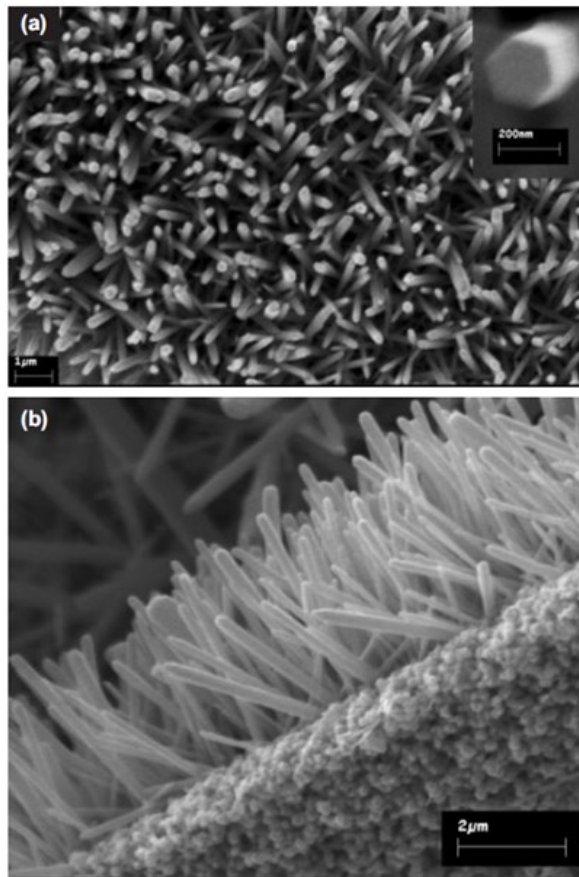
Figure 1.24: SEM images of ZnO NRs grown by aqueous chemical method on (a) silicon wafer, (b) ZnO nanostructured thin film. Adapted from [89].

31

Arrays of ZnO NRs were formed on rough substrates immersed in an aqueous solution of Zinc nitrate ($Zn(NO)_3$) and hexamethylenetetramine (HMTA, $(CH_2)_6N_4$) under continuous heating. In Figure 1.24 shown SEM micrographs of ZnO nanorods grown on silicon substrate and on ZnO nanostructured thin film.

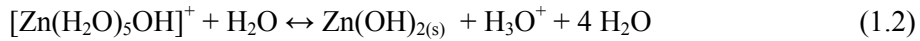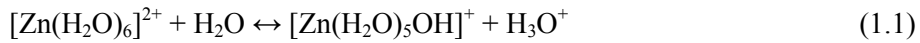Zn^{2+} ions, coming from the dissociation of zinc nitrate in water, gives rise to the formation of different hydroxyl species, depending on Zn^{2+} concentration, pH and temperature of the solution. Typically, the pH and Zn^{2+} concentration in chemical bath deposition are such that the formation of ZnO on the substrate occurs via $Zn(OH)_2$ formation[92]. Then solid ZnO nuclei are formed by the dehydration of these hydroxyl species [93].

In CBD of ZnO, ligands like HMTA are employed for keeping under control the concentration of free zinc ions. The formation of a solid phase in the solution should start when the ionic product (IP) exceeds the solubility product constant (Ksp). The constant Ksp for $Zn(OH)_2$ is in the order of 10^{-17}. In absence of ligands, the IP for $Zn(OH)_2$ easily exceeds the Ksp value while their addition tends to reduce the concentration of the Zn^{2+} ion by producing complex ions which avoids the spontaneous precipitation [94].

The following chemical reactions summarise the typical processes occuring in solution:

$$[Zn(H_2O)_6]^{2+} + H_2O \leftrightarrow [Zn(H_2O)_5OH]^+ + H_3O^+ \qquad (1.1)$$

$$[Zn(H_2O)_5OH]^+ + H_2O \leftrightarrow Zn(OH)_{2(s)} + H_3O^+ + 4\,H_2O \qquad (1.2)$$

$$Zn(OH)_{2(s)} \leftrightarrow ZnO_{(s)} + H_2O \qquad (1.3)$$

After Zn nitrate dissociation, Zn^{2+} ion forms a complex with 6 water molecules $[Zn(H_2O)_6]^{2+}$, while hydrolysis equilibria of $Zn^{2+}_{(aq)}$ move to the right for the simultaneous protonation of the HMTA itself or of the ammonia groups coming from HMTA decomposition:

$$(CH_2)_6N_4 + H_3O^+ \leftrightarrow [(CH_2)_6N_4]H^+ + H_2O \qquad (1.4)$$

or

32

$$(CH_2)_6N_4 + 6\ H_2O \leftrightarrow 6\ HCHO + 4\ NH_3 \qquad\qquad (1.5a)$$

$$NH_3 + H_3O^+ \leftrightarrow NH^{4+} + H_2O \qquad\qquad (1.5b)$$
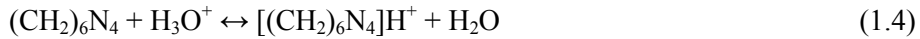
It is worth outline that stoichiometric deposits are easily obtained since the basic building blocks are ions instead of atoms [94].

Two different kinds of nucleation mechanisms occur in the solution. The homogeneous nucleation of solid ZnO takes place in bulk solution and requires a higher activation energy while the heterogeneous one, promoted at any solution-substrate interface, is energetically more favorable. Consequently, hetero-nucleation can occur at a lower saturation ratio onto a substrate than in bulk solution. Under such synthetic conditions, ZnO anisotropically grows on the substrate assuming the shape of crystal micro-nanorods along the easiest direction of crystallization, as expected when the system is closer to thermodynamic equilibrium [95]. Indeed, the thermodynamically stable phase for ZnO, as described above, is wurtzite structure. In particular, the polar faces are less stable and with higher energy than the non-polar phases, so the c-axis results the fastest growth direction. However, the growth rates of different surfaces can also be kinetically controlled by using additives that preferentially adsorb to specific crystal faces [96] or by modifying the molar ratio of the precursors.

A fundamental contribution was given by the work of Greene's group at of Lawrence Berkeley National Laboratory (University of California) [97]. They expanded the synthetic approach developed by Vayssieres et al. and proposed a simple two-step procedure enabling the deposition of dense arrays of ZnO nanorods on any kind of substrate [ref.]. In the first step, zinc oxide nanocrystals (prepared according to the method of Pacholski [98]) were spin-coated on the substrate, then the seeded substrate is suspending in the growth solution containing zinc nitrate and HMTA (25mM), kept at 90°C. Figure 1.25 reports a SEM image of ZnO NRs grown on silicon by following the Greene's procedure. The presence of the seed layer allows the use of a very wide range of substrate material and improves the adhesion of the nanorods on the substrate. Afterwards, different methods for creating ZnO seed layer were developed and numerous

studies were conducted with the aim to clarify the relationships between the morphology of the seed layer and the structural properties of resulting nanorods [99, 100]. Guillemin et al. [101] demonstrated that increasing the diameter of ZnO nanoparticles of the seed layer, leads to a decrease of the average diameter of the resulted NRs and to an improvement of their alignment.
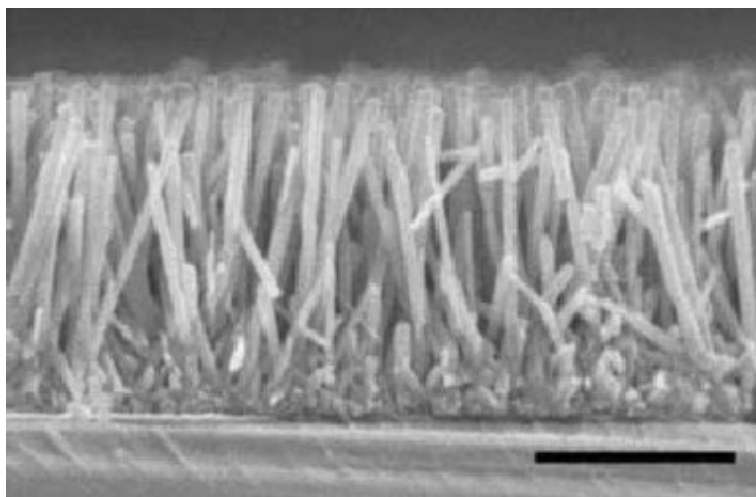
Figure 1.25: Cross-sectional SEM image of an array grown over 1.5 h on a silicon wafer (scale bar=1 μm). Adapted from ref [97]

Another work of the same group, reported on the crucial role of crystal orientation and polarity of the ZnO monocrystal seed layer [102]. ZnO nanorods showed to preferentially nucleate on polar c-plane due to the strong electrostatic interactions with Zn^{2+} and OH^- ions dispersed in solution. When the seed layer was highly textured along the c-axis, the nanorods array resulted well aligned and dense, on the contrary of the case of poorly textured seed layer, Figure 1.26.
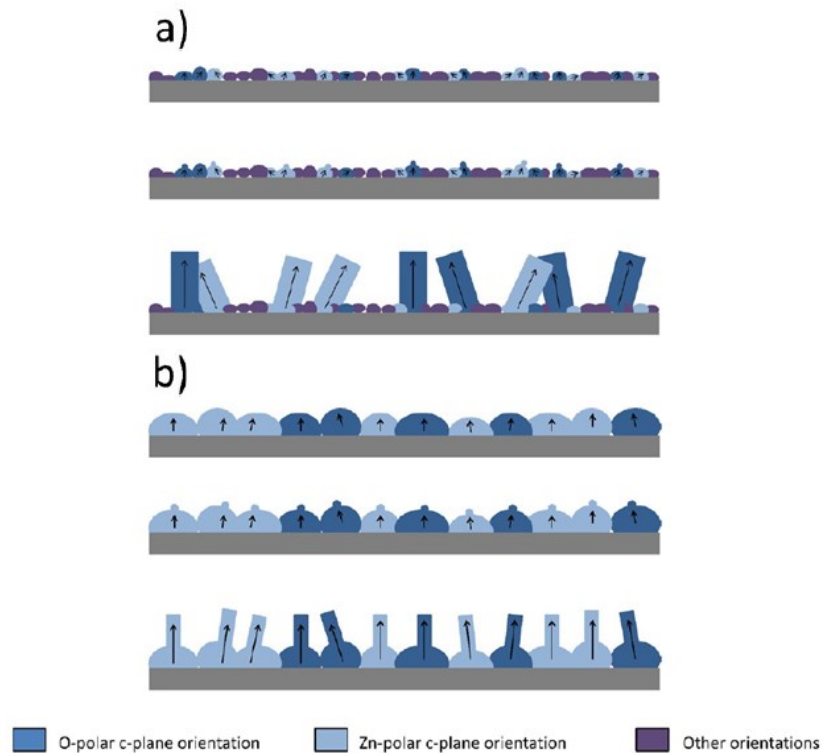
Figure 1.26: Diagram for the nucleation and growth processes of ZnO NRs on a (a) thin, poorly textured or (b) thick, well textured seed layer. Adapted from ref [102]

Understanding the CBD kinetics of ZnO nanostructures is a fundamental issue to achieve a good control of the morphology and thus to ensure the required level of reproducibility. In the past decades a considerable experience has been acquired and many groups have studied the effects on the growth mechanism arising from the variation of the experimental parameters such as reagents concentration, temperature, pH, growth time [85, 96, 103, 104]. The refined work of Boercker et al. [105] demonstrated that the heterogeneous growth of ZnO nanorods on seeded substrate is mass transport limited, resulting in an inverse relationship between NRs density and dimension. A one-dimensional model,

schematically illustrated in Figure 1.27, was developed, describing the transport of the chemical species near the substrate.
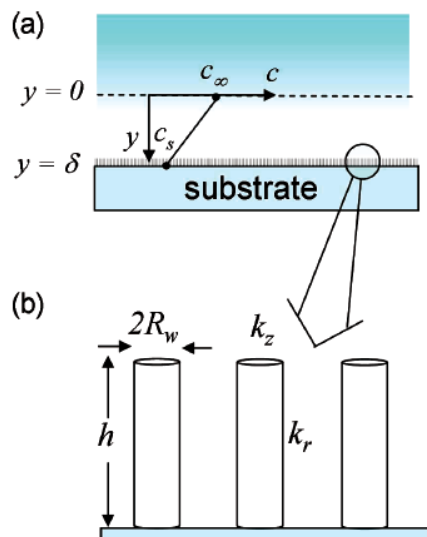
Figure 1.27: One-dimensional model used to calculate the temporal evolution of the nanowire height and diameter. δ is the thickness of the concentration boundary layer; c is the concentration of the NR precursor that varies along y. c_∞ is the bulk precursor concentration, and c_s is the concentration at the NRs surface. (b) A portion of (a). R_w and h are NRs radius and height, respectively. k_z and k_r are the first order surface reaction rate constants on the top (0001) and sides of the nanowires $(10\bar{1}0)$, respectively [105].

The main assumptions were the absence of homogeneous reaction near the substrate and the consumption of the zinc precursor via first order heterogeneous reactions. The NRs radius, R_w, and height, h, are functions of time and increase at different rates. The (0001) and $(10\bar{1}0)$ surface reaction rates were taken to be first order in the precursor concentration and parameterized by reaction coefficients k_z and k_r. Under these assumptions the precursor concentration in the boundary layer of thickness δ is linear and decreases from the bulk concentration, c_∞, to the concentration in the solution just above the nanorods, c_s.. This model predicts that when the growth is mass transport limited, the nanorods height and diameter scale as

$\sim 1/N$, being N the NRs density. Experiments carried out by varying the NRs density confirmed such theoretical expectation, as shown in Figure 1.28.
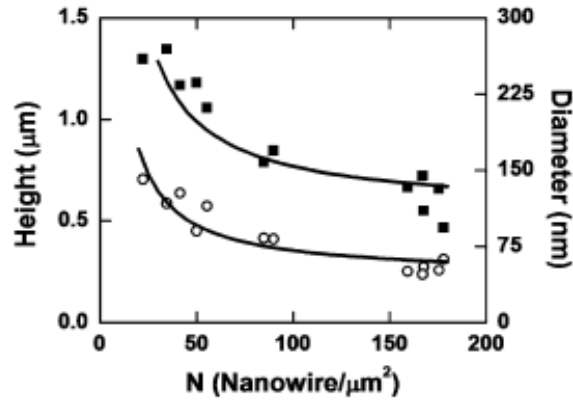
Figure 1.28: Experimentally determined NRs height (■) and diameter (O) as a function of nanowire density. Both trends are consistent with 1/N [105].
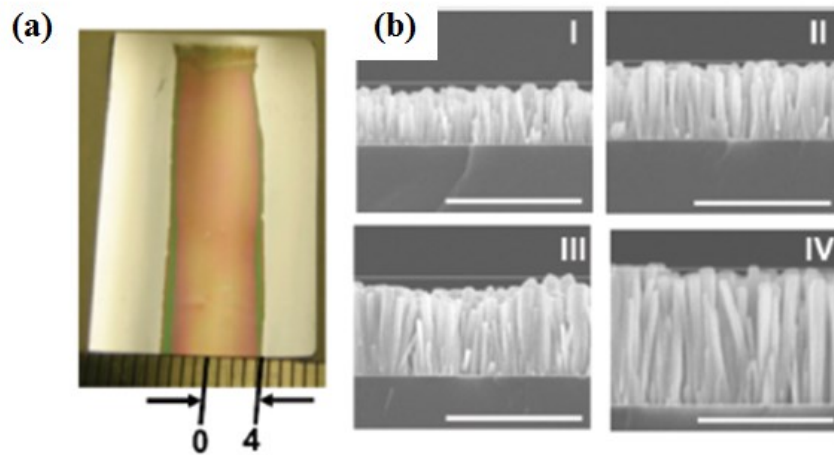
Figure 1.29: (a) Image of a sample ZnO NRs on a Si substrate patterned with an ~8 mm wide strip of ZnO seeds in the middle of the substrate. The darker part of the substrate is where the nanowires have grown and the lighter parts are unseeded regions where there are no NRs. (c) Cross-sectional SEM images of the NRs array at different locations between the positions 0-4 indicated in (a). Adapted from [105].

As further confirmation, the mass transport limitation was proved to be responsible to the non-uniform growth in the area between seeded and unseeded regions. A Si substrate was patterned and seeded only in the middle of the substrate, leaving the rest of the surface unseeded. Consequently, ZnO NRs grew only in the middle of the substrate (Figure 1.29(a)). Figure 1.29(b) shows cross sectional SEM images at various points between the position 0-4 labeled in Figure 1.29(a). Moving towards the unseeded region, NRs height increases because of the higher ZnO precursor concentration near the boundary between the seeded and unseeded regions. Finally, Boerker et al. confirmed that the anisotropic growth of ZnO NRs is not driven by the mass transport growth but by the growth kinetics of (0001) and (10$\bar{1}$0) planes of ZnO in the considered synthetic conditions, as already verified also by other authors [106].

1.5 ZnO Nanowalls: a brand new material

The effect of the substrate on the nature of the ZnO nanostructure formed via CBD was extensively studied [85]. It was observed that the usual shape assumed by ZnO, in chemical bath containing zinc nitrate and HMTA, is the nanorod one. However, as the substrate is Al or Al covered wafer, a particular 2D morphology of ZnO is formed, named usually nanowalls (NWLs) consisting of ZnO crystalline foils. ZnO NWLs (or nanoplatelets) grow vertically on Al substrates, with an intertwined, random, honeycomb-like pattern and *c*-axes parallel to the substrate. The first study of ZnO nanowalls was reported by Ng *et al.* [107] through carbothermal reduction (thus not a CBD method) for growing vertical ZnO nanowalls on a sapphire substrate, Figure 1.20.
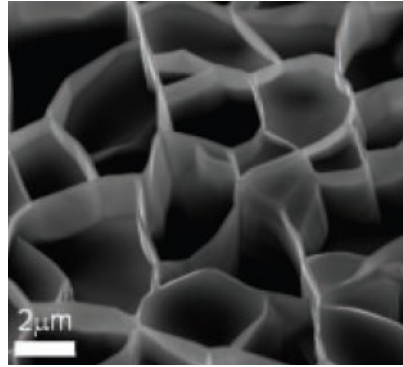
Figure 1.20: ZnO nanowalls grown by carbothermal reduction on sapphire with a height of 5µm. Adapted from [107]

As in the case of ZnO NRs, NWLs can be prepared by both physical and chemical vapour deposition techniques, with operating temperatures higher than 800 °C [108, 109]. Alternatively, ZnO NWs can be easily synthesized on Al-covered substrate by CDB at 90 – 100 °C [110-112]. However, in contrast to the case of 1D ZnO NRs, ZnO nanowall structure has not been investigated as much, although its huge surface-to-volume ratio and extremely thin wall thicknesses pave the route for many interesting applications [108,110- 112]. Ye et al. [110] reported the synthesis of ZnO NWLs on Al wafer in an equimolar solution of zinc nitrate hexahydrate and HMTA. For comparison, they produced ZnO NRs on Si substrate, using the same growth solution, as presented in Figure 1.21.

It is reasonable to assume that the presence of Al in the substrate is important for obtaining ZnO NWs, since the growth suppression effect along [001] direction can be originated from Al. Indeed, aluminum is an amphoteric metal and it can dissolve in the alkaline conditions. Therefore, in aqueous solution containing HMTA, Al undergoes chemical reaction, forming Al $(OH)_4{}^-$, as follows:

$$2Al_{(s)} + 6H_2O + 2OH^- \rightarrow 2\ Al(OH)_4^- + 3H_2 \qquad (1.6)$$
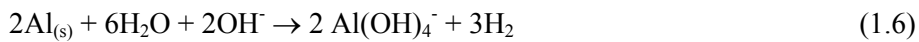
These Al complexes bind to the Zn^{2+} terminated (0001) surface and suppressed the growth along [0001] direction [110-112].
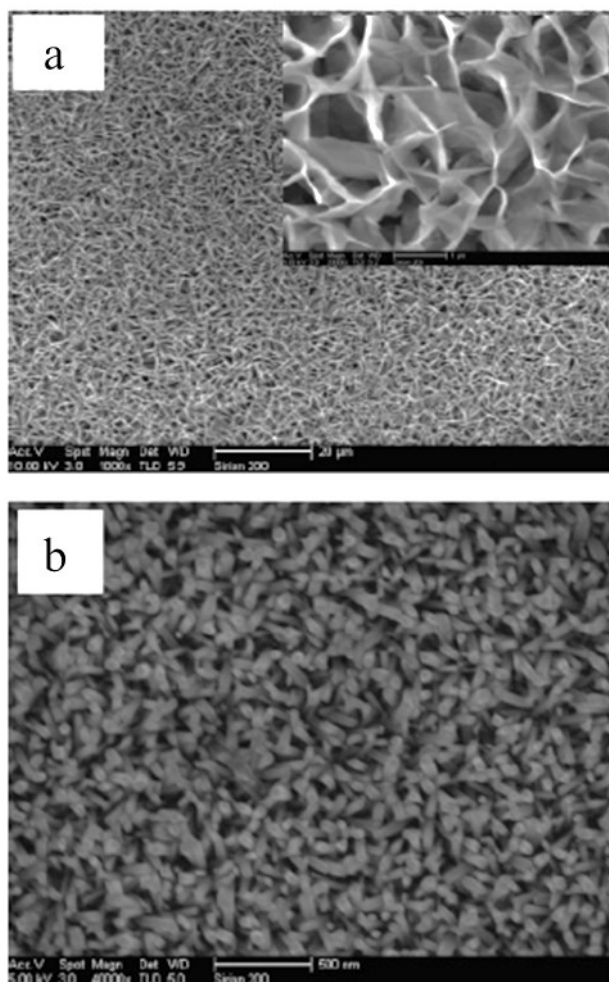
Figure 1.21: SEM images of nanostructures grown by CBD. (a) ZnO nanowalls at low magnification and higher magnification (inset); (b) ZnO nanorods arrays. Adapted from ref [110].

Ye et al. [110] demonstrated that by increasing pH from 6 to 12 (by adding ammonium hydroxide, AH), thinner nanowalls could be obtained. Changing the pH value of the solution alters the concentration of $Al(OH)_4^-$ in the solution as well as its adsorption quantity and coverage rate [110]. Moreover, NWLs of Zn-Al carbonate hydroxide hydrate, a layered compound, and ZnO nanorods were obtained at pH 10 with zinc acetate,

ammonium hydroxide, and e-beam evaporated Al film [113]. The concentration of $Al(OH)_4^-$ influenced the particular product obtained; at high concentration of the Al complex, made possible by using a 1 μm Al film, only the Zn-Al carbonate hydroxide hydrate NWLs were obtained, while a 100 nm Al film gave the layer compound first, and later ZnO nanorods on top. The authors attributed the formation of ZnO nanorod to the exhaustion of $Al(OH)_4^-$ needed to ensure the NW morphology. Therefore, it is clear that the growth rate of ZnO NWLs can be controlled by manipulating the rate of $Al(OH)_4^-$ generation that can be enhanced by increasing the pH of the solution. Moreover, starting from a solution of HMTA and zinc nitrate, a fast (10 min) sonochemical route for ZnO NW growth on Al and alumina substrates (with) at ambient conditions was reported by Nayak et al.[114]. However, there is no information on whether the growth dynamics and film quality differ between the two substrates. Moreover, prolonged sonication caused the NWs to peel off. ZnO NWLs can be also obtained by the selective etching of dense ZnO NRs films grown by CBD [115]. The process consists in three steps: the formation of a ZnO seed layer, the growth of ZnO NRs in an equimolar solution of 0.1M zinc nitrate and HMTA at 75°C and, finally, the etching into 0.3M KOH aqueous solution. The defect-selective dissolution in (0001) planes and along the c-axis, caused by the preferential adsorption of OH^- on particular faces, drives the formation of nanowall structure. Figure 1.22 shows etched ZnO NWLs and the initial NRs film.

At present, a complete picture of formation process of ZnO NWLs on Al substrate as well as an effective way to control the growth, have not yet been achieved.
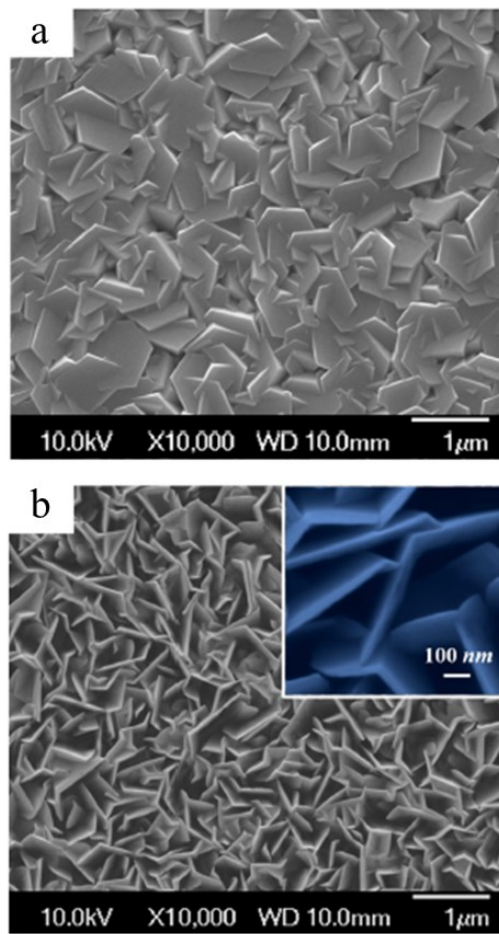
Figure 1.22: SEM images of (a) dense ZnO NRs film grown by CBD; (b) etched ZnO NWLs at different magnification. Adapted from ref [115].

Chapter 2

ZnO Nanorods Growth by Chemical Bath Deposition

ZnO nanorods grown by CBD are among the most promising semiconducting nanostructures currently investigated for a variety of applications. As a consequence, many works have been devoted to deeply understand the microscopic mechanisms leading to high aspect ratio and vertically aligned ZnO NRs. Still, contrasting experimental results appear in the literature.

This chapter presents a systematic investigation of the chemical deposition of ZnO nanorods using zinc nitrate salt and hexamethylenetetramine (HMTA). An optimized procedure for reproducible synthesis is presented as well as the growth kinetics is discussed. In addition, an empirical study evidences the double role of HMTA in the NRs growth mechanism. HMTA is shown to participate both as a supplier of OH^- ions and as a capping agent promoting the anisotropic growth. These two actions are not mutually exclusive and the amount of HMTA in solution determines the key process variable. This represents a promising step towards a better control of CBD synthesis.

2.1   HMTA, the key player

In recent years the possibility to fully exploit the advantages of CBD of dense arrays of zinc oxide NRs has stimulated detailed studies. Significant progress has been made in investigating the growth mechanisms, nevertheless the interpretation of the obtained results has been often matter of discussion. In particular, the role of HMTA in the growth kinetics is currently under debate and in this regard the literature proposes some contrasting interpretations. HMTA is a tertiary amine highly soluble in water, having a symmetric tetrahedral cage-like structure with four nitrogen atoms (N) at the four corners and six methylene bridges (-CH_2-) as shown in Figure 2.1. It is the most used ligand in the chemical bath deposition of zinc oxide nanostructures.
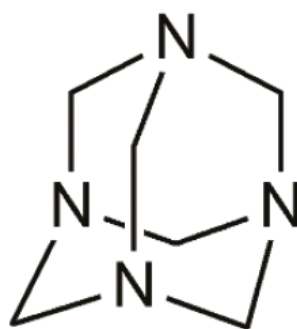
Figure 2.1: Chemical structure of HMTA. Adapted from ref. [116].

Many works have reported on the slow hydrolysis of HMTA in formaldehyde [CH_2O] and ammonia [NH_3] in the range of temperature and pH values involved in CBD [87, 92, 102, 117, 118]. Therefore, HMTA gradually releases the hydroxide ions driving the formation of ZnO (see Equations 1.1-1.5 in Chapter 1); at the same time, it controls the pH solution [85]. Ashfold et al. [92] have reported that the rate of HMTA decomposition at 90°C calculated for a zinc-free solution is the same of that observed experimentally in a solution containing zinc nitrate, implying that HMTA decomposition does not depend on the reactions taking place during ZnO formation and that HMTA is an effective pH buffer. Furthermore, HMTA or

44

other ammonia ligands can bind to the free zinc ions in solution, forming metal complexes and keeping the Zn(II) concentration under control [85, 93]. It is worth noting that the presence of HMTA in not essential for the ZnO nanorods growth [85, 116, 119] but it ensures crystalline and morphological properties better than other alkaline agent [Govender2004]. Near thermodynamic equilibrium, the driving force for the growth of wurtzite structured ZnO NRs is the minimization of the free energy of the system, as described in the Section 1.4. The elongated ZnO crystals are characterized by higher energy polar *c*-planes (with the alternation of Zn^{2+} terminated and O^{2-} terminated surfaces) and by non-polar lateral facets having lower surface energy. The fact that the anisotropic growth of these nanostructures is intrinsic to wet chemical methods and to wurtzite structure has found several experimental evidences [55, 105]. However, these thermodynamic considerations are not sufficient to explain the wide variety of nanostructures and the role of the bath composition on the growth rate of polar and nonpolar crystal plane must be taken in account [55, 120].

Even if HMTA decomposition is assumed in most papers [117, 121], Sugunan et al. [122] first have proposed that HMTA does not degrade during CBD of ZnO NR. They used attenuated total reflection Fourier transform infrared (ATR-FTIR) spectroscopy performed on a mixture of 0.1 M HMTA and zinc nitrate upon continued heating, and revealed no change in the tertiary amine structure. As shown in Figure 2.2, the absorption peak at 1012 cm^{-1}, (stretching vibrations of C-N bonds of HMTA) was monitored at different times. If thermal decomposition of HMTA into formaldehyde and ammonia had occurred, a significant reduction of the absorption signal would have been detected. Only a negligible degradation of the tertiary amine has been revealed by infra-red spectroscopy, although the anisotropic growth of ZnO was observed within 5 hours.
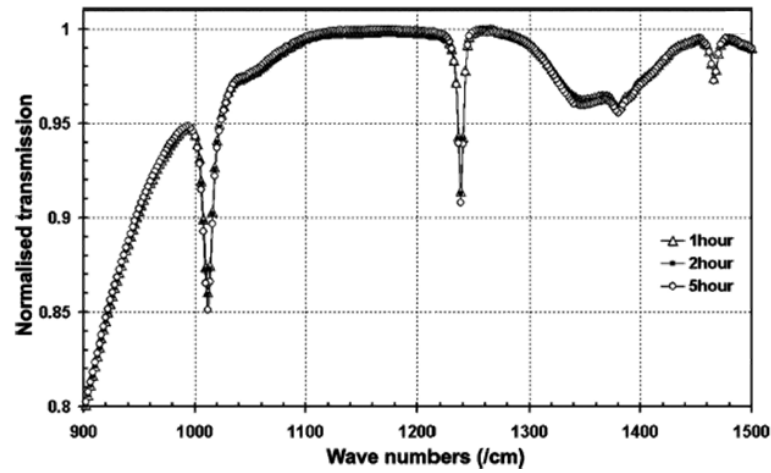
Figure 2.2: ATR-FTIR spectra for a solution of HMTA and zinc nitrate kept at 65°C for 1, 2 and 5 hours. Adapted from ref. [122].

They have also suggested that HMTA molecules, being non-polar chelators, are able to attach the non-polar surfaces of the nanorods acting as a capping agent for these facets and propelling the anisotropic growth along the c-axis, Figure 2.3.
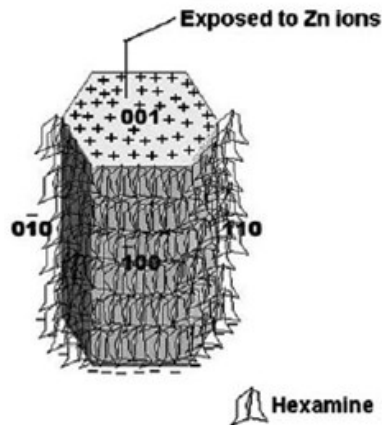
Figure 2.3: Illustration of the possible role of HMTA in the anisotropic growth of zinc oxide nanowires. Adapted from ref. [122].

46

Such *shape-inducing* effect of HMTA has been recently refuted in 2014 by McPeak et al. [116], who have claimed that ZnO nanorods growth by CBD does not involve the adsorption of HMTA on the ZnO lateral faces and the role of HMTA is only to control the saturation index of ZnO through the slow release of hydroxide ions.
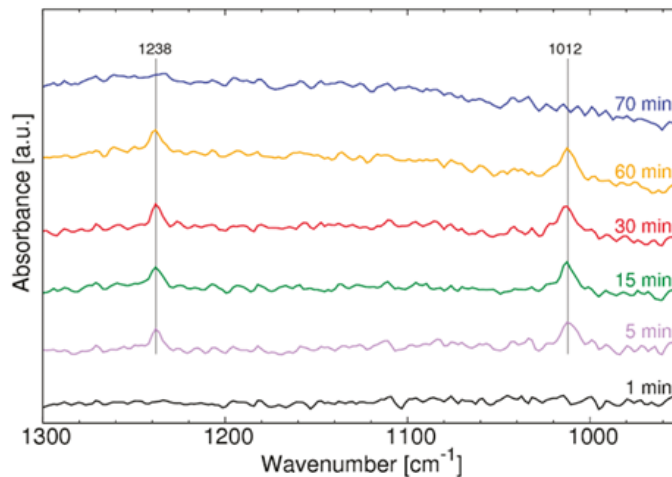
Figure 2.4: Time resolved ATR-FTIR spectra during the adsorption study of 1mM HMTA in 25mM KCl on ZnO nanoparticles. Adapted from ref. [116].

Figure 2.4 reports the results of *in situ* ATR-FTIR analysis performed by flowing 1mM HMTA in 25mM KCl solution on ZnO nanoparticles film for 60 minutes, followed by 10 minutes of rinsing with an aqueous solution of KCl. After 5 minutes the peaks at 1012 and 1238 cm^{-1} appeared, corresponding to C-N stretch and CH$_2$ rock respectively. Moreover, the peak positions and intensities did not change within 60 minutes while all the signals disappeared after 10 minutes of rinsing. McPeak et al. interpreted these data as coming from the solution phase rather than as indicating HTMA adsorption on ZnO.

Both works of Sugunan and McPeak are based on the results of attenuated total reflection Fourier transform infrared spectroscopy that, actually, allows to investigate the solid-liquid interface with high sensitivity.

47

On the other hand, to perform ATR-FTIR analysis of the zinc salt-HMTA chemical system, many expedients are needed in order to mimic the same mechanisms occurring under CBD conditions. In Sugunan et al.'s work, the ATR-FTIR spectroscopy was performed on a solution kept at 65°C with HMTA and zinc nitrate concentration higher than typical concentrations of the reactants used for the NRs growth, thus adapting it to the sensitivity of the ATR measurements. McPeak et al. carried out the absorption study on ZnO nanopowder, instead of NRs, in order to maximize the ZnO surface area available for absorption. In addition, the ATR-FRT analyses were made at RT since higher temperature resulted in extensive dissolution of the ZnO nanoparticle film. To avoid ZnO dissolution and maintain the same fraction of unprotonated to protonated HMTA molecules, all aqueous solutions were titrated to a pH of 7.5 using KOH or HCl. Such approaches are generally well-accepted in literature, however, further investigations are needed. Moreover, the Sugunan's thesis on the shaping effect of HMTA was not supported by strong experimental evidences. For these reasons part of this thesis aims to clarify the mode of action of HMTA, representing a fundamental issue to achieve a good control of the morphology of one-dimensional ZnO nanostructures grown via CBD.

2.2   ZnO NRs Synthesis and Structural Characterizations

The first purpose of our work was developing the experimental procedure able to ensure high reproducibility and uniformity of the growth on the 2×2 cm^2 substrate area. We have referred to the two-step method proposed by Greene et al. in 2003 [97, 123] which involves a pre-coating step of ZnO crystallites and a subsequent CBD process. The seed layer promotes the heterogeneous nucleation on the substrate (while the homogeneous one typically occurs in the bulk solution at slower nucleation rate) and allows to produce perpendicularly oriented ZnO nanorods on any substrate. Figure 2.5 reports a cross section view of ZnO NRs arrays grown on very rough Si substrate, showing that however the surface is oriented, ZnO NR grows along the direction normal to the surface.
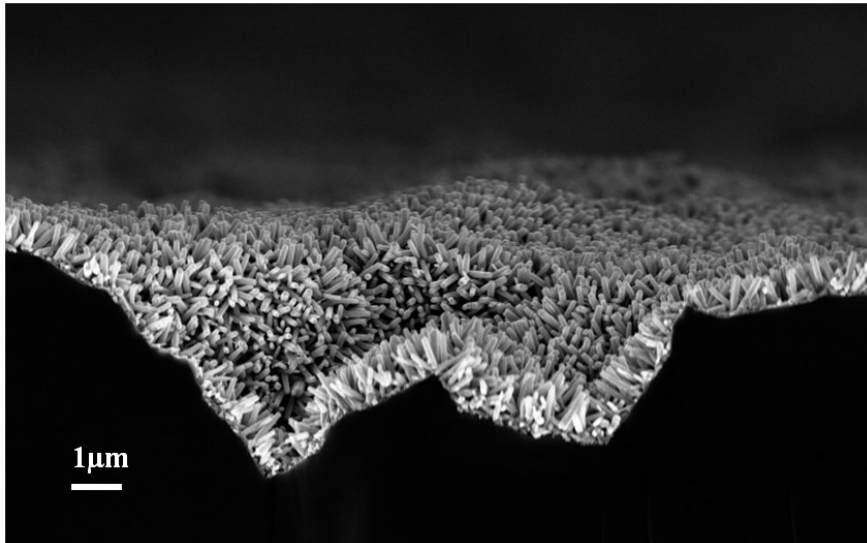
Figure 2.5: Cross section view of ZnO NRs grown by CBD on very rough Si substrate.

2.2.1   Seed Layer Preparation

ZnO nanorods arrays were grown by chemical bath deposition on n-type crystalline silicon (c-Si), glass, indium tin oxide (ITO) and gold coated (Au) substrate. However, if not specified, we will refer to nanorods grown on c-Si. The surface was cleaned by isopropanol and acetone rinsing. In our optimized procedure (see Appendix for details), a seed layer of ZnO crystallites was obtained by spin-coating (1000 rpm, 60 s) the surface with a solution of 5 mM zinc acetate dihydrate [(CH$_3$COO)2Zn·2H$_2$O] in ethanol (puriss. p.a., ACS reagent, $\geq$99.8%). Then the substrate was rinsed with a droplet of clean ethanol and annealed in air on a hot plate (at nominal temperature of 240 °C) for 20 minutes. A schematic of the seeding step is depicted in Figure 2.6.
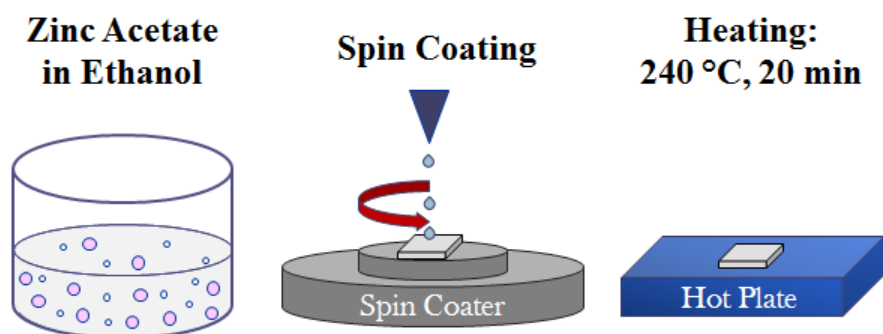
Figure 2.6: Illustration of the procedure for the preparation of the ZnO seed layer.

The morphological properties of the nanostructures were investigated by Scanning Electron Microscopy (SEM) using a field emission Zeiss Supra 25 system. The measurements were carried out with an acceleration voltage of 3-5 kV (the lower voltage was selected for analyzing nanorods arrays grown on glass in order to minimize charging effects) with an aperture size of 30 μm and a working distance of 2-5 mm. *In lens* detector was used for enhancing the signal coming from the secondary electrons (SE) generated in the upper range of the interaction volume and from the low-loss backscattered electrons originating from the beam spot centre. Therefore, high contrast images (containing direct information on the sample surface) are easily achieved. The statistical analysis based on the digital analysis of SEM images were conducted with the *Gatan Digital Microscope* software.

Figure 2.7(a) reports the SEM plane view of a seeded substrate consisting in small islands of ZnO (white spots) with an average size of 23 nm (size distribution from 5 to 50 nm) and a density of about 2.7×10^{10} seed/cm^2. This points out that the average distance (center to center) is about 60 nm, as it can be also appreciated by the SEM image. The evaluation of the average thickness of the seeds was done by Rutherford Backscattering Spectrometry (RBS). As shown in Figure 2.7(b), the RBS spectrum (2 MeV He$^+$ beam and 165° backscattering angle) contains a well-defined peak at 1.57 MeV corresponding to the atoms backscattered by surface ZnO atoms. The area under this peak is a quantitative estimation of the Zn dose [$(1.8\pm0.1)\times10^{15}$

Zn at./cm^2]. Assuming a cylindrical shape (diameter 23 nm) for the seeds and considering the ZnO density of 4.2×10^{22} ZnO molecules/cm^3, an average height of seeds of 4 nm can be estimated.
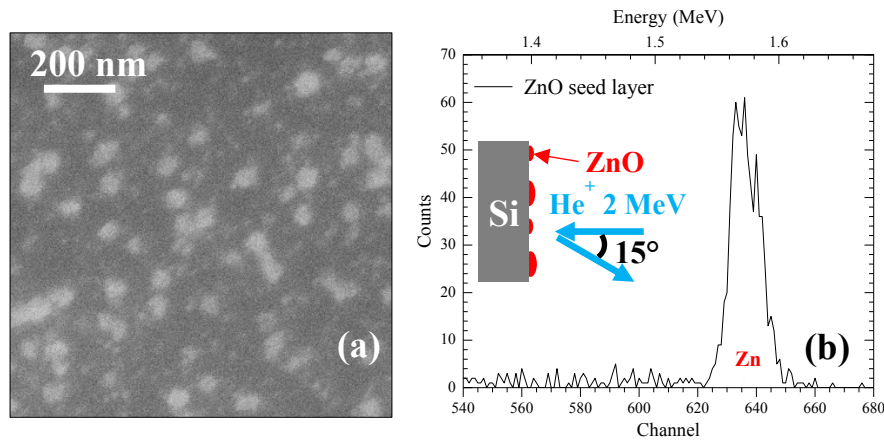
Figure 2.7: (a) SEM plan view of a seeded substrate (white spots are the seeds on the bare Si substrate). (b) Rutherford Backscattering Spectrum of He ions backscattered from Zn atoms, taken from the same sample of (a) with a 2.0 MeV He+ beam at a backscattering angle of 165 °, as depicted in the inset graph.

2.2.2   CBD

After the substrate was uniformly coated with ZnO seeds, the deposition of ZnO nanorods is carried out by vertically suspending the substrate in the growth solution for 1 hour, Figure 2.6. The sample position in the solution affects the sample quality. After many tests of the orientation, such as horizontal face up/ down, the vertical positioning of the sample, away from the bottom of the beaker, was revealed to be the best choice to minimize the deposition of crystallites on the substrate, coming from homogeneous nucleation in solution.An open large beaker filled with a 100 mL solution (50 mM) of zinc nitrate hexahydrate [Zn(NO$_3$)$_2$·6H$_2$O] in deionized (DI) water (Milli-Q, 18 MΩ·cm) and a small beaker filled with 100 mL solution of varying HMTA concentration in DI water were stirred

for 15 minutes and preheated at 90 °C. The HMTA solution was then poured in the large beaker. While zinc nitrate concentration in the CBD bath was set at 25 mM (after solution mixing), HMTA final concentration was varied in the 12.5−50 mM range. In some tests, HMTA was substituted or combined with propylamine [PA, $(CH_3)_3N$], a liquid primary amine highly soluble in water.
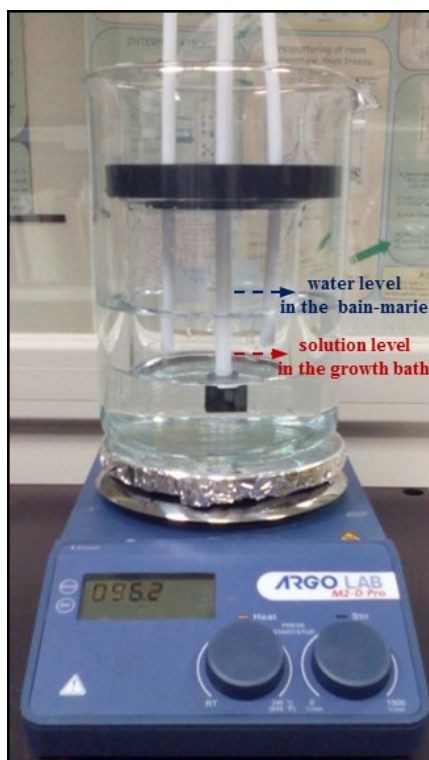
Figure 2.8: Experimental setup for the growth step. The apparatus which supports the samples was realized ad hoc, with Teflon bars placed so as to allow the simultaneous immersion of three samples.

As the concentrations of reactants vary with time (and at different specific rates), an aging effect of the solution can occur, decreasing the Zn^{2+}/OH^- ratio in a long CBD process [92, 117, 121]. In addition, the temperature of the solution heavily affects the growth kinetics [85, 103, 104]. These effects

have to be considered when performing CBD experiments; thus, particular care was taken to immerse the substrates immediately after the solution mixing and to keep the solution temperature fixed at 90 °C through a boiling water bath (bain-marie configuration, Figure 2.8). Only for the kinetics study presented in the section 2.4, reaction time and bath temperature were varied in the range 0.5−3 h and 65-90°C, respectively. pH and temperature were measured before, during and after the CDB with a pH-meter (EUTECH Instruments, pH2007) equipped with a temperature probe. Once the substrates were removed from the CBD beaker, they were rinsed with DI water and dried with N_2 gas.
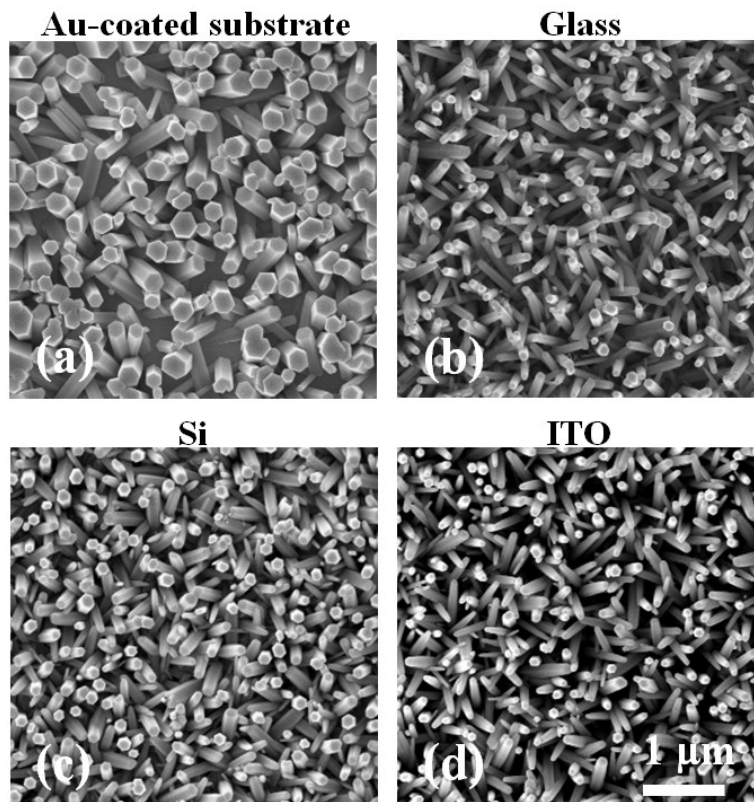
Figure 2.9: SEM images of ZnO nanorods arrays deposited on (a) Au-coated, (b) glass, (c) Si and (d) ITO substrates from 25mM solution of zinc nitrate and HMTA at 90°C for 1h. The scale bar is the same for all the images.

To test the versatility of the procedure, deposition experiments were performed using identical bath deposition (25mM $Zn(NO_3)_2 \cdot 6H_2O$ and HMTA, pH 5.7, 90°C, 1h) but different substrates. Micrographs of ZnO nanorods arrays on gold-coated, glass, silicon and ITO substrates are shown in Figure 2.9. The alignment of the ZnO nanorods is substrate-independent due to the presence of ZnO crystalline seeds, unlike the case of the seedless synthesis [85, 101, 102].

2.2.3   Structural Properties

Once defined the synthesis procedure, preliminary characterizations were performed in order to ascertain the crystalline and structural characteristics of the obtained ZnO nanorods.

RBS analysis was employed to verify the composition and the proper stoichiometry of a ZnO nanorods film (200 nm thick) grown for 30 minutes at 90°C, Figure 2.10. The signals at 1.6 and 0.7 MeV are related to the He^+ ions backscattered from zinc and oxygen atoms while the signal at 1.0 MeV refers to Si substrate. The area of each peak (after a proper background subtraction) is proportional to the dose of that element in the sample. The calculated atomic amount is the same for zinc and oxygen (about 7.5×10^{17} at/cm^2) corresponding to a stoichiometric relationship Zn:O=1:1.
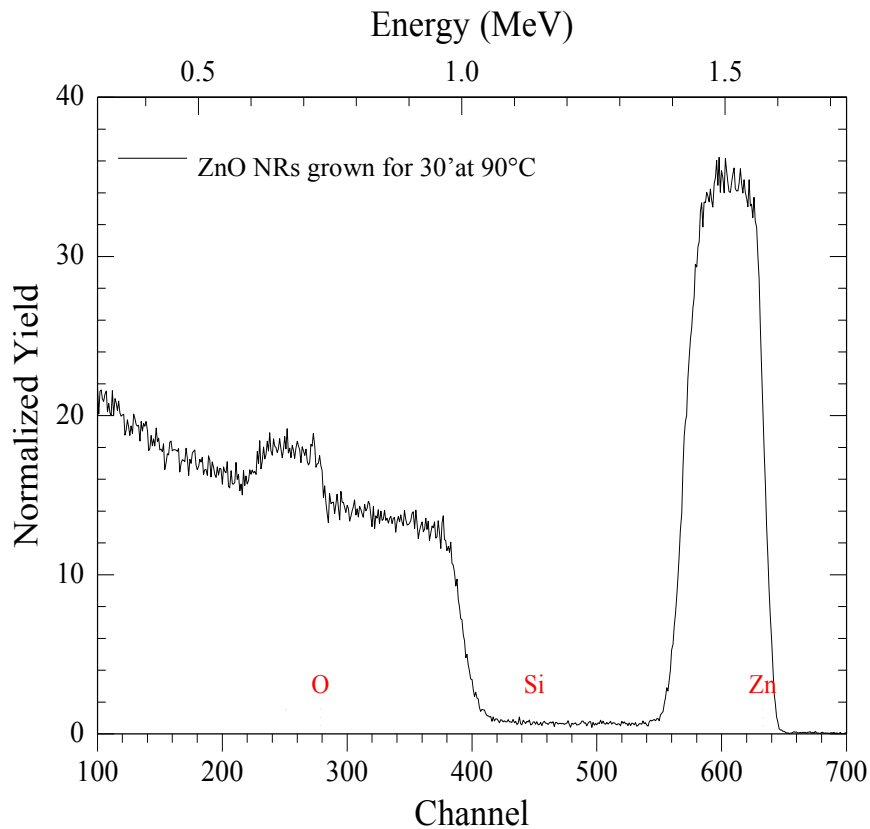
Figure 2.10: RBS spectrum of a ZnO NRs film grown by CBD for 30'at 90°C with a pH solution 5.7.

The structural characterization was also performed by using High Resolution X-Ray diffraction (HR-XRD: D8Discover Bruker AXS) using a $Cu_{k\alpha}$ source, in symmetric geometry configuration. The XRD pattern reported in Figure 2.11 demonstrates that the ZnO nanorods have a clear preferential orientation along [0001] direction as evidenced by the intense diffraction peak at 2θ=34.4° related to (0002) plane.
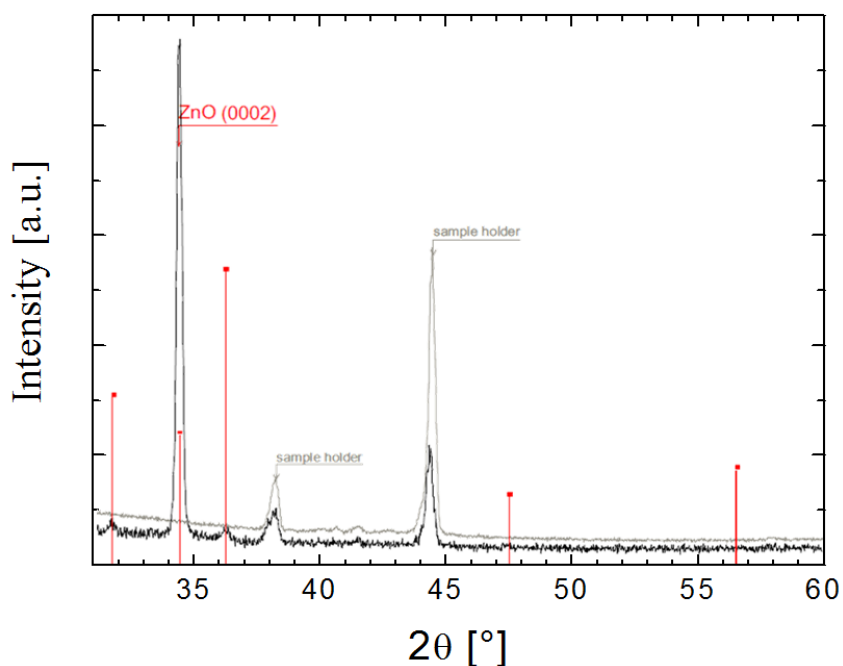
Figure 2.11: X-ray diffraction patterns of ZnO NRs deposited on Si at 90°C, pH 5.7 for 1h.

The ultraviolet and visible photoluminescence (PL) measurements of as-grown nanorods arrays were performed in air, at room temperature, by pumping at 1.5 mW the 325 nm line of a He-Cd laser chopped through an acousto-optic modulator at a frequency of 55Hz. The PL signal is collected and analyzed by a single grating monochromator, detected with a Hamamatsu visible photomultiplier. The spectrum has been recorded with a lock-in amplifier using the acousto-optic modulator frequency as a reference. As Figure 2.12 shows, the spectrum consists of two peaks, one in the UV region centered at 382 nm (3.24 eV) corresponding to the near band edge emission and the other one consisting of a broad emission related to defects energy level in the bandgap. The PL signal reported in Figure 2.12 (refers to NRs grown by CBD having diameter~60nm) is comparable with PL spectra of ZnO NWs grown by high-temperature synthesis method (see for example Figure 1.6 and 1.7).
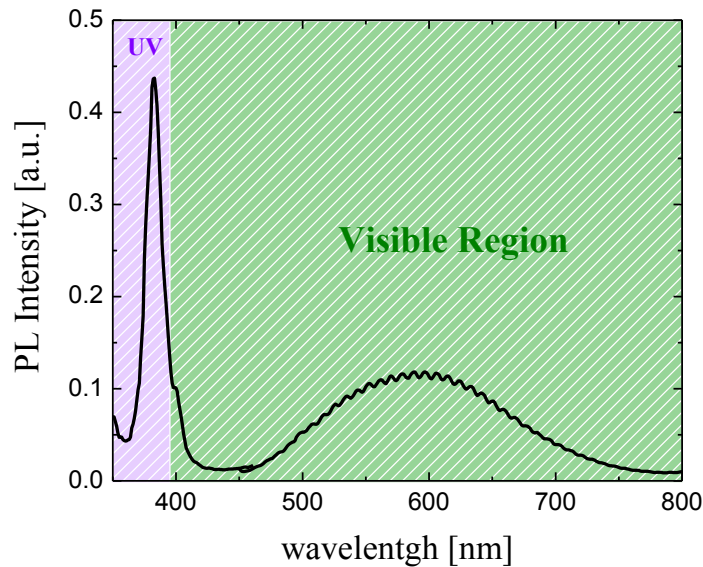
Figure 2.12: Room temperature PL spectrum for as-grown ZnO NRs array deposited on Si at 90°C, pH 5.7 for 1h.

2.3   Growth Kinetics

Time and temperature evolutions of the lateral size have been investigated, keeping fixed the other synthesis parameters (reagents concentrations and solution pH).

As reported in many studies [94], the formation of ZnO *via* CDB can occur at temperature as low as 65 °C. We have chosen to examine the temporal trend of the lateral dimension at that temperature by ranging the deposition time from 5 minutes to 2 hours. The average diameter (defined as the largest circumference inscribed in the hexagonal section of NR) of the nanorods was extracted by SEM image analysis.
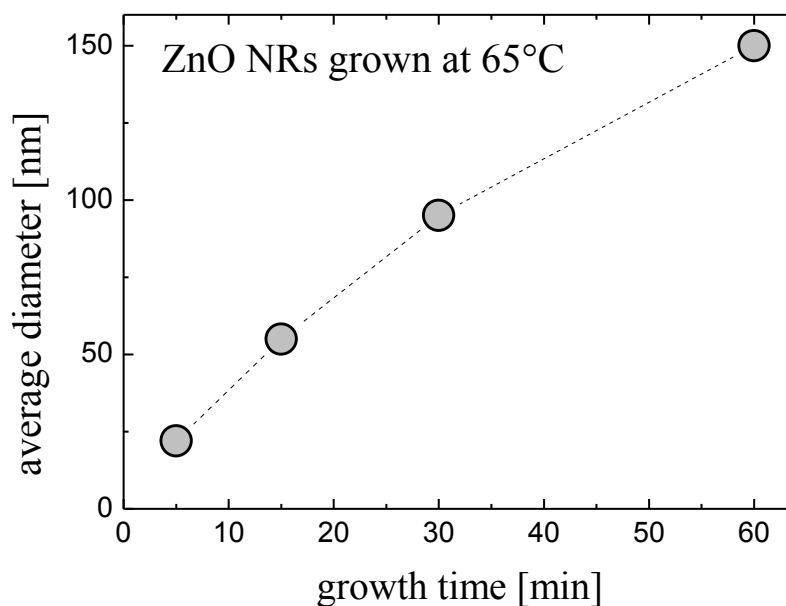
Figure 2.13: Nanorods average diameter as a function of the deposition time. The syntheses were carried out at 65°C. Error bars are included in the symbols size.

Two linear regions can be located in the curve reported in Figure 2.13 : after 30 minutes the lateral growth seems to slightly drop. Indeed, several kinetics tests have shown that the NRs size scales linearly with growth time up to a certain moment (dependent on the bath conditions) after which the growth rate decreases. As stated in the Section 2.2.1, the average distance among ZnO seeds is 60 nm so, assuming that each nanorod comes from a single seed, as soon as the nanorod reaches a lateral dimension of 100-120 nm, a further lateral growth will be affected by the presence of neighbors rods. At this point it may happen that two or more nanorods fuse together. The graph in Figure 2.13 does not show the value of the lateral size of the nanostructures grown in 2 hours long synthesis because the nanorods merging is such that the evaluation of an average diameter of a single NR becomes meaningless; contiguous nanorods seem to connect each other in a

common crystallographic orientation driving by a mechanism similar to the oriented attachment [98, 124, 125] and a spiral growth phenomenon begins to dominate, as shown in Figure 2.14.
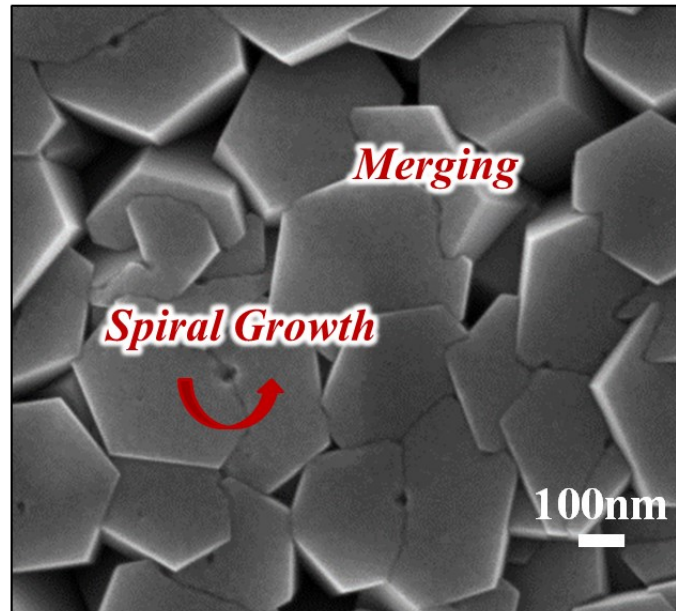
Figure 2.14: SEM image of ZnO NRs grown by CBD for 2h in a chemical bath kept at 65°C. Merging and spiral growth phenomena are evidenced.

The trend of the average diameter has been studied also as a function of the growth temperature. Four different temperatures were probed (65, 80, 85, 90 °C) while the duration of the deposition has been set to 1 hour. In Figure 2.15 it is evidenced that increasing the growth temperature, the lateral growth rate decreases and, as a consequence, the probability of the NRs merging is reduced. The lateral size ranges from 150nm for nanorods grown in a chemical bath kept at 65°C to 60 nm in the case of 90 °C. This is consistent with the result presented in literature[126, 127].
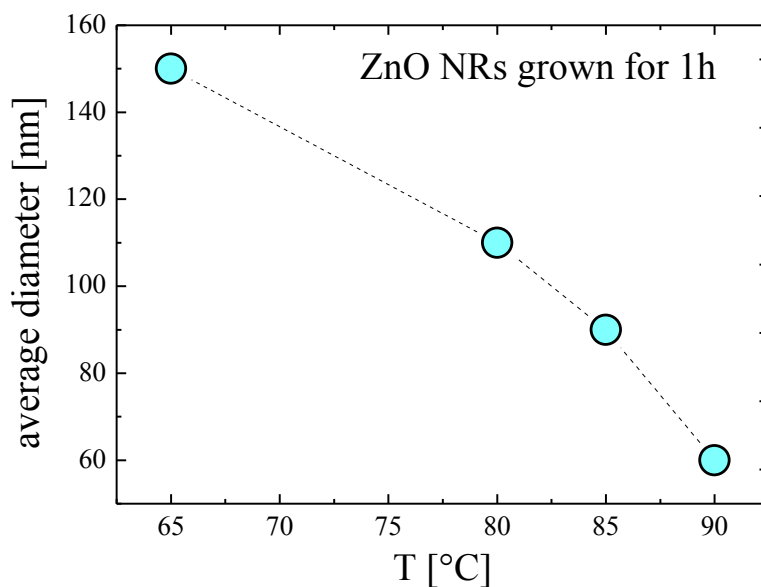
Figure 2.15: Influence of the growth temperature on the average diameter reached by ZnO NRs in 1 h long synthesis. Error bars for height are as large as the symbols size.

A summary diagram of the results discussed so far is shown in Figure 2.16. Increasing the deposition time, at temperature of 65°C the lateral growth is observed until neighbors nanorods merge. Increasing the growth temperature (1 hour long deposition) well-separated nanorods can be obtained since the lateral growth rate decreases. Limiting merging phenomena in favor of the formation of well-defined nanorods represents a key aspect for many applications. In this regard, it is clear that the optimum bath temperature is 90°C, so further investigations of the growth kinetics will be presented for this temperature.

To study the vertical growth kinetics at 90°C, we measured the height of NRs obtained after different durations of CBD. The result is reported in Figure 2.17(a).
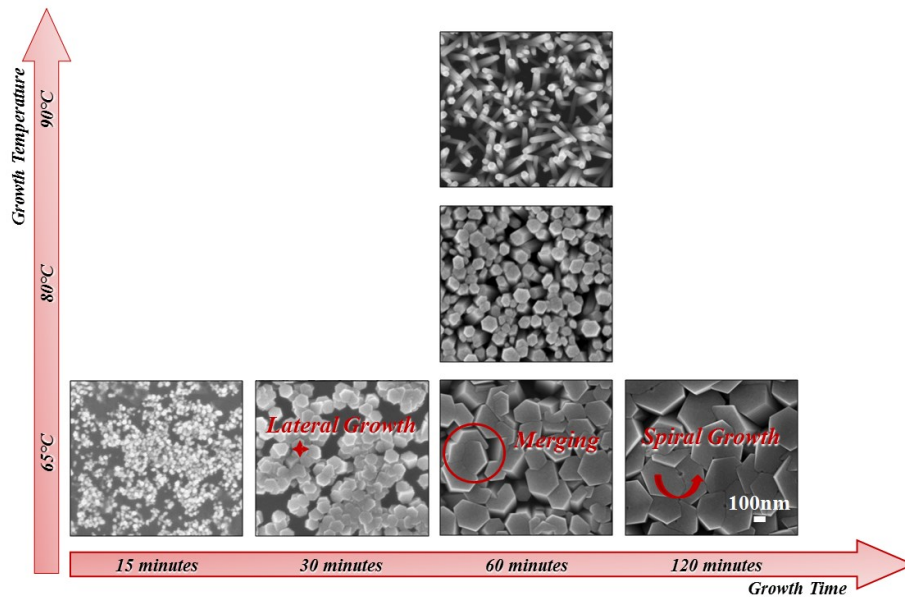
Figure 2.16: Summary diagram of the dependence of nanorods morphology on the growth time and temperature. Scale bar is the same for all the images.
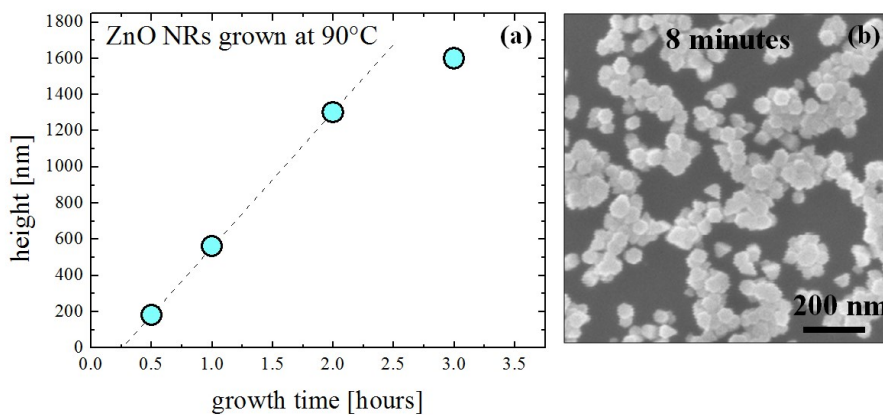
Figure 2.17: (a) Time evolution of NRs height (growth at 90°C, pH 5.7). Dashed line is the linear fit to extract growth rate and time offset, for data up to 2 h growth time. Error bars for height are as large as the symbols size. (b) SEM plan view of ZnO NRs grown at 90 °C for 8 minutes.

In many experimental tests, we have always observed that the NRs height increases proportionally with growth time, up to a maximum time of 2 h. This can be related to the change in Zn^{2+} ions concentration in the solution, as reported in ref [92]. For prolonged growth time, the concentration of Zn^{2+} ions in solution starts to decrease, leading to a lower NR vertical growth. So we have focused our attention on the 0−2 h growth time interval. In this time range we observed no significant lateral growth: the samples show ZnO NRs as large as ~50 nm from the beginning up to 2 h. The vertical growth rate can be determined with a simple linear fit and it was found that the growth rate is 12.5 nm/min. In addition, a systematic time offset (of about 15 min) is detected before the beginning of the vertical growth. The origin of this time offset can be explained by analyzing the early stages of the synthesis. We observed by SEM analysis the presence of ZnO NRs after 8 minutes growth, with a fairly low substrate coverage, Figure 2.17(b). The micrograph frames a transitory phase between the starting seed layer and a fully compact array of NRs uniformly covering the substrate. This is obtained after an incubation time corresponding to the time offset measured in the vertical growth rate analysis. A linear trend in the vertical growth can be reached after the incubation time. The vertical growth kinetics was analyzed also for the synthesis involving higher HMTA concentration (50mM) and it is reported in Appendix. In this case, the vertical growth rate resulted 13.0 nm/min. This means that by increasing the HMTA concentration, the hydrolysis equilibrium of $Zn^{2+}_{(aq)}$ is not significantly changed.

2.4   Role of HMTA

Some work demonstrated the control of ZnO morphology through the tailoring of the bath chemistry. We have conducted several experiments varying the HMTA concentration (12.5, 25 and 50 mM) and keeping fixed (25 mM) the concentration of zinc nitrate, with the aim to achieve a better understanding of the effect on the final structural properties. Figures 2.18 (a-c) show the SEM analysis of ZnO NRs in plan and cross view, evidencing that there is a strong dependence of the obtained morphology on the amount of HMTA. All the samples were grown for 1 h at 90 °C, and the measured

pH was 5.7. For 50 or 25 mM HMTA, a dense array of ZnO nanorods is obtained, with well-aligned and separated nanorods (40−50 nm wide, 600−700 nm high). The array is composed of ZnO nanorods with the well-known prism shape and hexagonal section with a flat top. If 12.5 mM HMTA is used, a remarkably different structure is obtained, as ZnO platelets (100 nm wide and 80 nm high) form, merged each other to form an almost continuous film. In this case, the height is even smaller than the lateral size, and moreover a large number of defects arose at the junction between these randomly oriented platelets. Thus, it is clear that there is a lower limit in the HMTA concentration over which the growth is biased toward the rodlike structure. Still, no difference in the pH of the solution is observed among the three cases; thus, the rodlike growth cannot be due only to the OH$^-$ release coming from the HTMA or ammonia protonation (see Equations 1-5(a-b)).
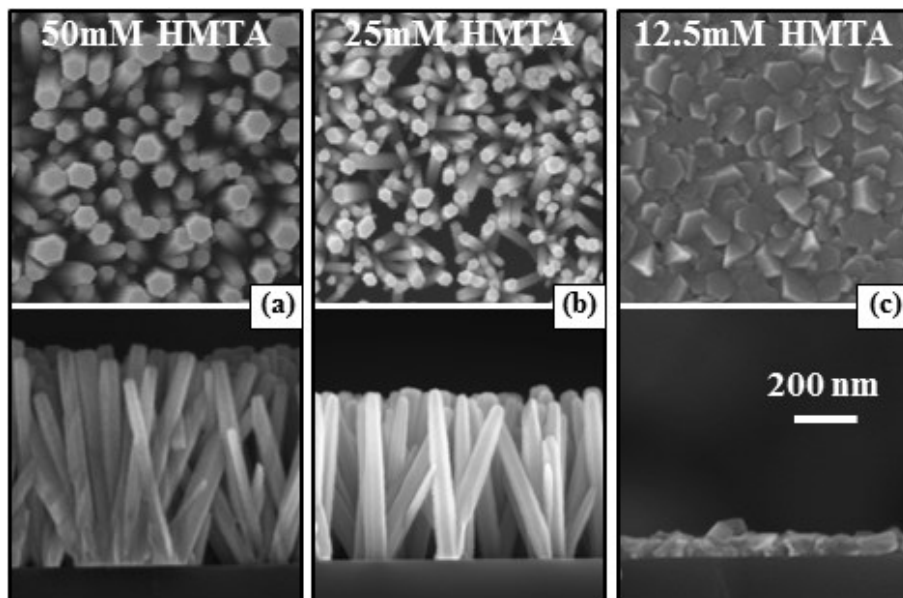
Figure 2.18: SEM images of the plane (top panel) and cross-sectional (bottom panel) views of the ZnO NRs grown with a zinc nitrate concentration of 25 mM and different molar concentrations of HMTA: 50 (a), 25 (b), and 12.5 mM (c). The growth temperature and time were 90 °C and 1 h, while the pH = 5.7. The scale bar is for all images [128].

The role of the pH value in ZnO NR growth by CBD has been largely discussed, [90, 91, 99, 116, 129]] with a general consensus that by changing pH different ZnO nanostructures can be formed. In this work, we have set the pH of the chemical bath at 5.7, with HMTA acting as pH regulator. In order to clarify if HMTA has any other role beyond that of pH regulation, we replaced it with a simpler amine, propylamine (PA). pH regulation can also be achieved by using inorganic salt, but we decided not to use them as they are known to affect morphology of oxide nanostructures in low-temperature solution growth [128]. Figure 2.19(a) reports the pH values of a 25 mM solution of Zn nitrate kept at 90 °C with different concentration of HMTA or PA. Without any amine, the Zn nitrate solution is acidic (pH = 4.2) due to the hydrolysis of $Zn^{2+}_{(aq)}$ complex. HMTA shows a strong pH regulation activity, quickly stabilizing the pH at 5.7 in the 12.5−25 mM range of HMTA concentration. The behavior of PA at low concentration is similar, while for PA concentration larger than 50 mM, pH increases up to 9. In particular, a 35 mM PA solution has a pH= 5.7 (indicated by vertical arrow in Figure 2.19(a)). In principle, if the role of HMTA is only to keep the pH = 5.7, using another reagent capable of ensuring the same pH condition should permit the synthesis of zinc oxide nanostructures with morphological features similar to those obtained by employing HMTA. Figure 2.19(b) shows the plan view of the CBD with 25 mM zinc nitrate and 35 mM PA solution. No nanorods or platelet structures were found. Given this results, we tried to repeat the growth by adding a small amount of HMTA. Figure 2.19(c) reports the SEM images in plan (top panel) and cross (bottom panel) of the ZnO nanorods obtained combining 35 mM PA and 12.5 mM HMTA (with a fixed 25 mM Zn nitrate). Under such conditions, very high and thin ZnO nanorods were obtained. It is worth noting that the same amount of HMTA (without PA) gave the merged ZnO platelets (Figure 2.19(c)). This indicates that ZnO NRs can be obtained even if a low amount of HMTA is used, as long as another pH regulator is present.

64
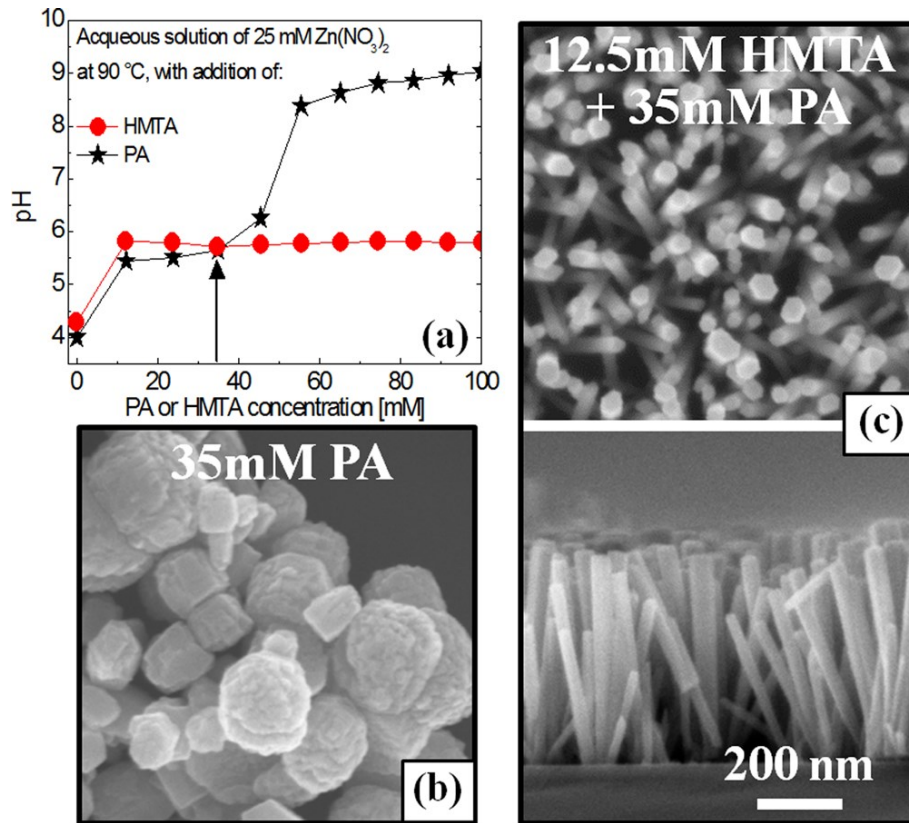
Figure 2.19: 3. (a) pH measured in an aqueous solution of Zn nitrate (25 mM) kept at 90 °C with different concentration of HMTA (close circles) or PA (stars). (b) SEM plan view ZnO nanostructures grown with 35 mM PA (Zn nitrate concentration of 25 mM, temperature of 90 °C, growth time of 1 h, pH = 5.7). (c) SEM images of the plane (top panel) and cross-sectional (bottom panel) views of the ZnO NRs grown with 12.5 mM HMTA and 35 mM PA (Zn nitrate concentration of 25 mM, temperature of 90 °C, growth time of 1 h, pH = 5.7). The scale bar is for all images [128].

Figure 2.20 provides an overview of the morphological features of ZnO NRs grown with different concentration of HMTA, with and without PA. The height and the lateral size were extracted from SEM images (error bars are of the same size as the symbols size). When only HMTA is used, higher HMTA concentration leads to significant increase in aspect ratio (AR),

65

ranging from about 0.7 (12.5 mM HMTA) to about 15 (50 mM HMTA). The combination of PA and 12.5 mM HMTA (stars) leads to height, lateral size, and AR comparable to those obtained with higher amount of HMTA. This effect of PA can be explained if a double role of HMTA is assumed: primarily it is a pH buffer, while its secondary role is to induce the rodlike growth of ZnO. In fact, looking at Figure 2.19(a), 12.5 mM HMTA turns out to be high enough to maintain pH at 5.7, but in this case no ZnO nanorods are obtained, implying that most or all of the HMTA is used up in pH regulation. When more HMTA or PA is added, ZnO nanorods appear. HMTA secondary function of biasing anisotropic growth of ZnO along the c-axis can be related to the preferential attachment of chelating HMTA molecules to the lateral faces of ZnO NRs [122]. HMTA can bind to nonpolar ZnO crystal surfaces by means of at least two mechanisms: a dative covalent bond between the basic N donor atoms and the acidic Zn^{2+} site or a hydrogen bonding between the tertiary ammonium cations and the O^{2-} crystal ions. Any of them can lead to a steric hindrance effect that hinders the lateral growth of the ZnO NRs. [104, 130, 131]. This explanation is in apparent contrast with ref. [116] where it is stated that HMTA does not adsorb on ZnO nanoparticles film. However, they used very low HMTA concentration (1 mM), and the HMTA absorption test was carried out at temperature well below 90 °C. At these conditions, HMTA adsorption and bonding to ZnO may not be favorable. Our results indicate that for typical ZnO NR growth condition (90 °C, pH = 5.7, HMTA=25 mM) a clear steric hindrance effect induced by HMTA cannot be ruled out.
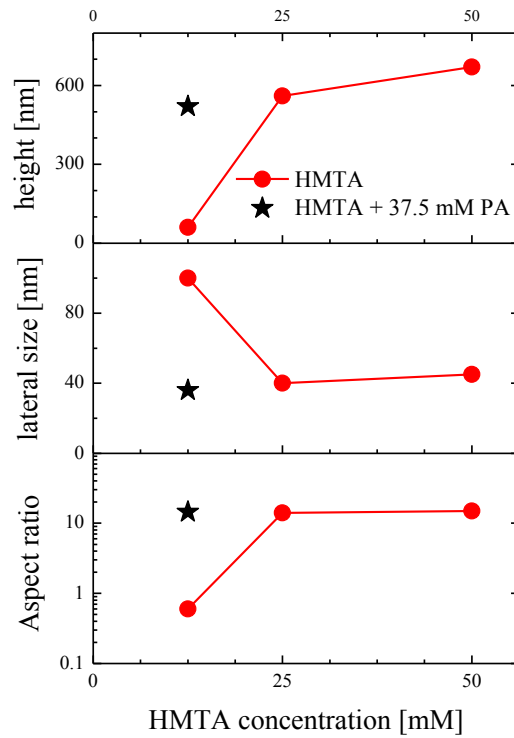
Figure 2.20: Circles refer to height (top), lateral sizes (medium), and aspect ratio (bottom) of ZnO NRs grown with different HMTA concentrations. Stars refer to ZnO NRs grown with HMTA (12.5 mM) and PA (35 mM). In all cases, Zn nitrate concentration was 25 mM, temperature was 90 °C, growth time 1 h, and pH = 5.7 [128].

2.5   Steric Hindrance Effect

Structural analyses were performed on ZnO NRs grown with 25 or 50 mM HMTA or with the combination of 12.5 mM HMTA and 35 mM PA by using a transmission electron microscope (TEM, JEOL ARM200CF), operating in conventional TEM (CTEM) and diffraction mode. In particular, in order to study the morphology of the NRs below the surface of the film, the NRs array was embedded by using an epoxy resin and then sliced up,

extracting a plane of observation about 100 nm above the substrate. All the TEM images refer to this kind of slice.
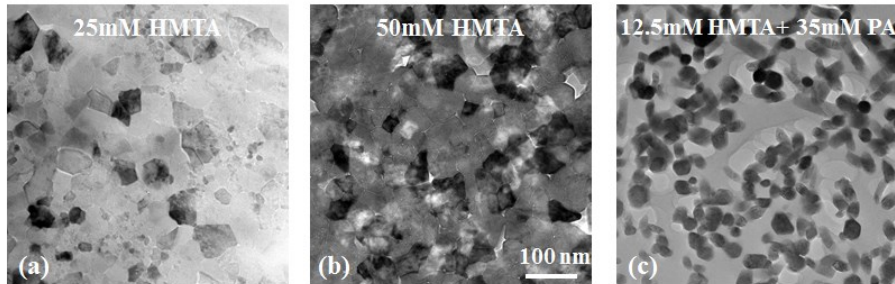
Figure 2.21: TEM images of a slice extracted 100 nm above the substrate of ZnO NRs samples grown with 25 mM HMTA (a), 50 mM HMTA (b), or 12.5 mM HMTA+35 mM PA (c) (Zn nitrate concentration of 25 mM, temperature of 90 °C, growth time of 1 h, pH = 5.7). The scale bar is for all images [128].

Figure 2.21 shows the bright field transmission electron microscopy (BF-TEM) images of ZnO NRs grown with 25 mM (a), 50 mM (b) of HMTA, and with the combined use of 12.5 mM HMTA and 35 mM PA (c). NRs with [0001] zone axis aligned with the line of sight appear with darker contrast and sharper edges. As shown by SEM images in Figure 2.19, not all NRs are properly perpendicular to the substrate, so some misalignment occurs
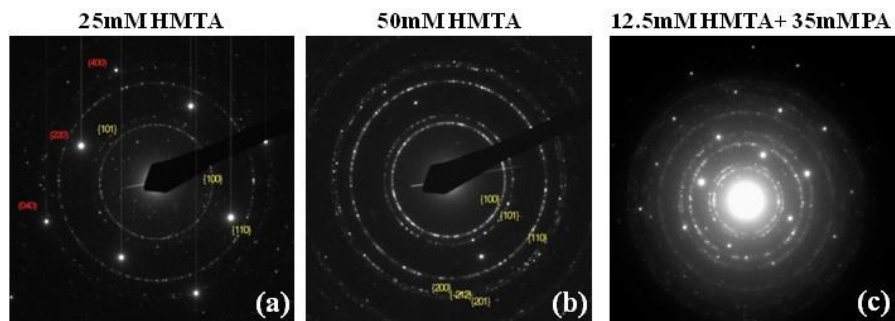
Figure 2.22: Selected Area Diffraction (SAD) patterns of TEM images of ZnO NRs grown with 25mM HMTA (a), 50mM HMTA (b), or 12.5mM HMTA+35mM propylamine (c) (Zn nitrate concentration of 25 mM, temperature of 90°C, growth time of 1 hour, pH=5.7) [128].

68

The selected area diffractions (SAD) patterns of TEM images are reported in Figure 2.22. This analysis and the extracted interplanar distances show that NRs are consistent with a wurtzite ZnO crystal, with white rings (green labeled) corresponding to [100], [101] and [110] axis directions, going from center to periphery. Spots with red labels in Figure 2.22(a) are referred to the diffraction spots of the c-Si substrate, and are disposed with a square lattice. The SAD shows that a predominant <0001> growth direction occurs for the NRs. It is clear that large differences arose among the three samples in terms of NRs density, dimension and uniformity. In order to investigate this aspect, we calculated the size distribution (Figure 2.23) of ZnO NRs both on the top plane and at 100 nm (bottom plane, hereafter) above the substrate, using SEM and TEM images analyses. Although two different techniques have been used on top and bottom of NRs, a fair comparison can be done and many reliable information can be drawn. For each sample, the areal density of NRs is reported, for both planes. In the case of only HMTA, the NR density clearly decreases from the bottom plane to the top one, in particular for the 25 mM HMTA sample. The same sample, moreover, shows a markedly larger size distribution at the bottom plane in comparison to all the other samples and the most representative size (35−40 nm) at the top plane is larger than the most representative size (10−20 nm) at the bottom plane. This may indicate that most of the ZnO NRs present at the bottom do not reach the top plane, perhaps suppressed during the growth. Another explanation is that merging of small NRs probably occurred by means of crystal coarsening or oriented attachment. The 50 mM HMTA NRs behaves slightly different, as the average size slightly increases from the bottom to the top plane, with a decrease of the NR density. The HMTA + PA sample shows fairly the same average size among the two planes, with only a moderate reduction in the NR density. It should be noted that this sample shows the lowest reduction in NRs density going from the bottom to the top plane and that also at the bottom plane the NRs density is quite low (see Figure 2.21(c)). The value of NRs density at bottom plane (280 NRs/μm^2) is really close to the density of seeds, indicating that most probably the NRs growth started at the preexisting seeds. In the 25 and 50 mM HMTA cases, instead, the NRs density at the bottom plane is much larger, suggesting that NR nucleation should have occurred well above the seed density.
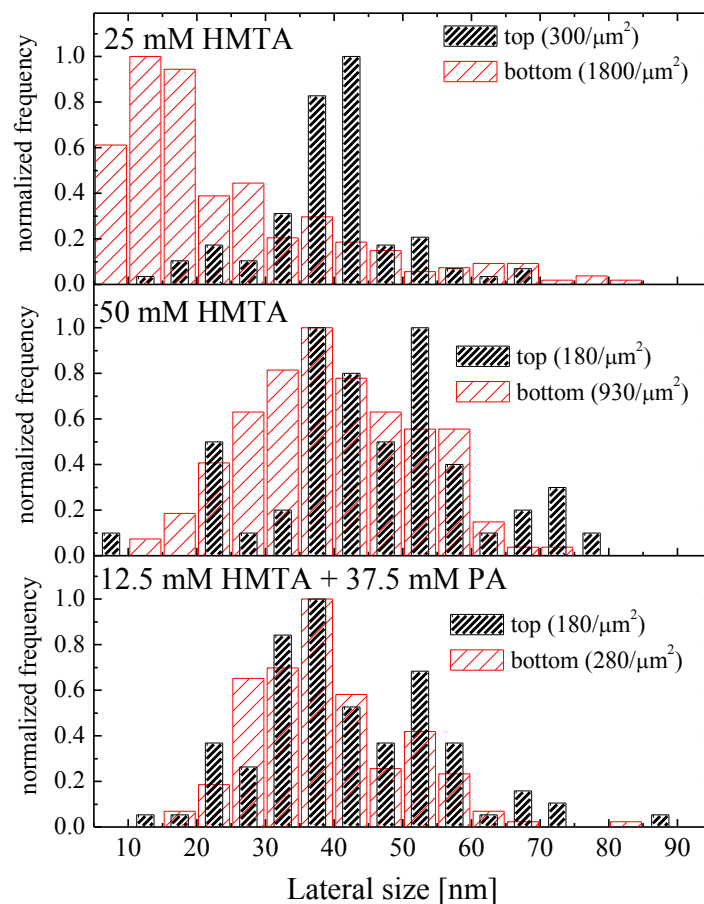
Figure 2.23: Size distribution of ZnO NRs in samples grown with 25 mM HMTA, 50 mM HMTA or 12.5 mM HMTA+35 mM PA, (Zn nitrate 25 mM, temperature of 90 °C, growth time of 1 h, pH = 5.7). Black and red histograms refer to the top or bottom (100 nm above the substrate) planes, as depicted in the drawing. NRs density per µm2 are also reported in the legend for each.sample, at the bottom and top planes [128].

In general, for the HMTA + PA samples ZnO NRs growth seemed to occur without any merging or NR suppression. These results can be interpreted with the steric hindrance effect. Basically, there is a sort of dynamic equilibrium among attached molecules (HMTA*) and molecules dispersed

70

in solution. When only 25 mM HMTA is used, the HMTA concentration in the residual solution at the bottom part of NRs during the growth becomes less and less, shifting the equilibrium toward molecules dispersed in solution. This reduces the HMTA* amount and consequently the steric hindrance effect. Merging phenomena can then occur. As the HMTA is increased, a more controlled growth occurs with 50 mM HMTA or even better with the HMTA + PA combination.

To counterprove the HMTA-induced steric hindrance action, a double-step synthesis test was carried out with HMTA concentration varied during the growth. Two seeded substrates were immersed in an equimolar solution (25 mM) of zinc nitrate and HMTA at 90 °C (pH = 5.7). After 1 h, one sample was extracted, rinsed, and dried, and a solution of 25 mM zinc nitrate (preheated heated at 90 °C) was added to double the original volume. As a consequence, the nominal HMTA concentration was then halved (12.5 mM) while maintaining that of zinc nitrate at 25 mM. The diluted solution had pH = 5.7, as expected. The second substrate was kept in the diluted solution for a further 30 min, then removed, rinsed, and dried. Figure 2.24 reports the results of this double-step synthesis test. After the first growth, ZnO NRs (Figure 2.20(a)) exhibit an average lateral size of 40 nm and a height of 540 nm. The second step (Figure 2.20(b)) surprisingly did not give any extra height (as observed by cross SEM images, not reported) but only a significant lateral size growth (from 40 to 100 nm), with several evidence of NR merging (red circles in Figure 7b). This scenario further confirms the steric hindrance action of HMTA, giving an explicit evidence that the NRs anisotropic growth strongly depends on the HMTA concentration. After the dilution, the amount of HMTA becomes so low that growth along the c-axis is essentially suppressed while only lateral growth occurs on the side walls of NRs.
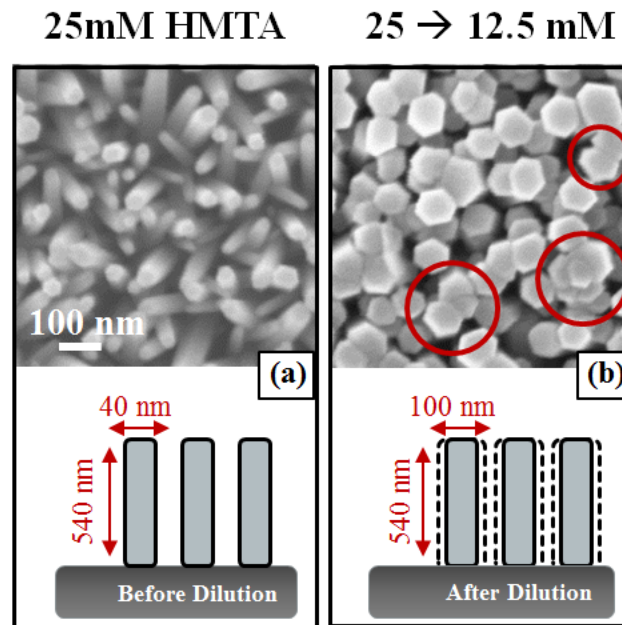
Figure 2.24: SEM plan views of ZnO NRs grown with 25 mM HMTA for 1 h (a) or with 25 mM HMTA for 1 h plus 12.5 mM HMTA for further 30 min (b) (Zn nitrate concentration of 25 mM, temperature of 90 °C, pH = 5.7). Red circles indicate merging ZnO NRs, while drawings below represent height and lateral size of NRs before and after HMTA dilution. The scale bar is for all images [128].

2.6 Conclusions

In this chapter, a systematic study of the structural properties and of the growth kinetics of ZnO nanorods synthesized by chemical bath deposition is presented and discussed. The precise synthetic conditions for ensuring a high degree of control and reproducibility were identified as well as the temperature and deposition time ranges suitable for growing high quality nanostructures. The investigation of the role of HMTA in the chemical bath deposition of ZnO nanorods allowed to conclude that a lower threshold in the HMTA concentration exists in order to induce the

anisotropic growth of ZnO NRs along the c-axis. Beyond the well-established pH buffering activity, HMTA is shown to introduce a strong steric hindrance effect, biasing growth along the c-axis and ensuring the vertical arrangement, Figure 2.25. This twofold function of HMTA should be taken into account for avoiding detrimental phenomena such as merging or suppression of NRs, which occur at low HMTA concentration.

Figure 2.25: Illustration of the shaping effect of HMTA in ZnO NRs grown by CBD.

Chapter 3

Light Scattering with ZnO Nanorods

In this chapter, the forward light scattering by ZnO NRs grown by chemical bath deposition (CBD) on flat and transparent substrate is presented.

The structural features of ZnO nanorods are analyzed and correlated to corresponding optical responses. The light scattering performance has been found to significantly increase with NRs longer than 1 μm and such a result is in qualitative agreement with theoretical prediction provided by a simple light scattering model.

The applicability of ZnO NRs film as low-cost light diffuser layer upon crystalline silicon (c-Si) solar cell is finally investigated. An enhancement of the light-current conversion efficiency has been achieved for wavelengths longer than 600 nm, attributable to the scattering of light by NRs array.

## 3.1   Nanostructures for cost effective Photovoltaics

Over the past decade, the constant increase of the global energy demand combined with the need to provide a viable and sustainable alternative to conventional fuels, have boosted the interest for renewable energy sources. In particular, solar energy stands out as the most promising candidate, being an almost limitless resource of the earth and relatively available in all the globe's surface. Among the different conversion technologies able to exploit the solar radiation, such as solar thermal or artificial photosynthesis, photovoltaic has the greater potential to become the major energy supply in the future, providing clean and affordable electricity. Although the photovoltaic effect is known since 1839 thanks to the experiments of Alexandre Edmond Becquerel on electrolytic cells, it found a physical explanation only in 1905, within the *quantum physics revolution*, through the photoelectric effect clarified by Albert Einstein. The first commercial silicon solar cell was realized in 1954 by Person, Fuller and Chapin at Bell Laboratories. Since then, the efforts of scientific research are aimed at improving the yield of photovoltaic systems in terms of conversion efficiency and manufacturing costs. In this regard, minimizing the thickness of the active materials represent one of the most promising route not only from the economy point of view but also for the decrease of the electrical losses during the photocarrier transport. In addition, thin film based technology permits a great versatility: thin film can be applied to almost all kind of substrate, also paper or flexible plastic, therefore particularly suitable for building integrated photovoltaic.

3.1.1   Light Trapping Approaches

Semiconductors are able to absorb a large part of the solar spectrum according to the value of their bandgap energy (E_g). For example, crystalline silicon exhibits an optical bandgap of 1.1 eV while amorphous silicon has higher bandgap (1.7 eV). The photons hitting the solar cell with energies above E_g can be absorbed and electron-hole pairs are formed within the material. The photogenerated carriers are then separated by the action of the

internal electric field (as in the case of a *p-n* junction) and collected to create electric current. The highest achievable efficiency is determined by intrinsic losses and, for the case of an ideal single junction device, the maximum thermodynamic efficiency is about 30%, as demonstrated by Shockley and Queisser in 1960 [132]. Moreover, especially for devices based on thin film, the decrease of the absorption coefficient α whit the increasing of the light wavelength represents a further limiting step for reaching high device performance. Figure 3.1 shows the trends of the absorption coefficient for crystalline, microcrystalline and amorphous silicon. In the visible range, the values of the parameter α are so high that the photons are easily absorbed in a single pass across the device. In the near infrared spectral region, as the energy of the light becomes comparable to E_g, the probability of absorption of photons strongly decreases. Therefore, the efficiency of the solar cell is affected by the weak absorption at longer wavelengths and this effect is particularly pronounced in thin film configurations where incoming light has a low probability to be absorbed during one single pass. Developing very effective photon management schemes is the key to maximize the light absorption probability even maintaining the minimal material use [133].

Nanostructures can play a crucial role in light trapping to increase the sunlight absorption in solar cell [134-136]. Firstly, the presence on the top of the cell of an effective antireflection layer allows to maximize the light entering into the cell. It has been demonstrated that nanostructures with appropriate morphological features can effectively reduce the reflectance of material with low absorption coefficient better than the conventional quarter-wavelengths thin films [137]. However, many problems related to nanostructuring hinder large-scale uniformity, fabrication costs and mechanical resistance.
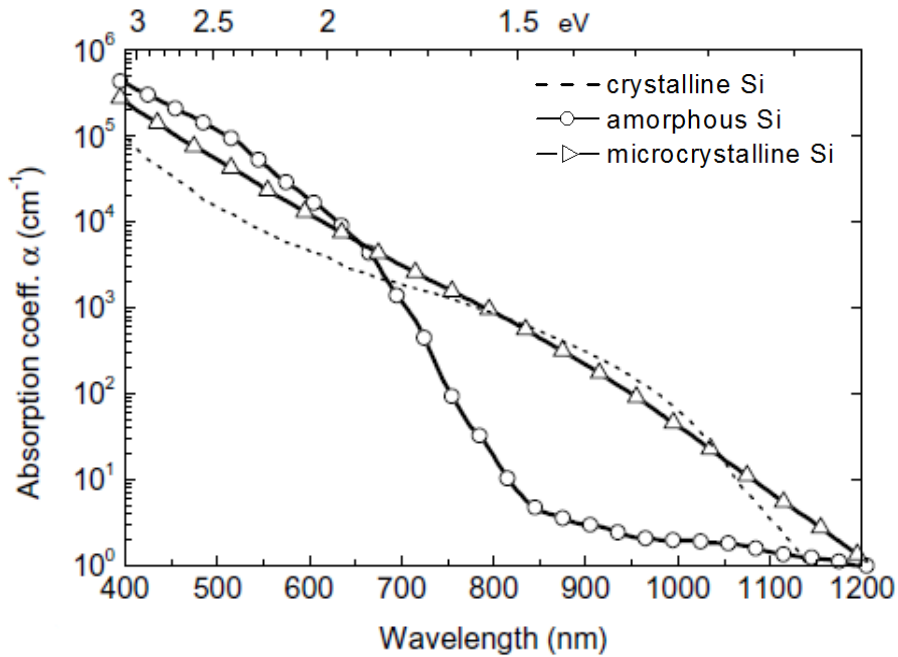
Figure 3.1: Absorption coefficient of crystalline (dashed line), amorphous (circles), and microcrystalline (triangles) silicon. Adapted from ref. [Muller2004].

Different approaches have been investigated to enhance the light absorption by confining light inside the active layer, such as photonic crystals, plasmonic nanostructures, and diffraction gratings [138-142]. Plasmonic nanostructures can be exploited in different ways to enhance the absorption in the photovoltaic layers, as shown in Figure 3.2(a-c). Metallic nanoparticles can serve as subwavelength scattering centers or work as subwavelength antennas by near-field enhancement. In addition, metallic gratings on the bottom of the cell can couple the incident sunlight in guided mode.
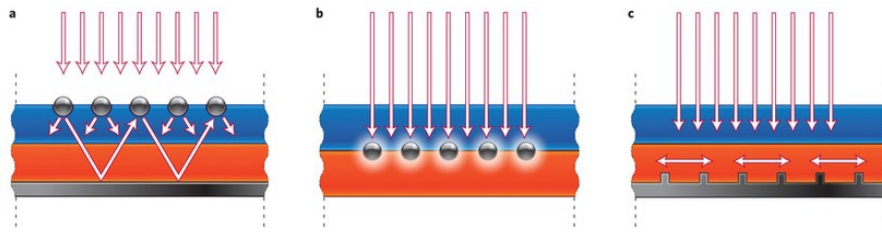
Figure 3.2: Illustration of light trapping mechanisms induced by plasmonic nanostructures: (a) scattering, (b) near-field enhancement, (c) waveguide modes. Adapted from ref [138].

Different geometry for diffraction grating have been investigated. Martins et al. have proposed a *supercell* grating able to suppress the diffraction orders that do not couple into the quasiguided modes and to enhance those ones able (Figure 3.3).
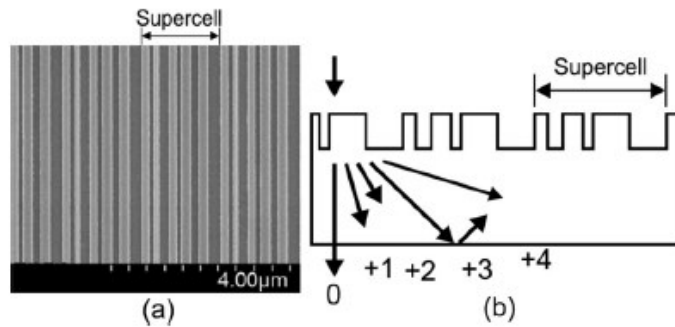
Figure 3.3: (a) SEM image of the supercell grating. (b) Schematic of operation principle: the diffraction orders that do not couple into quasiguided modes of the thin film are suppressed. Adapted from ref. [140].

Although these approaches seem promising from a theoretical point of view, the experimental evidences often have not confirmed the expectations. Moreover, their implementation cost might be too high for the relatively small enhancement of the solar cell efficiency they induce and, therefore, ill-suited for industrial scale.

Light scattering from highly textured interfaces is the most common way to improve the light management in the cells with *superstrate*

configuration as well as the presence of metallic back reflector in *substrate* configuration. The purpose of both approaches is to extend the light path beyond the thickness of the material in order to increase the internal absorption especially at energies corresponding to weak absorption. The deposition of intentionally roughened transparent conductive oxide (TCO) as front contact ensures a high electrical conductivity and a high transparency in the spectral region where solar cell typically operates. Figure 3.4(a) illustrates the cross section of a thin film silicon solar cell and the possible light scattering events at interfaces between neighboring layers. The ability to scatter the incident light of a TCO is related to the morphological features of the surface. In Figure 3.4(b) the SEM micrograph of a ZnO layer after chemical etching process is shown. In general, an appropriate choice of the deposition methods and of the post-growth processes allows the design of front electrodes with surface morphologies suitable for effective light scattering.
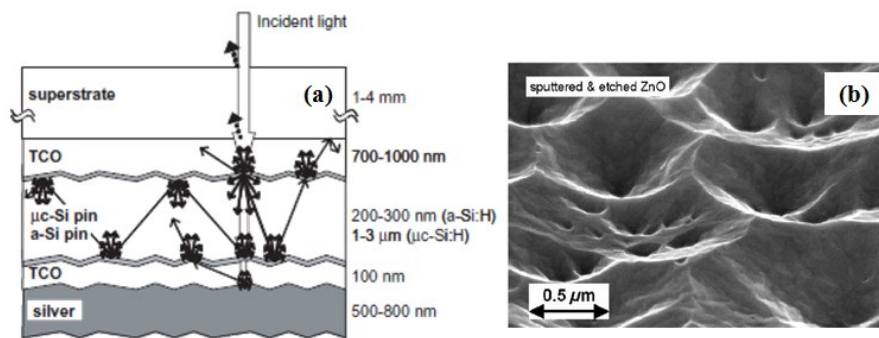
Figure 3.4: (a) Sketch of a Si thin film solar cell with superstate design. The arrows represent all the possible light paths and scattering events. (b) SEM image of magnetron-sputtered and texture-etched ZnO. Adapted from ref. [134].

Recently, strong efforts have been taken to improve the optical and electrical properties of ZnO-based materials since zinc oxide, unlike the conventional tin oxide (SnO_2), has the advantages of abundance in nature, non-toxicity and great potential to be deposited via large area and cost-effective techniques.

3.1.2 Light Scattering Performances of solution derived ZnO NRs

Despite the solar cell technology is mainly focused on sputtering and chemical vapor deposition techniques, several examples have been reported where low temperature solution-phase synthesis methods have been successfully employed. In particular, solution derived zinc oxide nanorods layers are shown to be profitably used to increase the efficiency of thin-film solar cells both as efficient antireflection coating [143-145] and as broadband light scattering transparent layer [146-148].

Ko and Yu [146] have reported, on urchin-aggregation inspired hierarchical nanostructures consisting in ZnO NRs grown by hydrothermal method on silica microspheres monolayer covered with Al-doped ZnO (AZO).
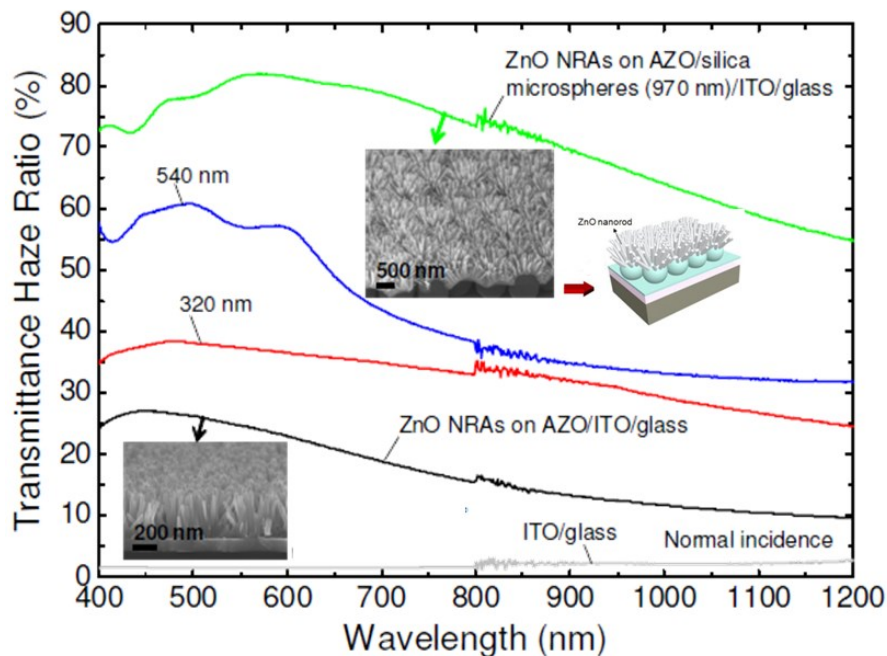
Figure 3.5: Transmittance Haze spectra of ITO/glass, ZnO NRs on AZO/ITO/glass, and ZnO NRs on AZO/silica microspheres of 320 nm, 540 nm, and 970 nm/ITO/glass, The insets show tilted-view SEM images. Adapted from ref. [146].

The transmittance haze spectra (diffused over total transmitted light) shown in Figure 3.5(b), have revealed that ZnO NRs grown on 970 nm silica

microspheres yield very high haze values about 80% - 60% in the wavelength rage of 400-900 nm. This represents a prime example of how different materials and synthesis methods could be well integrated into a single promising device.

By a low temperature (75°C) double-step electrodeposition method, Shinagawa et al. [147] have formed a layer of dense ZnO columnar grains with a (101)-faceted pyramidal tips on TCO substrate, whose light scattering effects give average haze values of about 50%, Figure 3.6. To provide a better insight into the possible improvement in solar cell performances, the authors tested the effects of the ZnO film with a pyramidally textured surface on a ZnO/Cu$_2$O solar cell (1.3–1.5 μm thick Cu$_2$O), achieving a 1.3 times higher short circuit current density (J$_{SC}$) than that using a non-textured ZnO.
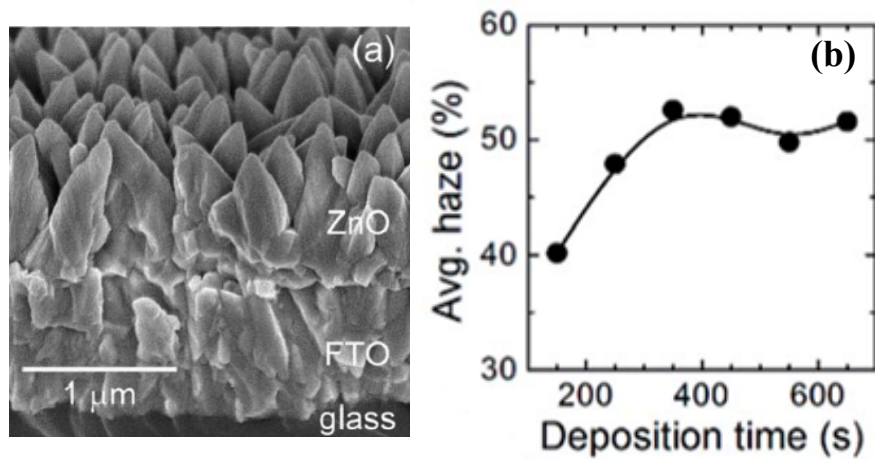
Figure 3.6: (a) SEM images of ZnO cylinder with pyramidal tip electrodeposited on fluorine tin oxide (FTO) substrate (second step deposition time 450 s) .(b) Variation of average haze values depending on the second step deposition time. Adapted from ref. [147].

A properly tuning of the size and shape of the nanostructures can promote the light scattering effect, as Nowak et al. [148] have demonstrated in their study on electrochemically deposited ZnO NRs arrays. In figure 3.7, SEM micrographs and the corresponding transmission haze spectra are

displayed revealing that the difference in morphology results in large variation of the optical response. The amorphous Si thin film solar cells grown on these ZnO nanorods (superstrate configuration) have evidenced a significant reduction in the cell reflectivity. Still, the ZnO NR arrays with the strong diffuse scattering (long and well-separated NR) have also caused significant electrical losses in the solar cell (low open-circuit voltage and low fill factor) cancelling out the benefits of the better optical performance.
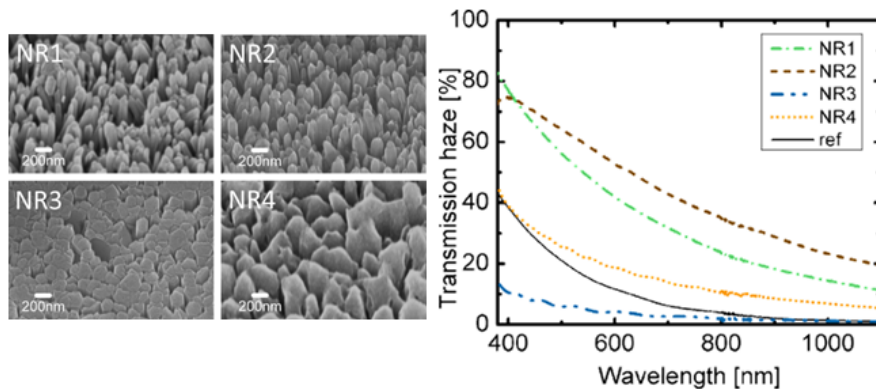
Figure 3.7: SEM images of ZnO NRs arrays grown with different electrochemical deposition parameter and corresponding transmittance haze spectra compared with a commercial TCO (ref). Adapted from ref. [148].

3.1.3   Decoupling the light diffuser layer: a new way

The implementation of high-haze layers in thin film solar cell is not a trivial question and, although ZnO NRs have clearly shown large potential in light management for sunlight-energy conversion, they may not have favorable physio-chemical properties for being a suitable substrate for the growth of the absorber layer. The high degree of roughness causes the inevitable creation of defects responsible for increased recombination probability in the photo-active material and consequent deterioration of the electrical properties of the entire device.
In this thesis, a novel approach is proposed, consisting in physically decoupling the ZnO light diffuser layer from the solar cell. This should

permit to keep flat the film, to avoid device performance degradation and, at the same time, to maximize the collection efficiency.

3.2   ZnO Nanorods on Transparent Substrate

3.2.1   Morphological and Structural Properties

ZnO nanorods arrays have been deposited on microscope glasses (2 x 2 cm^2) by chemical bath deposition. After substrate cleaning (ultrasonic baths of acetone, then isopropanol, followed by drying with N_2 gas) and seed layer deposition, three NRs samples were grown, by immersing the seeded glass in a 90 °C aqueous solution of 25mM zinc nitrate hexahydrate and 12.5 (NR1) or 25 (NR2) or 50 (NR3) mM hexamethylenetetramine for 1 hour. The geometry of nanostructures is known to dominate the light scattering behavior. Since the diffusion of the sunlight can be optimized by adequate design of the morphology of the nanostructures (diameter, length, density, etc.), an accurate structural characterization is required in order to find some correlation. Table 3.1 summarizes the morphological properties of the samples indicating the values for the length (l), lateral size (d), and aspect ratio (AR= l/d) of ZnO NR, as extracted from the SEM images reported in Figure 3.8(a-c). As expected, the morphology of grown ZnO structures is strongly affected by the HMTA concentration, as by increasing the amount of HMTA, longer and narrower NRs are obtained.

Sample	[HMTA]	l (nm)	d (nm)	AR	FWHM (°)
NR1	12.5 mM	120	280	0.4	/
NR2	25 mM	780	80	9.7	10
NR3	50mM	1300	60	21.6	11

Table 3.1: ZnO nanorod length (l), lateral size (d), aspect ratio (AR), and FWHM of rocking curves for the three ZnO NR samples synthesized with different HMTA concentrations.
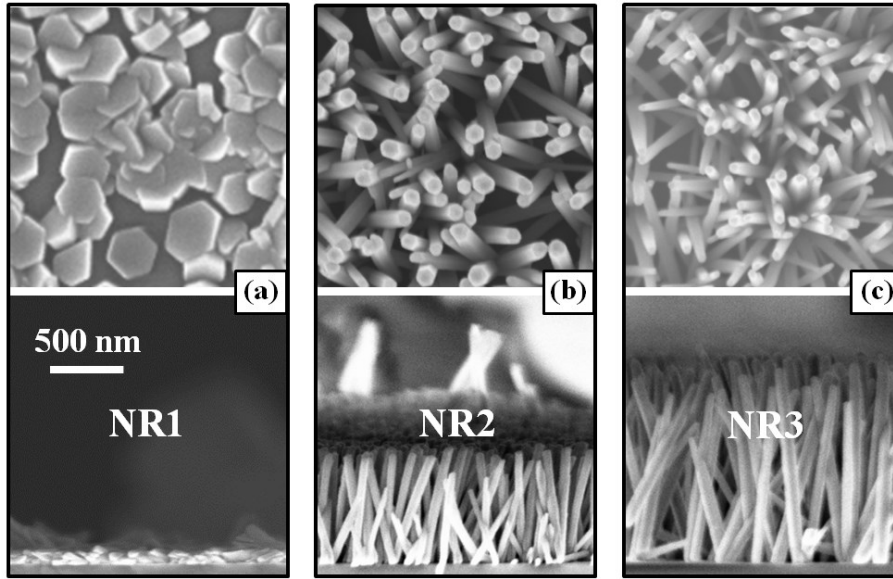
Figure 3.8: SEM images of the plane (top panel) and cross-sectional (bottom panel) views of ZnO NR grown with different molar concentrations of HMTA: 12.5mM for NR1 (a), 25mM for NR2 (b), and 50mM for NR3 (c). The scale bar is valid for all images [149].

ZnO NRs lattice structure and orientation have been studied by HR-XRD (D8Discover Bruker AXS, quipped with a $Cu_{k\alpha}$ source and thin film attachment; acquisition done in symmetric configuration). The diffraction patterns in Figure 3.9(a) reveal peaks from (10-10), (0002), and (10-1 1) planes of the ZnO wurtzite structure with different relative intensities depending on the HMTA concentration used. In order to give quantitative information about the growth axes of the ZnO NRs, the texturing coefficient J_{hkl} has been calculated:

$$J_{(hkl)} = \frac{I_{(hkl)}/I_{(hkl)}^*}{\sum_{hkl} I_{(hkl)}/I_{(hkl)}^*} \tag{3.1}$$

wherein the intensity of the experimental diffracted peaks (I_{hkl}) are normalized to the reference I_{hkl}^* values taken in a random poly-layer. The results are shown in Figure 3.9(b). In all cases, a preferential growth of ZnO NR along the wurtzite [0001] axis is observed, with growth axis

perpendicular to the sample surface. NR1 has the lowest degree of orientation along the [0001] direction, while NR2 has the highest degree of texturing along the [0001] direction, as evidenced by the intense diffraction peak at 2θ=34.4° related to the (0002) plane and the extremely weak signals due to (10$\bar{1}$0) and (10$\bar{1}$1) planes. Finally, NR3 is well oriented too, with a texturing value slightly lower than NR2.
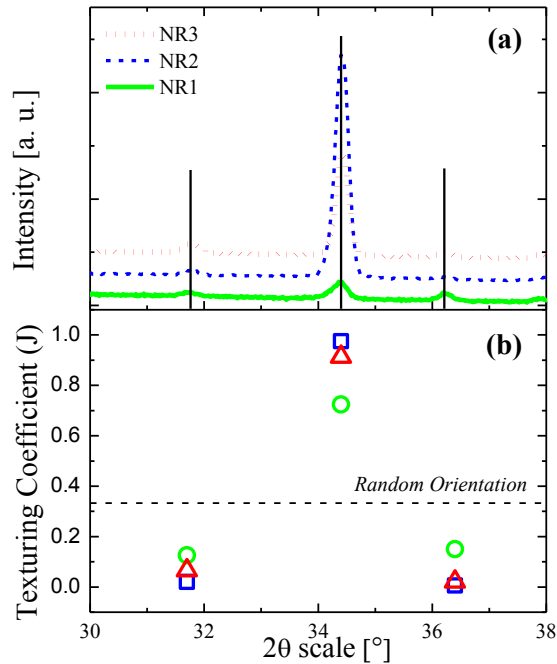
Figure 3.9: (a) X-ray diffraction patterns and (b) texturing coefficient values of ZnO NR deposited on glass. The black dashed line in (b) indicates the expected value of a randomly oriented ZnO layer [149].

The occurrence of a preferential growth was analyzed by the rocking curves shown in Figure 3.10 which describes the angular distribution of the [0001] growth axis with respect to the direction perpendicular to the sample surface. The full width at half maximum (*FWHM*) of the curve is a measure of the spread of the [0001] growth axis direction. The FWHM values for the samples are reported in Table 3.1 and indicate that the NR2 and NR3

samples have NR aligned around the vertical axis within an angular range of 10°-11°. The NR1 sample exhibits instead a flat distribution. The scenario on the spread of the growth axis is consistent with the morphology of the samples shown by the SEM images in Fig.3.8.
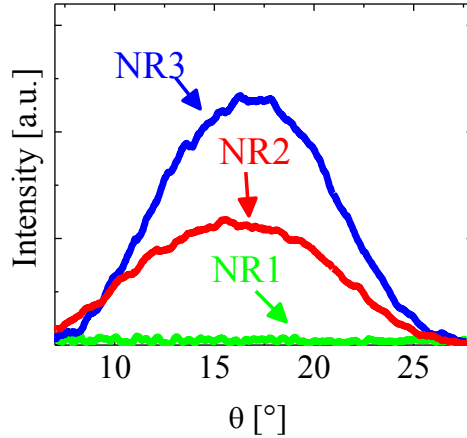
Figure 3.10: Rocking curves around the [0001] direction for the three samples [149].

3.2.2   Optical Analysis

In 1966, Tauc, Grigorovici and Vacu proposed a method to evaluate the bang gap energy of Ge amorphous by using optical absorbance [150]. A few years later, the method was extended for all amorphous semiconductors by Davis and Mott's study [151]. They concluded that the absorption coefficient depends on the photon energy ($h\nu$) and the bandgap E_g, according to the follow equation:

$$(\alpha h\nu)^{1/n} = A(h\nu - E_g) \tag{3.2}$$

where h is the Plank's constant, ν the photon's frequency and A a constant. Depending on the nature of the electronic transition, n can take different values: $n = \frac{1}{2}$ for direct transition, $n = 2$ for indirect transition. By

87

plotting $(\alpha h\nu)^{1/n}$ as a function of $h\nu$, E_g is determined by the x-axis intercept at the linear region of the plot. Although originally the "Tauc method" has been developed for amorphous materials, many studies have demonstrated its validity also for crystalline and polycrystalline semiconductors [152].

The optical properties of the samples have been measured using a UV-Vis Lambda 40 spectrophotometer with a 50mm integrating sphere that allows to detect the total transmittance and reflectance (T_{tot}, R_{tot}) as well as the diffused light in both transmission and reflection mode (T_{diff}, R_{diff}). Starting from such optical integrated measurements, the absorption coefficient has been calculated as:

$$\alpha = \frac{1}{d} \ln \frac{T_{tot}^S (1 - R_{tot})}{T_{tot}} \qquad (3.3)$$

where T_{tot}^S is the total transmittance of the glass substrate, R_{tot} and T_{tot} are, respectively, the total reflectance and transmittance of the samples. The experimental data of the absorption coefficient have been used to estimate the value of ZnO NRs optical bangap. Figure 3.11 reports the Tauc plot related to NR2 sample, calculated by setting $n = \frac{1}{2}$ in the equation 3.2, being zinc oxide a direct bandgap material. The x-axis intercept of the linear fit identifies a value for the optical bangap E_g= 3.2±0.1 eV, in good agreement with the data reported in literature [153].
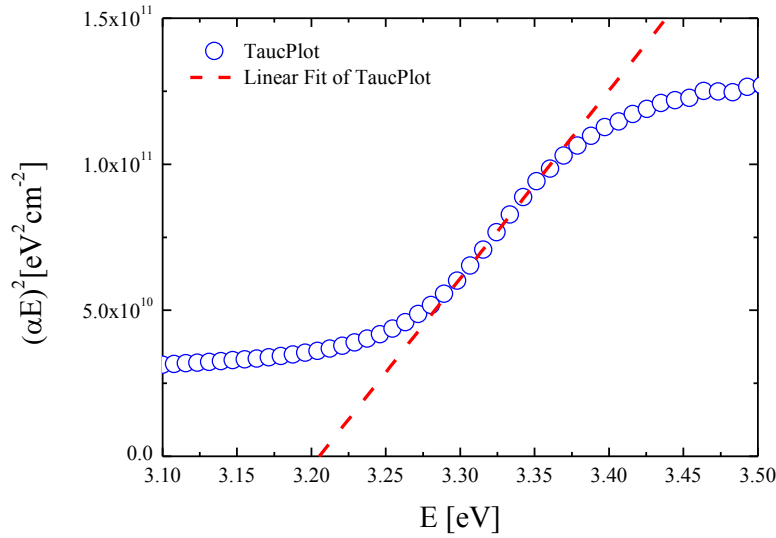
Figure 3.11: Tauc plot (circles) and relative linear fit according to the reported Tauc law (Eq 3.2) for NR2 sample.

In the Figure 3.12(a), the total and diffuse transmittance spectra for ZnO NR samples are shown. All the samples show very high T_{tot} (larger than 90%) in the 600–1100 nm λ range, with a cutoff at ~380 nm due to ZnO band-to-band absorption. In the 400–600 nm λ range, NR samples show a lower T_{tot} because of light reflection at air/glass interface and light absorption onset at ZnO bandgap energy. No antireflection coating was employed to further increase the transmittance in the investigated range. However, a significant portion of transmitted light is diffused at high angle. In order to estimate the light scattering effect, transmittance haze (H_T), defined as the ratio of diffused light to total transmitted radiation ($H_{T=}T_{diff}/T_{tot}$), is typically used. Fig. 3.12(b) shows H_T spectra for the three ZnO NR samples.
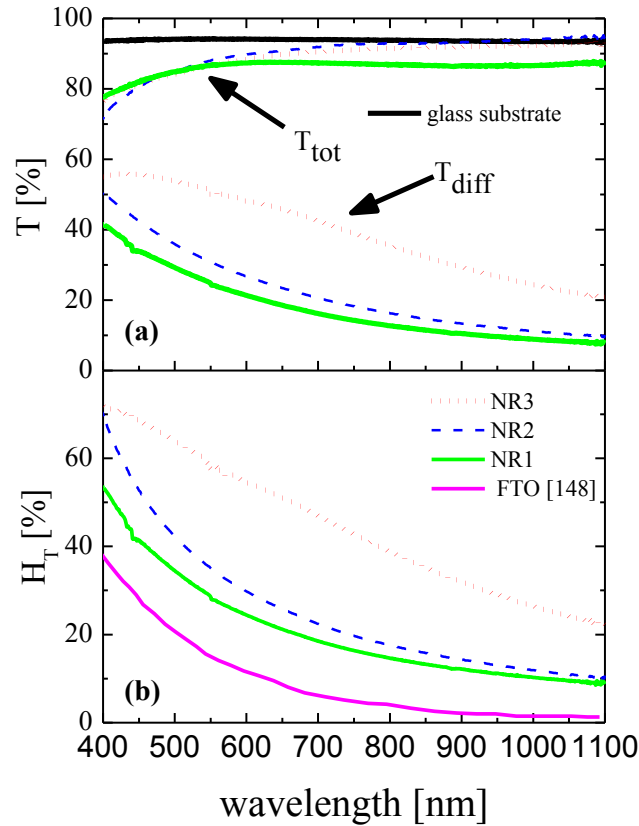
Figure 3.12: (a) Total and diffuse transmittance of ZnO NR samples and of microscope glass used as substrate. (b) Transmittance haze spectra of ZnO NR samples. For comparison, the transmission haze of a commercial textured FTO layer is reported [149].

The NR1 and NR2 spectra have a similar shape, with H_T higher than that of a commercial textured fluorine-doped tin oxide (FTO) layer [148]. The H_T spectrum for NR3 is even much higher, reaching a max value of 70% at 400 nm, as high as the highest haze values reported in the literature [147, 148]. Although there is a large difference in l, d, and FWHM, NR1 and NR2 samples show quite similar light scattering properties, which can be ascribed to the refractive index of ZnO rather than to the NR shape. On the other hand, NR3 shows a much higher transmittance haze, in spite of having rc-

FWHM and d values similar to those of NR2. Given the much longer NR, the haze improvement in the NR3 sample suggests a threshold in NR length over which the light scattering is effectively enhanced.

Light scattering simulations have been performed to investigate the role of the NRs shape, if any. Using the software MIST [154] we simulated the scattering of non-polarized light from a single cylinder of refractive index 2.0 (appropriate for ZnO in the visible range) immersed in vacuum (inset in Figure 3.13). The calculated differential scattering cross section (σ_s) was integrated over the forward hemisphere and averaged over different incidence angles θ_i [0°–10°] to account for the spread in the real samples.
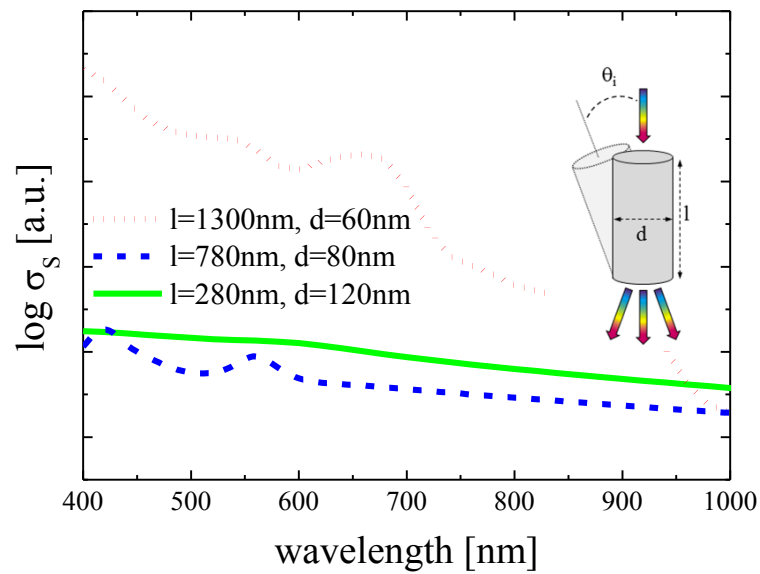
Figure 3.13: Calculated spectra of logarithmic differential scattering cross section (σ_s) for a single ZnO cylinder (diameter d, length l) immersed in air integrated over the forward hemisphere and averaged over incidence angle between 0° and 10°. The results of the calculations have been smoothed for clarity.

The results are reported in Figure 3.13 as log σ_s vs. wavelength, for lengths and lateral sizes equal to the experimental ones. Due to the presence of the

substrate and, above all, to the high density of the rods, which causes multiple scattering, we are prevented from a tight comparison between calculations and data. Nevertheless, the trend of the higher light scattering for the longer cylinder is in good agreement with the experimental data (Figure 3.12), confirming the hypothesis of a threshold in the ZnO NR length for a large improvement of the haze.

3.3   Effect of ZnO NRs light diffuser layer on c-Si Solar Cell

A crucial point is to ascertain if the presence of ZnO light diffuser layer does not entail a deterioration of the solar cell electrical parameters, therefore a thin c-Si solar cell was used to test the scattering effect on the light-energy conversion efficiency. This cell of ~1cm^2, illustrated in Figure 3.14, is composed of a p-type monocrystalline-silicon layer, 1.1 µm-thick layer with a i/n$^+$ a-Si:H emitter at the front-side, covered with a 75 nm-thick ITO layer and Ti/Pd/Ag emitter fingers. The rear-side was covered by an Al layer as base contact and bonded to a glass substrate. Further fabrication details can be found in ref. [155].
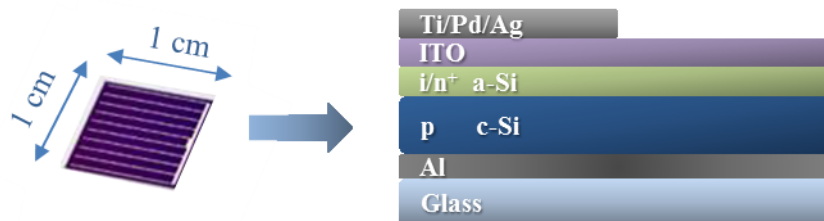
Figure 3.14: Image and schematic of c-Si solar cell.

Current density (J) versus voltage (V) measurement was carried in dark and under 150W halogen lamp condition both on the bare cell and on the cell with highest haze NR3 sample placed on top. The results are reported in Figure 3.15.
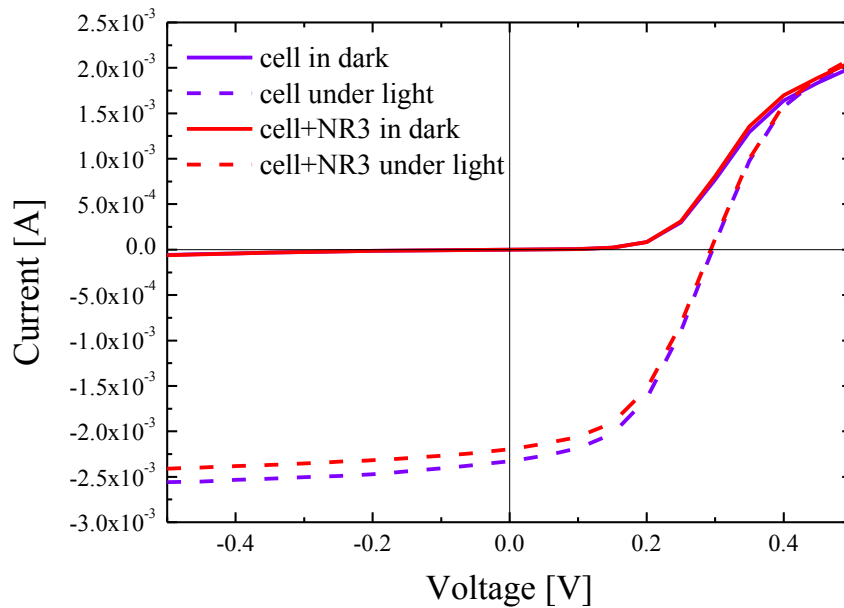
Figure 3.15: J-V curve under 150W halogen lamp for the bare cell and for the cell with NR3 sample on top.

The open circuit-voltage (V_{oc}) and the fill factor (FF), extracted from J-V curves, do not change with ZnO NRs film application and only a small decrease (~8%) of short circuit current density (J_{sc}) is observed which finds a justification by considering the lower total transmittance at wavelengths shorter than 600 nm, as shown in Figure 3.12. Such drawback, caused by the light reflection at air/glass interface and the light absorption in ZnO at energy close to its bandgap, can be reduced by a fine tuning of NR length and density and by using an antireflection coating.

External quantum efficiency (EQE) measurements have been done in short-circuit condition in the 400-1100 nm wavelength range (with a 20nm step), by dividing the net current density increment ($J_{light}–J_{dark}$) per the incident light power. NR2 and NR3 samples have been placed, as in the case of J-V measurements, in between the c-Si solar cell and the light beam, as

shown in the sketch in Figure 3.16. To measure the net effect on the light-energy conversion of the NR induced light scattering, disentangled from the above shortcoming, EQE analyses were carried out by considering the actual light intensity hitting the cell after passing the NR film, corresponding to T_{tot} reported in Figure 3.15(a).
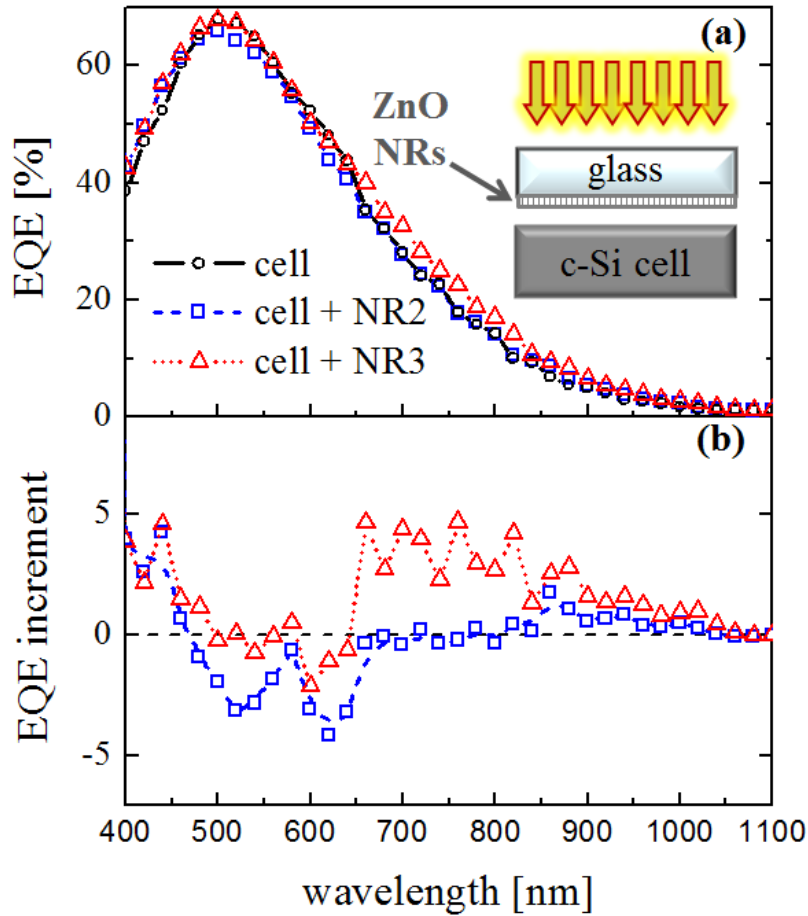
Figure 3.16: (a) External quantum efficiency (EQE) of c-Si cell and of the cell with NR2 or NR3 placed on top (see drawing). (b) EQE difference between cell with and without ZnO NR layer [149].

EQE curves of the c-Si cell with and without the ZnO NR layer are shown in Figure 3.16(a). Given the fact that the absorber layer of the cell is ∼1 μm, the scattering effect of ZnO NRs, if any, is expected only for λ larger than 600 nm (shorter wavelengths are certainly absorbed in 1 μm Si). A clear increase of the quantum efficiency is observed for NR3 at λ longer than 600 nm. This can be attributed to the longer pathways experienced in the c-Si solar cell by light deflected by the NR layer, and to the higher incident angle at the c-Si/Al interface reducing the plasmonic loss [156, 157]. To better visualize the effect, Figure 3.16(b) plots the EQE difference among the cell with or without the NRs film. A positive gain in EQE is observed at 400 nm for both samples (probably due to normalization effect of T_{tot} at λ close to the ZnO bandgap energy), while for NR2 sample, a negative EQE difference is recorded in the 450–650 nm range. In this last λ range, NR3 and NR2 samples have the same T_{tot} but NR3 has a much larger Haze. Finally, a net positive gain in EQE is observed at wavelengths longer than 600 nm, much more evident for NR3 than for NR2.

Given the EQE above reported, J_{sc} under 1 sun illumination can be estimated by using the formula [158]:

$$J_{sc} = e \int EQE(\lambda) \left(\frac{dJ_\gamma}{d\lambda}\right) d\lambda \qquad (3.4)$$

being $\left(\frac{IdJ_\gamma}{d\lambda}\right)$ the standard AM1.5G solar intensity spectrum and *e* the electron charge. In the case of NR3 sample, J_{sc} increases from 12.0 (bare cell) to 12.7 mA/cm^2. These data prove that the ZnO NR layer may effectively improve the light-energy conversion for λ longer than 600 nm. It should be also noted that Figure 3.16 evidences the ZnO NR effect on the EQE for the specific solar cell we used. Further improvement may be expected in alternative solar cell configurations. In fact, in the present cell, a significant amount of photons is lost by parasitic absorption of the Al rear layer that is directly contacted with the c-Si film [155].

3.4   Conclusions

Transparent film based on ZnO nanorods with different morphological and structural features were synthesized on transparent glass by CBD. The light scattering effect of ZnO NRs was investigated and simulated, pointing out that a threshold in the ZnO NR length (~1 µm) exists over which the scattering efficiency is greatly enhanced. ZnO NR film was also tested on a c-Si (~1 µm thick) solar cell, physically decoupled from the ZnO NR film, proving that EQE is enhanced for λ larger than 600 nm. These results show that ZnO NRs can be applied as light scattering layer on top of a solar cell without having to modify the cell fabrication process.

Although the present study has been mainly focused on silicon based thin film technology, the achieved results, in terms of control of the nanostructures morphology and of the corresponding optical properties, can be successfully used to improve the efficiency in many kinds of zinc oxides based solar cells as polymer, hybrid and dye sensitized photovoltaic devices.

Finally, decoupling the ZnO film from the solar cell, greatly increases the versatility of such light diffuser layer, making them suitable also for photovoltaic device in *substrate configuration*, suited for deposition on flexible.

Chapter 4

ZnO Nanowalls by Chemical Bath Deposition: Growth and Applications

ZnO nanowalls are a new form of nanostructure with high surface-to volume ratio and reactivity, key elements for enhancing the material-environment interactions. Indeed, ZnO NWLs are extremely active in sensing and photocatalytic applications. As an additional advantage, ZnO NWLs can be synthesized via low temperature chemical bath deposition on Al-covered substrate. A clear understanding of the main factors driving the growth mechanism of ZnO NWLs is lacking, hindering a good control of the synthesis. In this regard, the scientific efforts that have been made so far are limited and many aspects remain to be investigated.

In this chapter the effects of the solution composition, pH, concentration of Al(OH)$_4^-$ and growth time on the quality of ZnO NWL films are examined. A prior oxidation of Al substrate is proposed as a new, easy and inexpensive route for enhancing the quality of ZnO NWLs. A self-screening model has been developed to explain the growth kinetics of ZnO NWLs. The promising results of ZnO NWLs as pH sensing material and as photocatalyst are shown in the last sections.

4.1   ZnO Nanowalls growth: role of pH

Ye et al. [110] reported the possibility to tune the thickness and the growth rate of ZnO NWL films by regulating the pH of the solution in chemical bath deposition. As discussed in the Section 1.5, the role of $Al(OH)_4^-$ ions in determining the morphology of NWLs is generally accepted.

We studied the effect of solution composition and pH on the growth of NWLs by varying the reagents composing the chemical bath. All the ZnO NWL films presented were synthesized under chemical bath deposition conditions, illustrated in Figure 4.1, using a solution of DI water (18.2 MΩ·cm) with 25 mM zinc nitrate hexahydrate and HMTA and, in some cases, 16 mM ammonium hydroxide (AH). Except if otherwise indicated, the growth was performed at 95 °C for 300 s on Al film (100 nm thick, sputtered on silica over silicon substrates). For some test the Al film was previously electro-anodized . For all samples, the bare Al films were sonicated in soapy water, water, ethanol, and acetone before use. The NWL film quality is defined in terms of homogeneity in film thickness across the substrate and the presence or absence of embedded ZnO (micro/nano) particles.
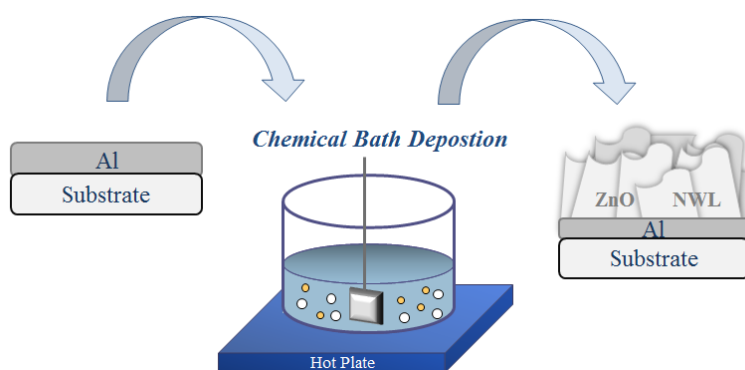
Figure 4.1: Simplified scheme of the synthesis of ZnO NWLs by CBD.

Three kind of samples of ZnO NWLs were prepared using zinc nitrate with HMTA (sample named ZNW1), zinc nitrate with AH (ZNW2) or   zinc

nitrate with the combination of HMTA and AH (ZNW3), as summarized in Table 4.1. When only HMTA was used, measured pH was 5.7, while the addition of AH -with or without HMTA- increased the pH to 7.4.

| Sample	Solution Content	Solution pH	Thickness [nm]
ZNW1	Zinc Nitrate + HMTA	5.7	850
ZNW2	Zinc Nitrate + AH	7.4	600
ZNW3	Zinc Nitrate + HMTA+AH	7.4	1200

Table 4.1: Synthesis condition of ZnO NWL samples and related film thicknesses. Adapted from ref. [159].

Figure 4.2 reports the SEM plan views of the three samples. ZNW1 presents the lowest density of ZnO NWLs compared with the other samples, while both ZNW2 and ZNW3 have a more interlaced structure. This can be attributed to an increased nucleation of NWLs as a result of a higher concentration of $Al(OH)_4^-$ at high pH. It should be stressed that the SEM micrograph in Figure 4.2(b) reports the best NWL density for ZNW2, that showed quite significant variation in the density of NWLs across a wide area of the substrate. Uniformity in the density of the NWLs improves significantly in ZNW3. However, the increase of the pH was accompanied by an unwanted side effect. Both ZNW2 and ZNW3 samples presented a significant number of micro and nano-particles embedded in the film. This presence of embedded particles is likely due to a fast precipitation of ZnO in solution at higher pH. We also observed that, in the case of the synthesis with only zinc nitrate and AH, further increase in AH concentration to 32 mM gave the same film thickness as ZNW2 but with even worse quality. As shown in Table 4.1, the thicknesses of NWL films are 850, 600, and 1200 nm for ZNW1, ZNW2, and ZNW3, respectively. This indicates that increasing pH, as a way of increasing the concentration of $Al(OH)_4^-$, does not necessarily lead to increase in film thickness. The combination of HMTA and higher pH (ZNW3) gives a faster growth, implying that this combination is essential for both higher nucleation and growth rates of NWLs.
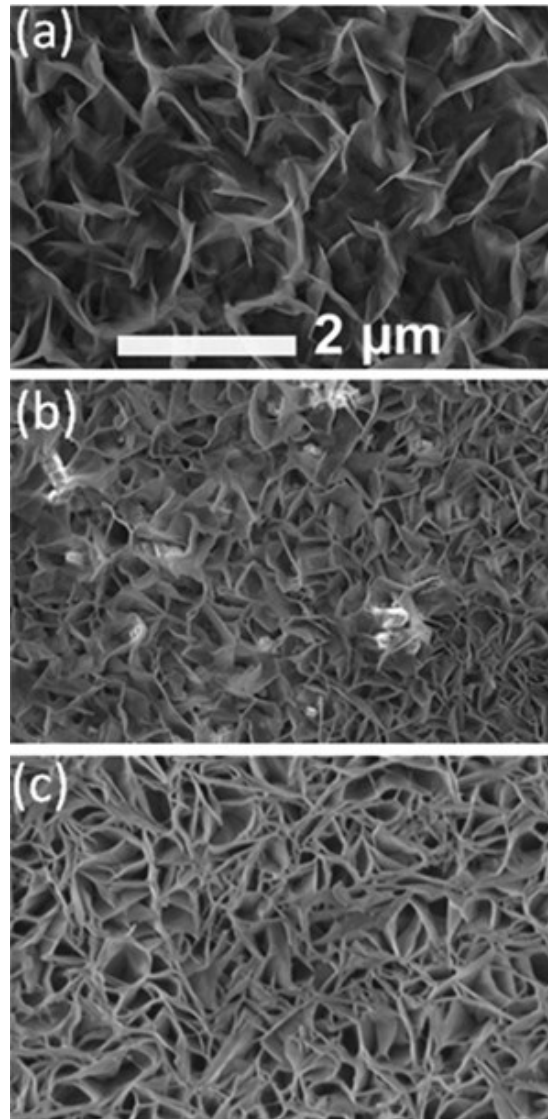
Figure 4.2: Plan view SEM micrographs of ZnO NWL films: (a) ZNW1, (b) ZNW2, (c) ZNW3. Scale bar is the same for all the images [159].

To investigate the composition of as grown material and to define the thickness of the possible residual aluminum after the growth of ZnO NWLs, we carried out RBS analyses on ZNW1 and ZNW2 samples and Al film used as substrate. The thickness of ZNW3 hindered the acquisition of a reliable RBS spectrum. The peaks at 1.6, 1.1 and 0.75 MeV, reported in Figure 4.3, are related to He$^+$ ions backscattered by Zn, Al, and O atoms, respectively. The Al film shows a sharp peak at 1.1 MeV while the O signal at 0.71 MeV comes from the silica below. ZNW1 and ZNW2 have a similar Zn peak at 1.6 MeV but only ZNW1 shows a strong Al peak at 1.05 MeV (shifted to lower energy because of the NWL film on top). Only a very small signal at 1.05 MeV is observed for ZNW2. This suggests a fast corrosion of the Al film during ZNW2 growth at higher pH and it may be responsible for the smaller thickness and poor quality of its ZnO NWL film, as this fast corrosion might have delayed or impeded the heterogeneous NWL nucleation. The reason this deleterious effect was not seen in ZNW3 (prepared at the same pH) can be related to the presence of HMTA. One possible explanation is that HMTA helped in keeping under control the Zn^{2+} concentration by reducing the spontaneous precipitation of ZnO in the chemical bath (for example, through chelating free Zn^{2+} ions [Pachauri]). This then would enhance NWL nucleation and growth. It is also possible that steric hindrance caused by interaction of HMTA with alumina (Al^{3+}) inhibited its fast dissolution. The area of Zn peak (A$_{Zn}$) is proportional to the dose of Zn in the NWL film, which is 0.82×10^{17} and 1.05×10^{17} Zn at./cm^2 in ZNW1 and ZNW2, respectively. In both cases, the O signal is in agreement with a Zn:O ratio of 1:1. ZNW2 contains a larger amount of ZnO compared to ZNW1, according to the more dense structure. On the basis of these data and growth time (300 s), we also estimated the deposition rate of ZnO molecules in this NWL structures, which results about 3×10^{14} ZnO molecules/(cm^2 × s). It is worth noting that ZnO NRs, grown with the same synthetic condition as ZNW1, showed a vertical growth rate of 12 nm/min, as reported in Chapter 2, which translates to around 4×10^{14} ZnO molecules/(cm^2 × s). This demonstrates that the precipitation kinetics of ZnO molecules is not greatly affected by the presence of Al(OH)$_4^-$, whose main function is shaping the solid ZnO.
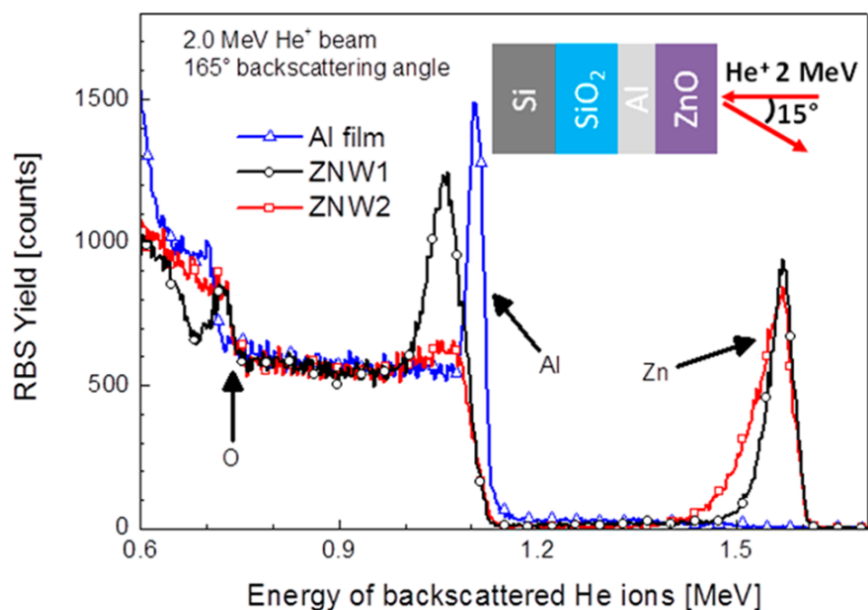
Figure 4.3: RBS spectra of ZNW1, ZNW2, and Al film. The inset shows the experimental setup and the sample structure (ZnO NWL film on Al/silica/silicon) [159].

To evaluate the porosity in these two samples, the filling factor (FF, fraction of volume occupied by ZnO) was calculated. An equivalent thickness (t_{eq}) was derived from the RBS spectra, as $t_{eq} = (A_{Zn}/\rho_{Zn})$, where ρ_{Zn} (2.05×10^{22} Zn at./cm^3) is the density of Zn atoms in ZnO. FF is the ratio of t_{eq} to the measured thickness. We obtained t_{eq} and FF of 40 nm and 4.7% for ZNW1, and 51 nm and 8.5% for ZNW2. It is therefore clear that ZnO NWL film is a highly porous material, with pore size in the range of 50−200 nm.

The impact of Al(OH)$_4$ $^-$ on ZnO NWL film thickness and quality was further investigated by carrying out synthesis on substrates seeded with ZnO nanoparticles layer. A volume of 20 µL of 1 or 0.1 wt % ZnO colloid (diluted with ethanol, particle size <40 nm) was spin coated on 1 cm^2 of substrate at 7000 rpm for 30 s, followed by heating at 120 °C for 20 min. ZNW3_0.1% and ZNW3_1% samples were synthesized using the same synthetic conditions of ZNW3 on Al film spin coated with 0.1 and 1 wt % ZnO colloidal solutions, respectively. ZNW3_0.1% yielded a film thickness

(Figure 4.4(c)) and porosity (Figure 4.4(a)) similar to ZNW3- the related seed layer was too thin to be viewed by SEM in cross section but was clearly seen in plan view (not shown). In ZNW3_1% sample, the more concentrated ZnO colloidal solution gives rise to a thicker seed layer (about 70nm) and the NWL film shows a reduced thickness (4.4(d)) of 600 nm, with a lower porosity (Figure 4.4(b)) than even ZNW1. This implies that the presence of thicker seed layer, limiting the penetration of the synthetic solution and the consequent diffusion of $Al(OH)_4^-$ from the Al substrate, significantly reduces the concentration of $Al(OH)_4^-$. In any case, the Al films were not completely corroded in these samples.
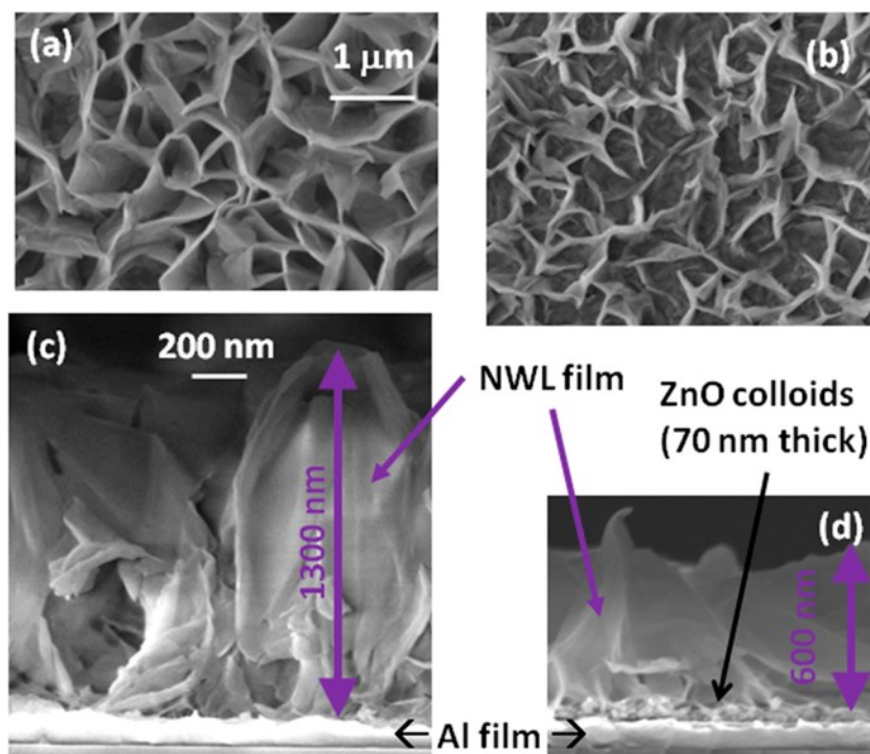

Figure 4.4: SEM images of plan (a) and cross-section (c) of ZNW3_0.1% and plan (b) and cross section (d) of ZNW3_1%. The scale bar is the same for each kind [159].

The experimental data prove that the production rate of $Al(OH)_4^-$ ions largely affects the thickness and porosity of NWL film and thicker film can be obtained with a higher concentration of $Al(OH)_4^-$, achieved by increasing pH. However, the latter is not suitable for Al or some pH sensitive substrates, whose fast corrosion in a highly basic solution damages the quality of NWLs grown on them. Therefore it is worthwhile developing a different approach for enhancing the rate of generation $Al(OH)_4^-$ and the quality of the resulted ZnO NWLs film.

4.2   Pre-anodization of Al substrate

We tested a preliminary and controlled anodization of Al substrate as a way to increase its oxide layer and to enhance the rate of generation of $Al(OH)_4^-$, with the aim to avoid the detrimental effects on NWL film quality produced by high pH. The basic assumption of this approach is that dissolution of anodic aluminum oxide should be faster than that of pure Al. The particular morphology and properties of porous aluminum oxide (or *alumina*, Al_2O_3), formed by the anodization process of aluminum in presence of particular electrolytes, has attracted the scientific attention and determined the numerous applications of anodized Al in nanotechnology [160]. The geometry of anodic alumina can be represented schematically by a honeycomb structure with a closed-packet array of columnar cells, as depicted in Figure 4.5. The structure of anodic alumina is characterized by the presence of a thin oxide layer contiguous to metallic Al substrate that continually regenerates during the growth of the pore walls. Many studies have focused on investigating the role of synthetic parameters (type and concentration of electrolyte, anodic voltage, bath temperature and process time) in controlling the electrochemical growth of aluminum oxide [161, 162].
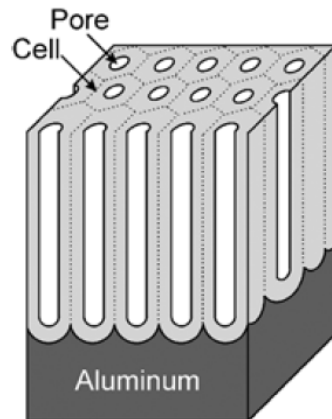
Figure 4.5: Schematic model of (a) porous anodic alumina and (b) cross-sectional view of the anodized layer. Adapted from [160].

In general, the overall reaction leading to the formation of anodic alumina is the following [163]:

$$2Al + 3H_2O \rightarrow Al_2O_3 + 3H_2 \qquad (4.1)$$

The self-organized growth of ordered pores on anodized aluminum occurs within a relatively limited range of conditions and a mild anodization can be carried out at room temperature, using sulfuric, oxalic or phosphoric acid as electrolytes [160]. For each kind of electrolyte, a particular value of anodizing potential exists, at which the optimum degree of pore ordering is reached (*self-ordering regime*). Moreover, nowadays multi-steps anodizing procedure is commonly used, instead of single-step approach, in order to enhance the periodic arrangement of the porous structure. Bwana reported on the production of anodic Al by a two-step anodizing process in 0.4 M sulphuric acid at constant cell potentials of between 5 and 25 V and at a constant current density of 20 mA cm^{-2} and demonstrated that 25 V is the self-ordering voltage for sulfuric acid. However, for the purpose of the present work it is not necessary to ensure a highly ordered porous structure, therefore the anodization of Al was carried out at lower potential (5 V),

using as reference electrode a saturated calomel electrode (SCE) and *VersaSTAT 4* potentiostat, in 0.4 M sulfuric acid for 2 min. Such conditions yielded a thin porous aluminum oxide layer. A comparison of the RBS spectra of Al film before and after this anodization process is presented in Figure 4.6. The RBS spectra were obtained in glancing detection mode to enhance the depth resolution at the surface. In this configuration, Al and O peaks are at 1.35 and 1.05 MeV respectively. Spectral simulations were performed with *SimNRA* software [164]. According to the sample structure reported in the Table 4.2, Al film contains a very thin native Al oxide layer at the surface, while the oxide layer on anodized Al is thicker and fairly stoichiometric. SEM micrographs (insets in Figure 4.6) reveal that the surface of pure Al is somehow rough, comprising big and small particles, while that of the anodized film is smoother, exhibiting the expected porous structure (pore size ≈ 10 nm).
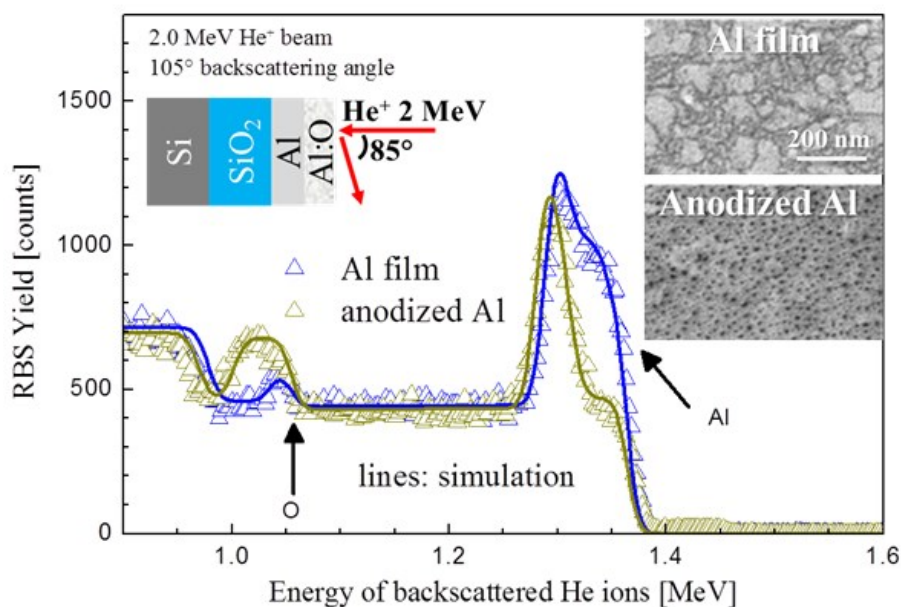

Figure 4.6: RBS spectra (symbols) of Al and anodized Al films. The insets show SEM micrographs in plan view of Al film (top) and anodized Al film (bottom). The scale bar is the same for all the images. Adapted from [159].

106

| Sample	Bottom Layer	Top Layer
Al film	38 nm – Al:O=95:5	10 nm – Al:O=70:30
Anodized Al	22 nm – Al:O=90:10	20 nm – Al:O=60:40

Table 4.2: Structures of the Al film before and after anodization, derived from the simulation (lines) of RBS spectra.

A ZnO NWLs sample (named ZNW1_anod) was grown on anodized aluminum under the same synthetic conditions as ZNW1 (pH=5.7). It can be seen from Figure 4.7(a) that ZNW1_anod film is quite uniformly thick across a wide area of the substrate, unlike ZNW1 which shows a variation in film thickness, Figure 4.7(b). Since this lack of uniformity was also seen in ZNW3, it is possible conclude that it does not depend on the concentration of the aluminum complex but it can be related to the surface roughness of the non-anodized Al film, indicating a morphology-dependent rate of $Al(OH)_4^-$ across the substrate surface. Anodization therefore helps to smoothen the surface of the substrate, ensuring a uniform rate of the complex generation. It should be noted that the dark spots in Figure 4.7(b) are not necessarily void of NWLs, though they may be less populated. The insets of Figure 4.7 indicate that the thickness of ZNW1_anod is 1300 nm, compared to 850 nm for ZNW1, representing an increase of 53%. This is similar to the difference between ZNW1 and ZNW3, implying that the concentration of $Al(OH)_4^-$ can be increased at a lower pH value when Al is replaced with anodic aluminum oxide. Therefore, ZNW1_anod possesses a larger surface area than ZNW1. Moreover, there is little or no evidence of embedded particles n ZNW1_anod.
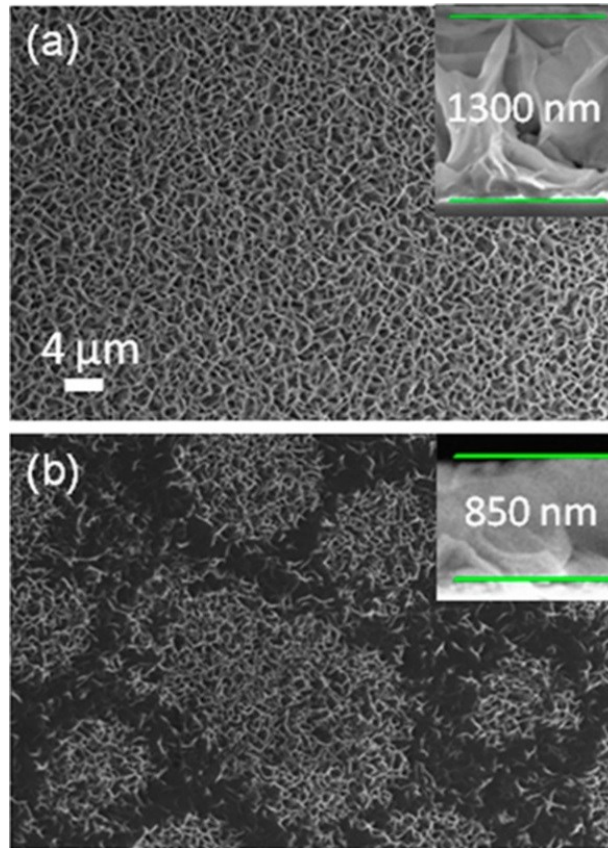
Figure 4.7: Low magnification SEM plan image of (a) ZNW1_anod, and (b) ZNW1. The insets are their cross sectional views. Scale bar in (a) is the same for (b). Adapted from [159].

Room temperature photoluminescence spectra related to ZNW1, ZNW1_anod and ZNW3 samples are reported in Figure 4.8. In all the cases a peak centered at 560 nm was observed, attributed to radiative recombination from band gap defect states. This indicates that increasing the concentration of $Al(OH)_4^-$ does not affect the energy level of the surface defects.
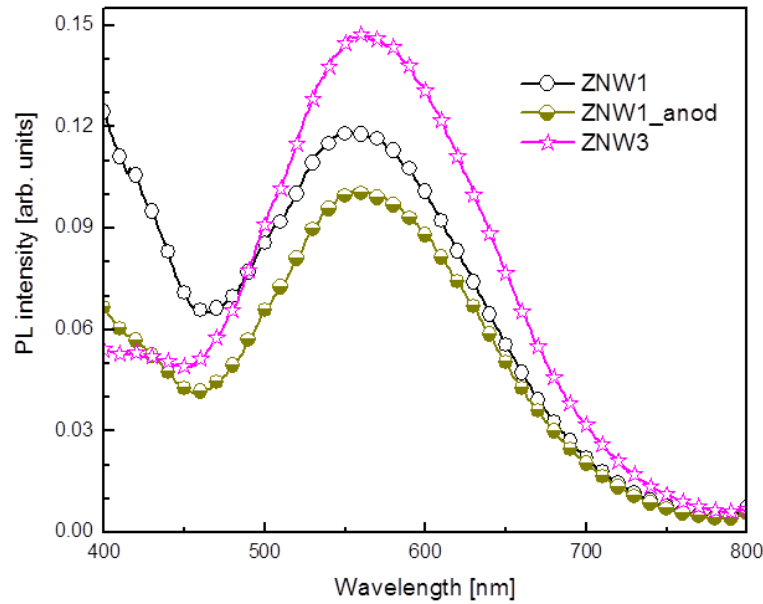
Figure 4.8: Photoluminescence spectra of ZNW1, ZNW1_anod and ZNW3 grown at 95°C.

4.3   Growth Kinetics and Model

With the aim to gain insight into the growth kinetics of the ZnO NWLs, various samples were grown on anodized Al for different duration. It can be seen from Figure 4.9 (a−e) that after 10 s of growth the substrate is only sparsely covered by NWLs, with the coverage increasing after 30 s. At 90 s the substrate becomes uniformly and densely covered, which was also evident by visual observation. Little or no change in porosity occurs from 90 to 300 s. The sample grown for 900 s appears smoother than those grown for 90 and 300 s. As shown in Figure 4.9(f), there is an explosive growth within 90 s, with the film thickness reaching 800 nm, while the growth rate decreases at higher duration.
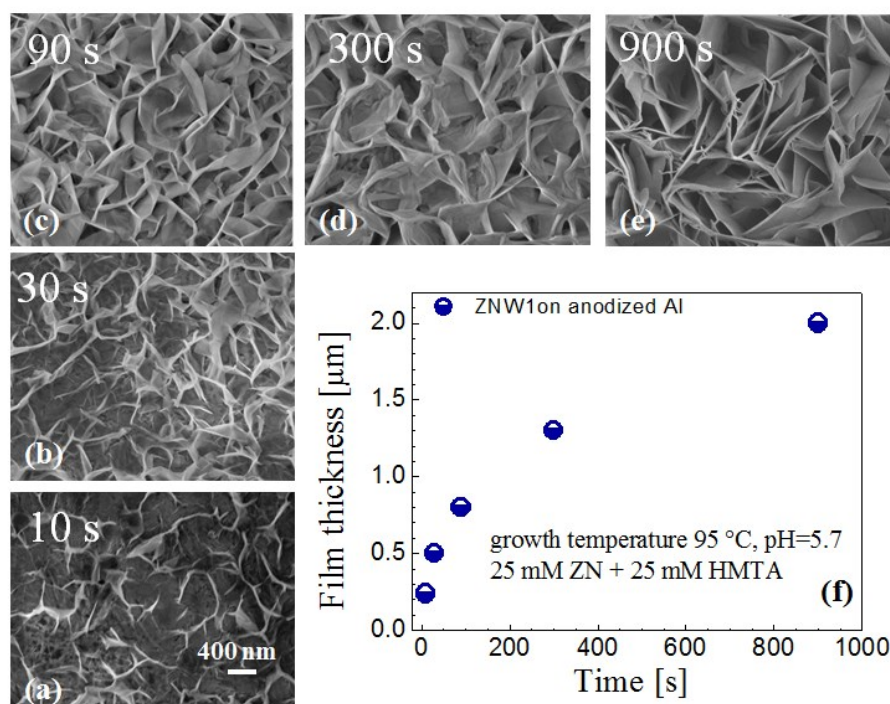
Figure 4.9: SEM plan views of ZNW1_anod grown for (a) 10 s, (b) 30 s, (c) 90 s, (d) 300 s, and (e) 900 s; the scale bar is the same for all. (f) NWL film thickness vs growth time for ZNW1_anod. Adapted from [159].

The presence of the ZnO crystal structure was confirmed with high resolution X-ray diffraction analyses of NWLs grown on non-anodized Al, for 60 min at 90 °C [165]. In that case the X-ray diffraction pattern revealed a peculiar splitting of the (002) peak into two components (corresponding to d-spacing of 0.261 and 0.265nm) indicating the occurrence of a non-uniform strain on the zincite planes. X-ray diffraction patterns were acquired also for ZNW1 and ZNW1_anod grown at 300 and 900 s, confirming the presence of the ZnO crystalline structure, with clear signal of the expected reflections (100, 002, 101) for the 900 s samples (Figure 4.10). Also in this case, the (002) peak results split in two components at lower diffraction angles. The films grown for a longer time exhibit more intense peaks, probably due to

enhanced film thickness or to progressive crystallization while the peaks for the samples grown for 300 s are weak and quite hard to be detected.
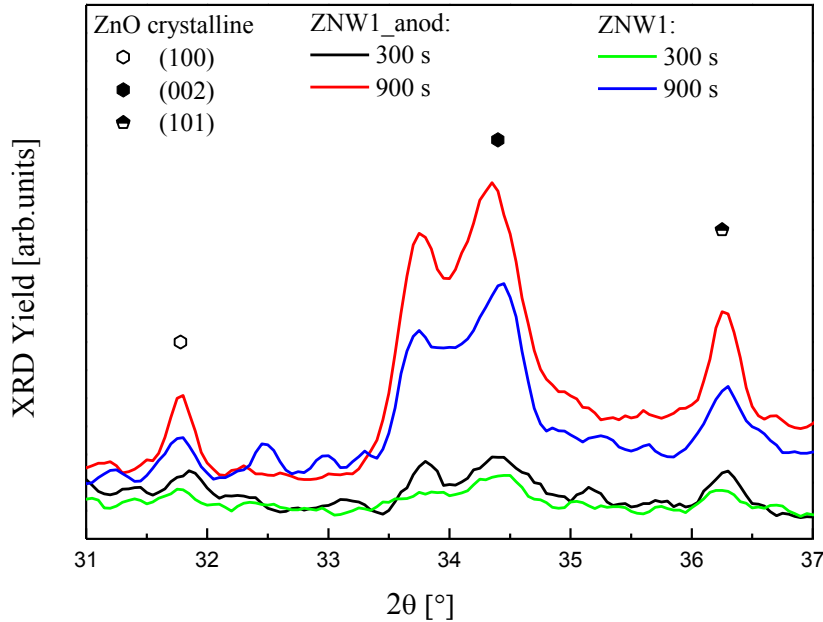
Figure 4.10: XRD spectra of ZNW1 and ZNW1_anod grown at 95°C, for 300 and 900 s.

The growth trend of ZnO NWs suggests a kinetics process highly affected by the concentration of $Al(OH)_4^-$. Indeed, taking into account also the results of the synthesis on the substrate seeded with ZnO colloids (Figure 4.4), it can be assumed that initially, a maximum flux of the $Al(OH)_4^-$ complex is attained just over the surface of the substrate, ensuring a growth rate as high as 15−20 nm/s at the early stage. With increasing NWL film thickness, the flux of $Al(OH)_4^-$ coming from the substrate decreases, because the growing NWLs screen the Al film from the solution and, in addition, can obstruct the diffusion of Al complex to the top of the film. A simplified scheme of this process is shown in Figure 4.11. In solution, the diffusion of the Al complex can be very fast compared with its generation, thus we assume that the flux of $Al(OH)_4^-$ complex is essentially limited by its generation.
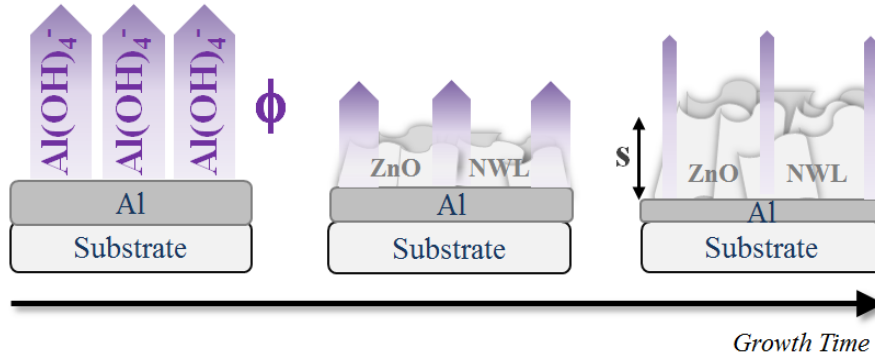
Figure 4.11: Scheme representing the evolution of the flux (ϕ) of the Al(OH)$_4^-$ complex coming from the Al substrate.

The following two hypotheses are the basis for a self-screening model developed to explain the growth kinetics:

(i) the flux (ϕ) of Al(OH)$_4^-$ generated at the surface of the substrate decreases exponentially with film thickness (s);

(ii) the growth rate of the film is proportional to ϕ.

These bring to fore the following equations:

$$\frac{d\phi}{ds} = -a\phi \tag{4.2}$$

$$\frac{ds}{dt} = b\phi \tag{4.3}$$

Where a, b and ϕ_0(flux of Al(OH)$_4^-$ at the beginning) are the only parameters. The analytical solution for $s(t)$, given at $t = 0$ and $s = 0$, is:

$$s(t) = \alpha \times \ln(1 + \beta t) \tag{4.4}$$

Where $\alpha = \frac{1}{a}$, $\beta = ab\phi_0$.

Figure 4.12 reports the time evolution of the NWL thickness for ZNW1_anod (half-close circles) and ZNW1 (open circles) grown at 95 °C, and for ZNW1 (open squares) grown at 70 °C, giving a more complete picture of the kinetics. The error bars are as large as the sizes of the symbols.
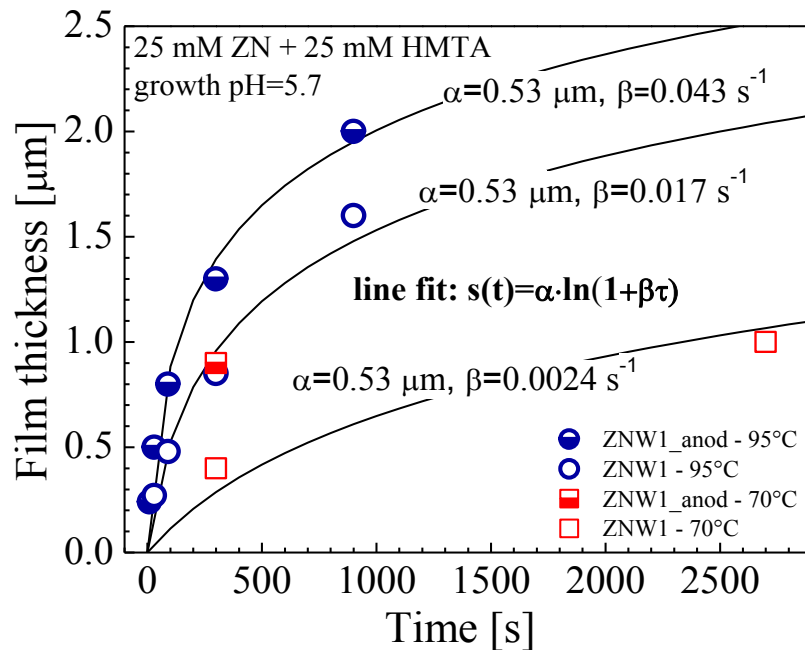
Figure 4.12: NWL film thickness versus growth time for ZNW1_anod (half-filled symbols) and ZNW1 (open symbols) grown at 95 ˚C (circles) and 70 ˚C (squares). The lines represent the model fits to the data based on the reported equation and parameters (α and β). Adapted from [159].

It is expected that NWL films grown on anodized Al show a faster growth rate. The best fit procedure applied on ZNW1_anod at 95 °C gives the following values: $\alpha = 0.53$ µm and $\beta = 0.043$ s^{-1}. The first parameter accounts for the self-screening effect, while the second one contains the initial flux of the Al complex (ϕ_0) and the product $a \times b$. Assuming that the self-screening parameter (a) is not affected by the Al film anodization, ZNW1 grown at 95°C was fitted by fixing $\alpha = 0.53$ µm and obtaining $\beta = 0.017$ s^{-1}. This indicates that anodization increased the initial flux of Al

complex, as expected. To fit the data of ZNW1 at 70 °C, $\alpha = 0.53$ µm is considered fixed and a best fit is obtained with $\beta = 0.0024$ s−1. This is expected given the lower synthesis temperature.

Finally, the film thickness of ZNW1_anod at 70 °C (300 s growth time, half-closed square) is as high as that of ZNW1 grown at 95 °C for the same duration (Figure 4.12). In addition, the former possesses a good quality-uniformity in NWL thickness and absence of embedded particle, as shown in Figure 4.13. These evidences suggested that by preliminary anodization of Al, the temperature growth for ZnO NWLs can be decreased to 70 °C with no negative effect on NWL film quality, reaching a considerable gain in the thermal budget used.
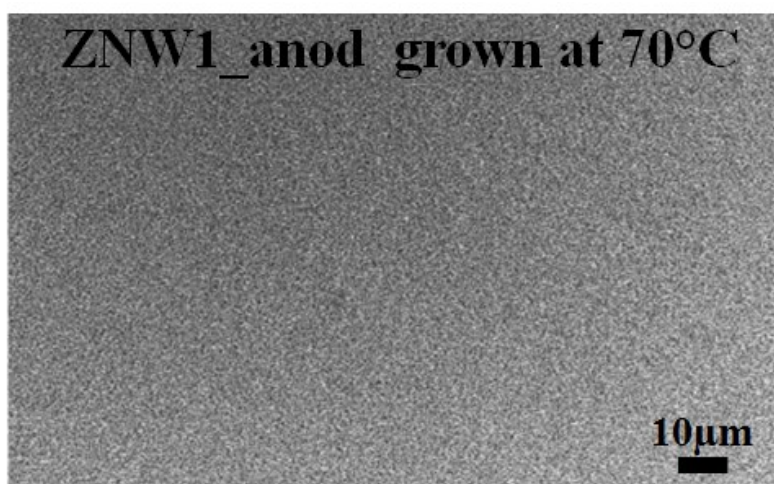
Figure 4.13: Low magnification SEM plan image of ZNW1_anod grown at 70°C.

4.4   ZnO Nanowalls as pH sensitive material

The precise monitoring of the pH of a solution represents a fundamental tool in laboratories, clinics and industries as many biological and chemical processes are pH dependent. Although the usual glass bulb pH electrode has a proven efficiency in pH measurements, the need of

miniaturized and biocompatible pH sensing has driven the exploration of new materials.

ZnO NWLs grown by CBD were proved to be an excellent nanomaterial for a fully flexible pH sensor. This kind of device highlighted some of the most intriguing properties of NWLs. First, the huge effective surface area leads enhanced sensitivity, improved signal-to noise ratio and faster response times [166, 167]. Moreover, a selective coating of Al easily enables the synthesis of patterned ZnO NWLs, essential for optimizing the device design. NWLs have also a steady contact with the substrate, providing a continuous pathway for signal transport.

The pH sensing property of ZnO NWLs was tested in an extended gate thin film transistor (EGTFT) based on low-temperature polycrystalline silicon (LTPS) on polymide (PI) substrate. Details of the fabrication of LTPS EGTFT can be found in ref [165]. ZnO NWLs were deposited on top of the sensing area of the extended Al-gate by following the same synthetic conditions of the sample ZNW1 (see table 4.1).
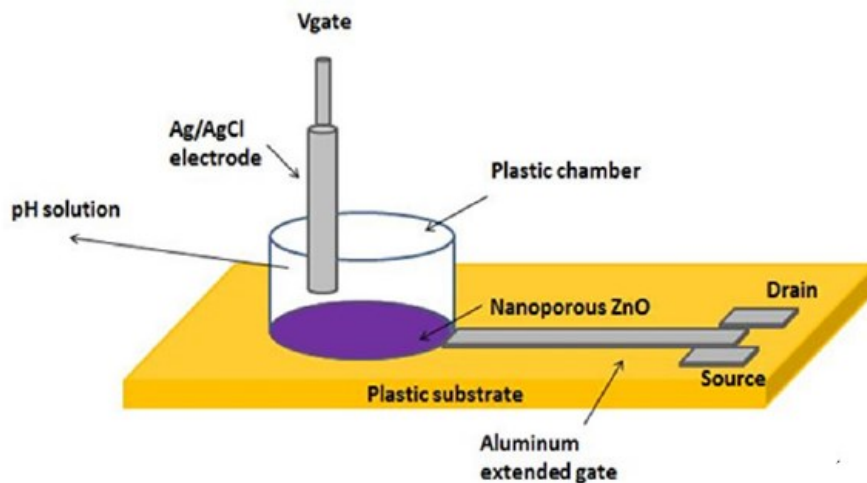
Figure 4.14: 1. Schematic of the flexible pH sensor, based on EGTFT and ZnO NWLs, and the measurement setup. Adapted from ref. [165].

The fabricated LTPS TFT is characterized by a leakage current below 10 pA, $I_{on}/I_{off} > 10^6$, a threshold voltage V_t of 7V, field effect mobility 50 cm^2/V·s, and subthreshold slope 0.9 V/dec. The pH-sensitivity was tested by exposing the extended gate to solutions having pH values ranging from 1 to 9, and using an Ag/AgCl electrode as reference, as reported in Figure 4.14. The transfer characteristics of the sensor were acquired (Figure 4.15) at low drain-source voltage (V_{ds}=0.1V) for different pH-solutions and the threshold voltage shift induced by pH variation was calculated (inset in Figure 4.15), giving a slope of 59mV/pH.
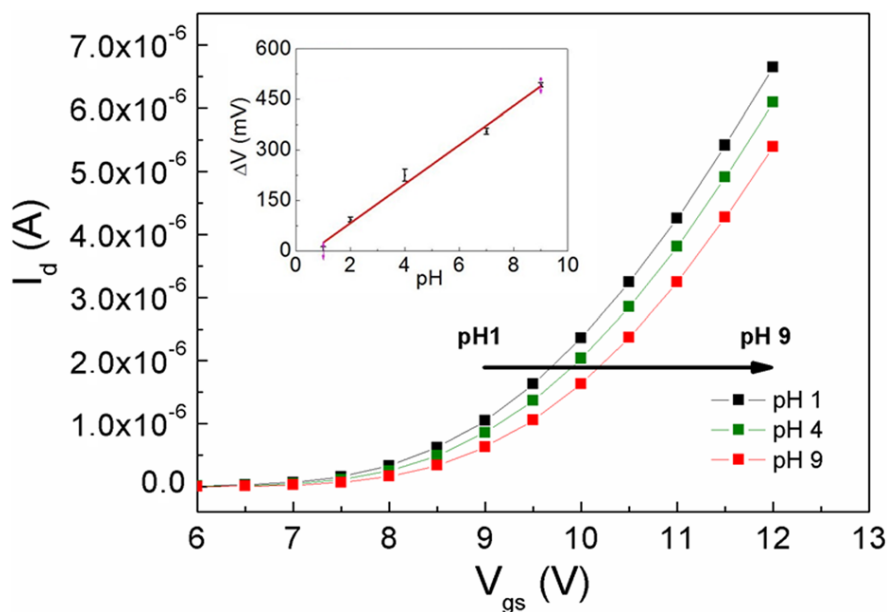
Figure 4.15: The shift in the transfer characteristic of the sensor for three increasing pH solutions up to pH 9. In the inset, a graph that shows the linear response of the sensor with a sensitivity of 59 mV/pH. Adapted from ref. [165].

Fixing the gate potential (V_g) at 9V, the output characteristics of the pH-EGTFT for different pH values were measured, Figure 4.16. The saturation current shows a consistent variation with the pH, as a result of the induced threshold voltage change.
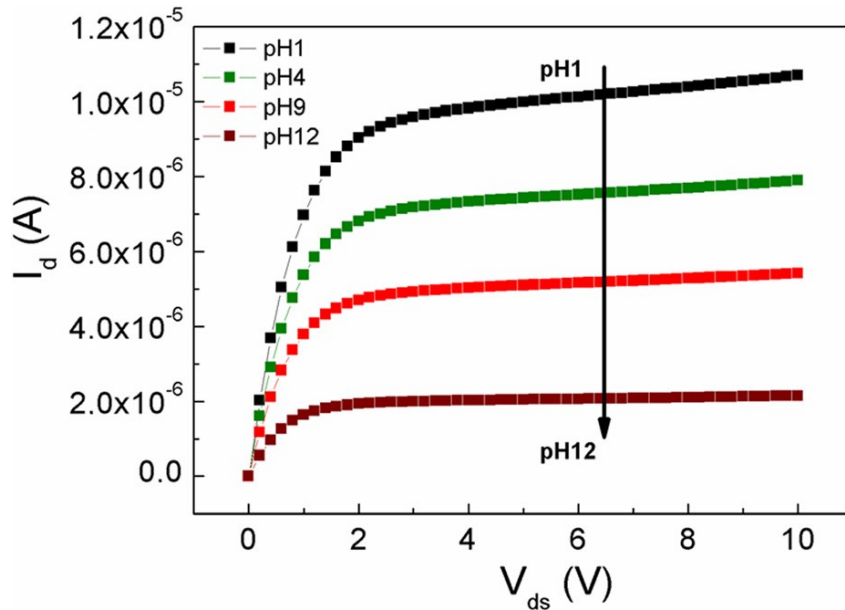
Figure 4.16: Output characteristic of the EGTFT for different pH solutions, measured at Vg=9V. Adapted from ref. [165].

As stated above, the use of the ZnO NWLs as a pH sensing material is based on the activity at the electrolyte-ZnO nanowalls interface. The H^+ specific bonding sites located at ZnO surface can protonate or deprotonate, leading to a surface charge and a surface potential that is dependent on the pH of the electrolyte solution [166, 168]. ZnO is an amphoteric compound and the hydroxyl groups present on the surface can act as proton donors or acceptors, depending on the electrolyte pH. The corresponding reactions are [169]:

$$ZnO_{(S)} + 2H_2O \leftrightarrow Zn(OH)^-_{3(S)} + H^+ \text{ (in basic solution)} \tag{4.6}$$

$$ZnO_{(S)} + H^+ \leftrightarrow ZnOH^+_{(S)} \text{ (in acidic solution)} \tag{4.7}$$
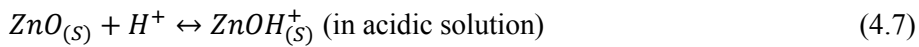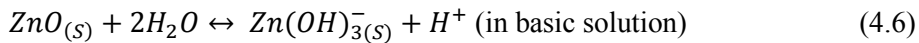
The ZnO NWLs surface potential (E_l) can be calculated according to the Nerst equation:

117

$$E_I = E_0 - 2.303RT/F\ pH \hspace{4cm} (4.8)$$

Where E_0 is the standard potential of ZnO electrode, R is the gas constant (8.314 J/mol·K), T is the absolute temperature (298K) and F is the Faraday constant (96487.34 C mol^{-1}). At room temperature and at different pH conditions, the values of E_I give a slope of 59.1 mV/pH. It is possible conclude that our ZnO NWLs based pH sensor has a sensitivity close to the ideal Nerstian response and represents a further improvement compared to the performance of ZnO nanostructures based devices reported in literature ((~28mV/pH for NRs and ~45 mV/pH for NTs) [166, 169-171].

The enhanced pH sensitivity observed for NWLs can be ascribed to very large surface-to-volume ratio and also to the presence of surface defects acting as effective bonding sites for protonation/deprotonation reactions.

4.5   Photocatalytic Performance of ZnO NWLs Films

Photocatalysis mechanism has been extensively studied in the last 40 years [172] as promising method to face the increasing water pollution. Semiconductors with appropriate wide band gap are used as effective photocatalysts able to accelerate the photo-induced degradation of organic contaminants. Figure 4.17 shows the schematic of the photocatalysis. When a photocatalytic semiconductor absorbs a photon having energy greater than the band gap energy, a valence band electron (e$^-$) is excited to the conduction band while a positive hole (h$^+$) is generated in the valence band. If the semiconductor material is in contact with the water, the positive hole could oxidize organic contaminants directly or produce very reactive hydroxyl radicals (OH•), primary oxidants in the photocatalytic system. The photo-generated electron reacts with O_2 forming highly reactive oxygen radicals. Manly of these photochemical reaction take place on the surface of the catalyst, therefore nanostructures, with their high surface-to-volume ratio, offer enhanced photocatalytic efficiency compared to bulk material.
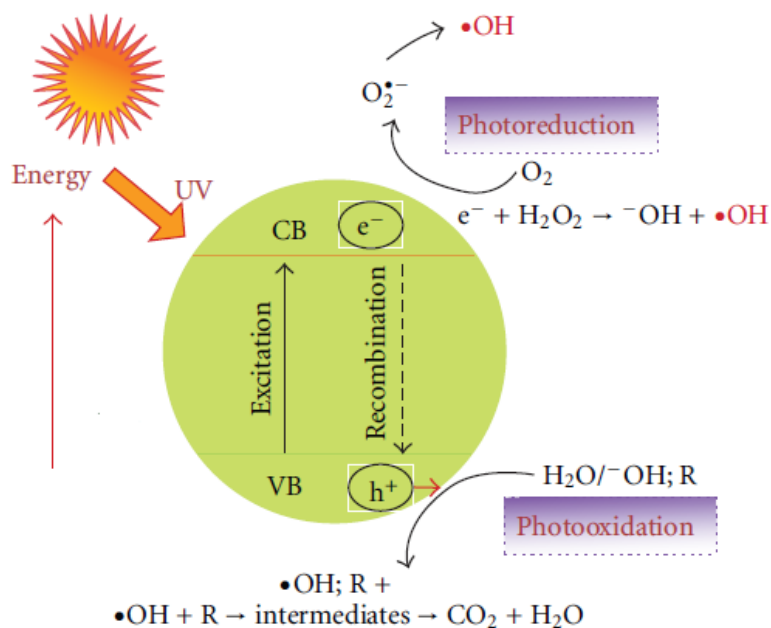
Figure 4.17: Schematic of the photocatalysis process. Adapted from ref [69].

Different ZnO nanostructures used as photocatalysts have been reported by many research groups [ref]. Ye et al. first investigated the photocatalytic decomposition of organic dye through ZnO NWLs films. They argued that the combination of large surface area and very small thickness of ZnO foils- close to the quantum size effect regime – can have favorable effect in photocatalytic efficiency. Figure 4.18(b) reports the data related to the decomposition kinetics of methyl orange (MO) in presence of ZnO NWLs film (Figure 4.18(a)) measured by Ye et al. They found that the rate constants of the degradation reactions for MO is $(1.5 \pm 0.2) \times 10^{-3} s^{-1}$, measured in presence of 2 mg of ZnO in form of NWLs dispersed in DI water.
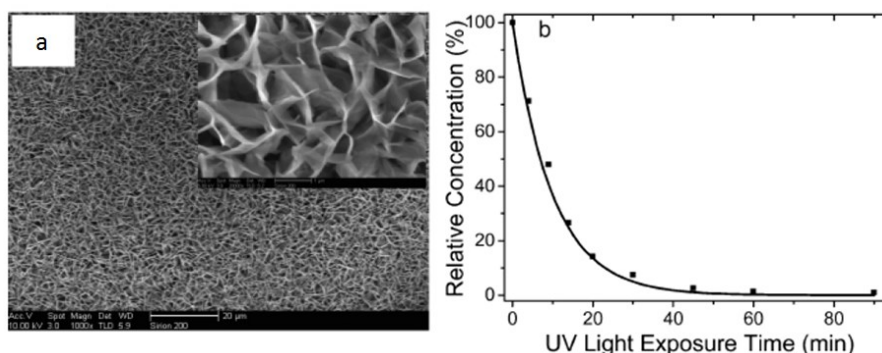
Figure 4.18: (a) SEM image of ZnO nanowall grown by CBD. (b) Apparent photodegradation of methyl orange in presence of ZnO NWLs film reported in (a). The solid squares are the experimental data, the solid lines is fitting curve using the formula $Y(t) = Y(0) \exp(-kt)$, where $Y(t)$ is the relative concentration of the organic dyes in the solution at time t, $Y(0)$ is the initial relative concentration, namely, 100%, and k is the photodegradation rate constant. Adapted from ref.[110].

As discussed in the previous sections, the nanowalls on anodized Al substrate have shown enhanced quality compared to those grown on pure Al. A better morphology could imply a more effective photocatalytic activity, therefore we conducted a comparative study to evaluated the efficiency of ZnO nanowalls grown with and without pre-anodization step, by measuring the degradation of a methyl orange solution under UV radiation. The first step was keeping ZnO NWL samples under a UV light source (8 W power; at 365 nm, 20 nm of full width at half maximum, irradiance of 1.1 mW cm^{-2}) for 60 minutes in order to remove any organic compound on the sample surface. Then the samples were immersed in an aqueous MO solution (2 mL, starting MO concentration of 1.0×10^{-5} M). To distinguish the adsorption of MO on ZnO from its own degradation, the samples were left immersed in the solution under dark conditions for 20 h, until the MO concentration remained constant (about 50% of the starting value). Thereafter, the samples were irradiated with the UV light, at regular time intervals, the absorbance of the solution was measured in the range from 350 to 650 nm using a PerkinElmer Lambda 35 UV/vis spectrometer. The degradation of MO was evaluated by the absorbance peak at 464 nm, based on the Lambert−Beer law that defines the proportionality between the <u>absorbance</u> of the radiation in a homogeneous <u>isotropic</u> medium and the concentration of the absorbing

species [173, 174]. Moreover, the decomposition of the MO solution in the absence of any catalyst was checked as a reference. Figure 4.19(a) shows the time evolution of the residual concentration (C) of MO, normalized to the initial concentration (C_0) obtained after adsorption test in the dark. The results clearly indicate that both the sample ZNW1 and ZNW1_anod act as effective photocatalysts. Furthermore, ZNW1_anod sample results to have a higher photoactivity than ZNW1. On the other hand, no response was obtained for Al film and anodized Al film. According to the Langmuir−Hinshelwood model [175], the photodegradation reaction rate (k) of water contaminants can be estimated by the following equation:

$$ln\frac{c}{c_0} = -kt \qquad\qquad (4.5)$$

where t is the irradiation time. Therefore, fitting the experimental data, it is possible to calculate the MO photodegradation rate. The rates for ZNW1_anod and ZNW1 are 3.2×10^{-6} and 2.3×10^{-6} s^{-1}, respectively.

Given the sample area and the RBS estimation of A_{Zn}, the mass of ZnO was calculated resulting about 17 μg for ZNW. If normalized to this value, the photocatalytic activity of ZNW1 becomes 0.13 (s^{-1} g^{-1}), which is in the same order of magnitude of the value reported by Ye et al. [110]. In fact, we used the less performing configuration of ZnO NWLs film on a substrate rather than ZnO NWLs scratched away from the substrate and dispersed in water. The calculated photodegradation rates for the discoloration process, normalized to the value obtained for MO decomposition without any catalyst (k_{MO}) are reported in Figure 4.19(b). ZNW1 and ZNW1_anod show a clear photodegradation activity, with the latter being 40% higher than the former. This difference can be explained by the larger surface area of ZNW1_anod. Finally, SEM analyses allowed to ascertain that the discoloration test did not change the NWLs structure, suggesting a good chemical stability of the material.
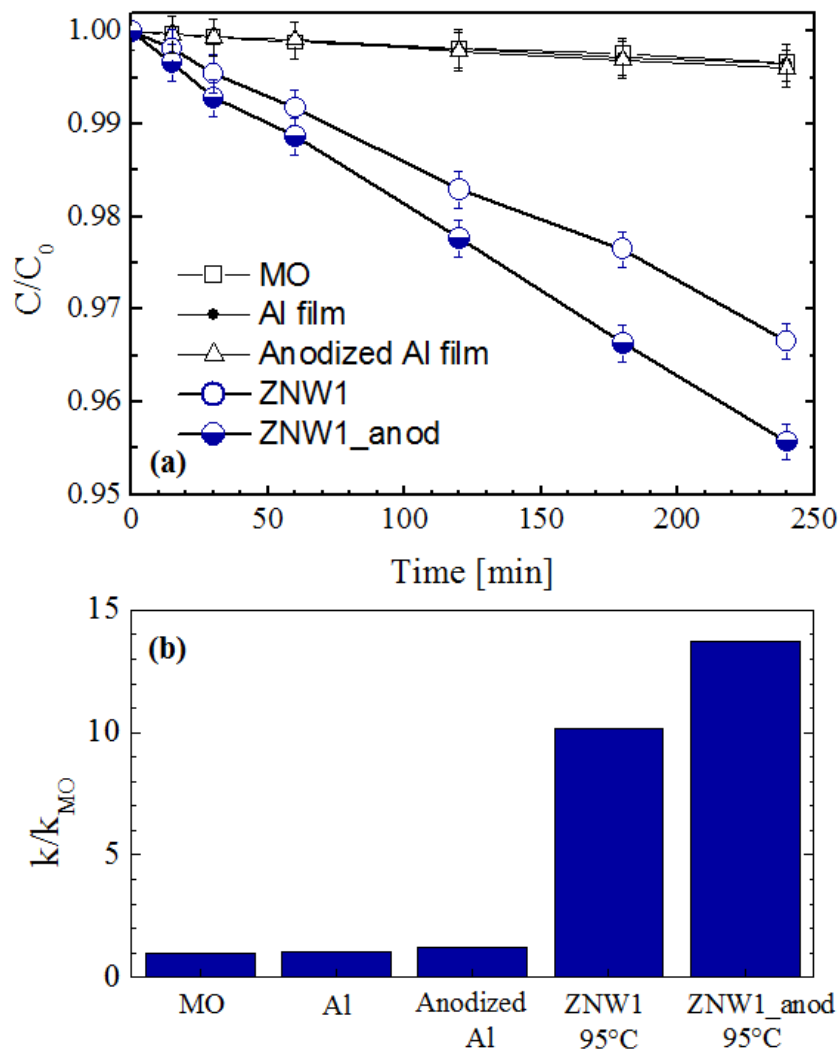
Figure 4.19: Apparent photodegradation test of methyl orange (MO). (a) Normalized MO concentration during irradiation time for ZNW1_anod (half-filled symbols) or ZNW1 (open symbols) and for reference samples (Al, anodized Al, and MO solution). (b) Photodegradation rates for the discoloration process. Adapted from ref. [159].

4.6   Conclusions

In this chapter the synthesis of ZnO nanowalls grown by CBD (70−95 °C) on Al film was studied. $Al(OH)_4^-$ ions generated in situ by the reaction of the Al substrate with the solution, are assumed to be responsible for engendering the NWL morphology. The growth rate of the film was enhanced by increasing pH from 5.7 to 7.4, which translated to increasing the concentration of $Al(OH)_4^-$. However, it was shown that this was accompanied by a poor film quality. The enhancement of growth rate and a good film quality could however be achieved at the lower pH by employing a preliminary anodization of the Al film. Anodization allowed the growth of a uniformly thick ZnO NWL film and it was also useful in increasing the film thickness without recourse to higher (basic) pH which could compromise film quality and substrate integrity. The growth kinetics was investigated and modeled, describing the dependence of ZnO NWL film thicknesses on the flux of $Al(OH)_4^-$.

A fully flexible pH sensor, based on EGTFT, was fabricated showing an ideal Nernstian response (59 mV/pH).

Finally, the potentiality of ZnO NWLs as photocatalyst was investigated. The enhanced morphology reached by the growth on anodized Al showed a higher photocatalytic activity in the degradation of toxic methyl orange, than corresponding NWLs grown on pure Al. Given these results, it would be worth exploring the possibility to use the NWLs based technology for others low-cost and marketable flexible sensing devices.

123

Summary and Perspectives

The main aim of this thesis work was achieving a good control of low-cost ZnO nanostructures. Such a goal has been obtained after a systematic study of the growth kinetics and of the structural properties of ZnO NRs and NWLs grown by chemical bath deposition in an aqueous solution containing zinc nitrate and HMTA. In fact, such low-cost products can be usefully employed in various nanoscale applications only when a robust control of the growth process is achieved.

As the synthesis of aligned NRs arrays is concerned, the precise synthetic conditions for ensuring a high degree of control and reproducibility were identified as well as the temperature and deposition time ranges suitable for growing high quality nanostructures. Under the optimized synthetic conditions, a high and constant deposition rate was achieved (around 10 nm/s). The investigation of the role of HMTA in the growth process allowed to conclude that HMTA plays a dual role in the synthesis of ZnO NRs, participating both as supplier of OH^- and as promoter of the anisotropic growth. Indeed, the preferential attachment of HMTA molecules to the non-polar faces of ZnO was found to lead to a steric hindrance effect that inhibits the lateral growth of nanorods. The two modes of action are not mutually exclusive, and the amount of HMTA resulted to be one of the key variables in the growth process. In particular, a fine-tuning of the HMTA concentration in the growth solution allows to avoid phenomena such as merging or suppression of NRs which are detrimental for device applications.

In this work the ZnO NRs have been shown to be a low-cost material able to effectively scatter the visible and near infrared radiation. We investigated the optical properties of transparent ZnO NRs (120–1300 nm long, 280–60 nm wide) layer, getting transmission haze as high as 70% at 400 nm wavelength. By varying shape and size of ZnO NRs and by using light scattering simulations we proved that a threshold exists in the NRs length (~1 μm) over which the light scattering is significantly enhanced.

ZnO NR film was also tested on a c-Si (~1 μm thick) solar cell, physically decoupled from the ZnO NR film, proving that EQE is enhanced for λ larger than 600 nm. These results showed that ZnO NRs can be applied as light scattering layer on top of a solar cell without having to modify the cell fabrication process. At any rate, decoupling the ZnO NRs film from the solar cell greatly increases the versatility of such light diffuser layer, making them suitable also for photovoltaic device in *substrate configuration*, suited for flexible technology.

Unlike the other kinds of ZnO morphologies, ZnO nanowall structure has not been investigated as much in current literature, in spite of its huge surface-to-volume ratio and extremely thin wall thicknesses. These features make the ZnO NWLs a promising future candidate for technology based on material-environment interactions. We studied the effect of the solution composition and of the solution pH on the CBD growth of NWLs upon Al film. $Al(OH)_4^-$ complexes generated in situ by the reaction of the Al substrate with the solution, are assumed to be responsible for engendering the NWL morphology. The growth rate of the film was enhanced by increasing pH of the solution which led to increase the production of $Al(OH)_4^-$ complexes. However, it was shown that the rise in the pH was accompanied by a poor film quality. We demonstrated that a combined enhancement of growth rate and a good film quality can be achieved at the lower pH by employing a preliminary anodization of the Al film. The growth kinetics of ZnO NWLs grown on both pure and anodized Al has been investigated and modeled, describing the dependence of ZnO NWL film thicknesses on the flux of $Al(OH)_4^-$.

The good control achieved in tuning the ZnO NWLs morphologies allowed to explore their potentialities in photocatalysis and sensing applications. ZnO nanowalls film was tested as sensitive membrane in a fully flexible pH sensor, based on extended gate polysilicon thin film transistor (TFT). The NWL based pH sensor showed an ideal Nernstian response (59 mV/pH), suggesting that such a technology can give actual opportunities for the fabrication of effective and marketable devices. Finally, the potentiality of ZnO NWLs as photocatalyst in the degradation of toxic

126

methyl orange was investigated, evidencing the advantage of a pre-anodization of Al substrate.

The versatility of ZnO joined with the cost-effectiveness of CBD make the nanostructures studied within this thesis promising candidates for every-day devices. Beyond the results presented, there is still significant space to improve the potentiality of ZnO nanostructures by CBD. Post-growth processing, as low-temperature thermal treatment or UV exposure, should be addressed with the aim to properly adjust the structural and physical characteristics, and to perform surface defects engineering. Preliminary electrical measurements showed that the thermal annealing in forming gas (5% H_2 in N_2) at 300°C for 30 minutes lead to a 100 times improvement in the conductivity. As a final issue of this thesis work, we recently succeeded in the synthesis of a brand new ZnO nanostructures, combining NRs and NWLs. While such a novel ZnO shape needs to be thoroughly investigated, its intriguing morphology can be useful for a variety of applications. In details, a ZnO NRs array was grown via CBD by following the procedure described in Chapter 2. Then, a thin layer of Al (~20nm thick) was sputtered on top of the nanorods. Finally, the sample was immersed in an equimolar (25mM) aqueous solution of zinc nitrate hexahydrate and HMTA for 5 minutes, to induce he NWL growth. The resulting nanostructure (ZnO NWL/NR) is shown in Figure 1.

Thin foil of ZnO rise from the top of the nanorods resulting in a structure with very large surface area, particularly suitable for sensing applications. The presence of the NRs may serve as a bridge for enhancing the signal transport between NWLs and the substrate, while exposing the bottom part of NWL to ambient. Further studies are on going on this novel nanostructure.

127
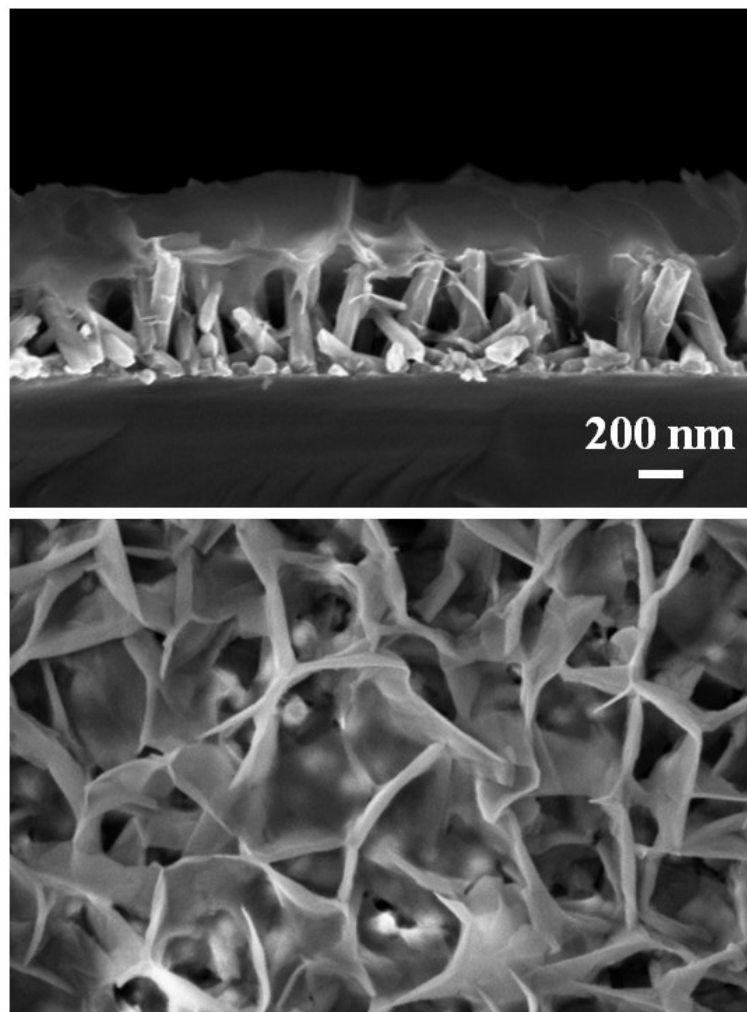
Figure 1: SEM images in cross (top panel) and plane (bottom panel) view of the ZnO NWL/NR, a novel combined nanostructures obtained by CBD with ZnO NWLs grown on top of ZnO NRs.

128

References

[1]   A. Kołodziejczak-Radzimska, T. Jesionowski, *Materials* **7**(4), 2833 (2014).

[2]   Brown H. *Zinc Oxide Rediscovered*. New York (1957).

[3]   Z. Wang, *Mat. Sci. Eng. R: Reports* **64** (3-4), 33 (2009).

[4]   C. Bunn, *Proc. Phys. Soc*. **47**(5), 835 (1935).

[5]   C. Klingshirn, *ChemPhysChem*. **8**(6), 782 (2007).

[6]   S. Nakamura and M. R. Krames, *Proc. IEEE* **101**, 2211–20 (2013).

[7]   D. C. Reynolds, D. C. Look and B. Jogai, *Solid State Commun.* **99**, 873 (1996).

[8]   A. Janotti, C. Van de Walle, *Rep. Prog. Phys*. **72**(12), 126501 (2009).

[9]   C. Klingshirn, R. Hauschild, H. Priller, M. Decker, J. Zeller, H. Kalt, *Superlattices and Microstruct.* **38** (4-6), 209 (2005).

[10]   Z. Wang, *Appl. Phys. A* **88** (1), 7 (2007).

[11]   J. Cui, *Materials Characterization* **64**, 43 (2012).

[12]   H. Morkoç, U. Özgür, *Zinc Oxide*. Weinheim: Wiley-VCH (2009).

[13]   Y. Gu, Kuskovsky I, M. Yin, S. O'Brien, G. Neumark, *Appl. Phys. Lett*. **85**(17), 3833 (2004).

[14]   S. Pearton, *Progr. Mater. Sci*. **50**(3), 293 (2005).

[15]   Z. Feng *Handbook Of Zinc Oxide And Related Materials*. Boca Raton, FL: CRC Press (2013).

[16]   C. Jagadish, S. Pearton *Zinc Oxide Bulk, Thin Films And Nanostructures*. Amsterdam: Elsevier (2006).

[17]   U. Rössler, *Phys. Rev.* **184**, 733 (1969).

[18] D.W. Langer, and C.J. Vesely, *Phys. Rev. B* **2**, 4885 (1970).

[19] C.J. Vesely, , R. L. Hengehold, and D. W. Langer, *Phys. Rev. B* **5**, 2296 (1972).

[20] D. Vogel, P. Krüger, and J. Pollmann, *Phys. Rev. B* **52**, R14316 (1995).

[21] R.T. Girard, O. Tjernberg, G. Chiaia, S. Söderholm, U.O. Karlsson, C. Wigren, H. Nyl_en, and I. Lindau, *Surf. Sci.* **373**, 409 (1997).

[22] J.E. Jaffe, J.A. Snyder, Z. Lin, and A.C. Hess, *Phys. Rev. B* **62**(3), 1660 (2000).

[23] U. Özgür, Y. Alivov, C. Liu, A. Teke, M. Reshchikov, S. Doğan, V. Avrutin, S. Cho, H. Morkoç, *J. Appl. Phys*. **98**, 041301 (2005).

[24] D. M. Bagnall, Y. F.Chen, Z. Zhu, T. Yao, S. Koyama, M. Y. Shen and T. Goto *Appl. Phys. Lett.* **70,** 2230 (1997).

[25] L. Wang and N. C. Giles, *J. Appl. Phys*. **94**, 973 (2003).

[26] Z. K. Tang, M. Kawasaki, A. Ohtomo, H. Koinuma, and Y. Segawa, *J. Cryst. Growth* **287**, 169 (2006).

[27] Y. M. Lu, X. P. Li, P. J. Cao, S. C. Su, F. Jia, S. Han, W. J. Liu, D. L. Zhu, and X. C. Ma, *Journal of Spectroscopy* **2013**, 1-7 (2013).

[28] N. Ohashi, T. Ishigaki, N. Okada, T. Sekiguchi, I. Sakaguchi, and H. Haneda, *Appl. Phys. Lett.* **80** (16), 2869 (2002).

[29] Q. X. Zhao, M. Willander, R. E. Morjan, Q-H. Hu, and E. E. B. Campbell, *Appl. Phys. Lett.* **83** (1), 165 (2003).

[30] M. Willander, P. Klason, L. Yang, S. Al-Hilli, Q. Zhao, O. Nur, *Phys. Stat. Sol.(c)*.**5** (9),3076 (2008).

[31] I. Shalish, H. Temkin, V. Narayanamurti, *Phys. Rev. B* **69**, 245401 (2004).

[32] A. Djurišić, Y. Leung, *Small* **2**(8-9), 944 (2006).

130

[33] W. Göpel, U. Lampe, *Phys. Rev. B* **22**, 6447 (1980).

[34] K. Hagemark, *J. Solid State Chem*. **16**(3-4), 293 (1976).

[35] A. Hutson, *Phys Rev*. **108**(2), 222 (1957).

[36] C. Van de Walle, *Physica B: Condens. Matter*. **308-310**, 899 (2001).

[37] A. Kushwaha and M. Aslam, *J. Appl. Phys*. **112**, 054316 (2012).

[38] M. Willander, O. Nur, J. R. Sadaf, M. I. Qadir, S. Zaman, A. Zainelabdin, N. Bano and I. Hussain, *Materials* **3**, 2643 (2010).

[39] A. F. Kohan, G. Ceder, D. Morgan, and C.G. Van de Walle, *Phys. Rev. B* **61**(22), 15019 (2000).

[40] A. Janotti and C. G. Van de Walle, *Phys. Rev. B* **6**, 44 (2007).

[41] C.G. Van de Walle, *Phys. Rev. Lett.* **85**, 1012 (2000).

[42] K. Iwata, P. Fons, S. Niki, A. Yamada, K. Matsubara, K. Nakahara, and H. Takasu, *Phys. Status Solidi A* **180**, 287 (2000).

[43] D.C. Look, D.C. Reynolds, J.R. Sizelove, R.L. Jones, C.W. Litton, G. Cantwell, and W.C. Harsch, *Solid State Commun*. **105**, 399 (1998).

[44] J. D. Albrecht, P. P. Ruden, S. Limpijumnong, W.R.L. Lambrecht and K.F. Brennan, *J. Appl. Phys.* **86**, 6864 (1999).

[45] Z. Fan and J. Lu, *J. Nanosci. Nanotechnol*. **5**(10), 1561-1573 (2005).

[46] W. II Park, J. S. Kim, G. Yi, M. H. Bae, H.J. Lee, *Appl. Phys. Lett.* **85**, 5052 (2004).

[47] D. Ginley, *Handbook Of Transparent Conductors*. New York: Springer (2010).

[48] M. H. Zhao, Z. L. Wang, S. X. Mao, *Nano Lett.* **4**, 587 (2004).

[49] J. A. Christman, R. R. Woolcott Jr., A. I. Kingon, R. J. Nemanich, *Appl. Phys. Lett.* **73**, 3851 (1998).

[50] J. T. Luo, Y. C. Yang, X. Y. Zhu, G. Chen, F. Zeng, F. Pan, *Phys. Rev. B* **82**, 014116 (2010).

131

[51] Y. C. Yang, C. Song, X. H. Wang, F. Zeng, F. Pan, *Appl. Phys. Lett.* **92**, 012907 (2008).

[52] Z. L. Wang, J. Song, *Science* **312**, 242 (2006).

[53] G. Zhu, R. Yang, S. Wang, Z. L. Wang, *Nano Lett.* **10**, 3151 (2010).

[54] B. Kumar, S. W. Kim, *Nano Energy* **1**, 342 (2012).

[55] C. Xu, P. Shin, L. Cao, D. Gao, *J. Phys. Chem. C* **114**, 125 (2010).

[56] M. Law, L. Greene, J. Johnson, R. Saykally, P. Yang, *Nature Materials* **4**(6), 455 (2005).

[57] K. Takanezawa, K. Hirota, K. Tajima, K. Hashimoto, *J. Phys. Chem. C* **111**, 7218 (2007).

[58] L. M. Chen, Z. Hong, G. Li, Y. Yang, *Adv. Mater.* **21**, 1434 (2009).

[59] D. C. Olson, Y. J. Lee, M. S. White, N. Kopidakis, S. E. Shaheen, D. S. Ginley, J. A. Voigt, J. W. P. Hsu, *J. Phys. Chem. C* **111**, 16640 (2007).

[60] L. Baetem, B. Conings, H. G. Boyen, J. D'Haen, A. Hardy, M. D'Olieslaerger, J. V. Manca, M. K. Van Bael, *Adv. Mater.* **23**, 2802 (2011).

[61] J. Huang, Z. Yin, Q. Zheng, *Energy Environ. Sci.* **4**, 3861 (2011).

[62] S. Hau, H. Yip, N. Baek, J. Zou, K. O'Malley, A. Jen, *Appl. Phys. Lett*. **92**(25), 253301 (2008).

[63] Y. Cheng, C. Hsieh, Y. He, C. Hsu, Y. Li, *J. Am. Chem. Soc*. **132**(49), 17381 (2010).

[64] L. Sang, M. Liao and M. Sumiya, *Sensors* **13**, 10482 (2013).

[65] H. Kind, H. Yan, B. Messer, M. Law, P. Yang, *Adv. Mat.* **14** (2), 158 (2002).

[66] K. Liu, M. Sakurai, M. Aono, *Sensors* **10**, 8604 (2010).

132

[67] E. G. Barbagiovanni, V. Strano, G. Franzò, I. Crupi, S. Mirabella, *Appl. Phys. Lett.* **106**, 093108 (2015).

[68] M. Huang, *Science* **292** (5523), 1897 (2001).

[69] Y. Zhang, M. Ram, E. Stefanakos and D. Goswami, *J. Nanomater.* **2012**, 1 (2012).

[70] M. Spencer, *Progr. Mater. Sci.* **57**, 437 (2012).

[71] J. Wang, X. Sun, Y. Yang, H. Huang, Y. Lee, O. Tan and L. Vayssieres, *Nanotechnology 17*, 4995 (2006).

[72] S. Arya, S. Saha, J. Ramirez-Vick, V. Gupta, S. Bhansali and S. Singh, *Anal. Chim. Acta* **737**, 1 (2012).

[73] A. Fulati, S. Ali, M. Asif, N. Alvi, M. Willander, C. Brännmark, P. Strålfors, S. Börjesson, F. Elinder and B. Danielsson, *Sensors Actuat. B- Chem.* **150**, 673 (2010).

[74] D. Choi, M. Choi, W. Choi, H. Shin, H. Park, J. Seo, J. Park, S. Yoon, S. Chae, Y. Lee, S. Kim, J. Choi, S. Lee and J. Kim, *Adv. Mater.* **22**, 2187 (2010).

[75] F. Tong, K. Kim, D. Martinez, R. Thapa, A. Ahyi, J. Williams, D. Kim, S. Lee, E. Lim, K. Lee and M. Park, *Semicond. Sci. Technol.* **27**,105005 (2012).

[76] G. Hodes, *Phys. Chem. Chem. Phys.* **9**, 2181 (2007).

[77] J. Elias, R. Tena-Zaera, G.Y. Wang, and C. Lévy-Clément, *Chem. Mater.* **20**(21), 6633 (2008).

[78] Y. Y. Xi, Y. F. Hsu, A. B. Djurisic, W. K. Chan, *J. Electrochem. Soc.* **155**(9), D595 (2008).

[79] H. El Belghiti, T. Pauportè, D. Lincot, *Phys. Stat. Sol. (a)* **205** (10), 2360 (2008).

[80] J. Cui, U. Gibson, *Appl. Phys. Lett.* **87**, 133108 (2005).

[81] A. Goux, T. Pauporte, J. Chivot, D. Lincot, *Electrochim. Acta* **50**, 2239 (2005).

[82] Y. Zhang, B. Lin, X. Sun, and Z. Fu, *Appl. Physi. Lett.* **86**(13), 1 (2005).

[83] S. E. Ahn, J. L. Soo, H. Kim, S. Kim, *Appl. Phys. Lett.* **84**(24), 5022 (2004).

[84] S. Alias, A. Mohamad, *Synthesis Of Zinc Oxide By Sol-Gel Method For Photoelectrochemical Cells*, Springer-Verlag Singapur (2014).

[85] K. Govender, D. Boyle, P. Kenway and P. O'Brien, *J. Mater. Chem.* **14**, 2575 (2004).

[86] L. Podrezova, S. Porro, V. Cauda, M. Fontana, G. Cicero, *Appl. Phys. A* **113**, 623 (2013).

[87] P. Baviskar, P. Nikam, S. Gargote, A. Ennaoui and B. Sankapal, *J. Alloys Compd.* **551**, 233 (2013).

[88] L. Schmidt-Mende, J. MacManus-Discroll, *Mater. Today* **10** (5), 40 (2007).

[89] L. Vayssieres, K. Keis, S. E. Lindquist, A. Hagfeldt, *J. Phys. Chem. B* **105**, 3350 (2001).

[90] K. Fujita, K. Murata, T. Nakazawa and I. Kayama, *J.Ceram. Soc. Jpn.* **92**, 81 (1984).

[91] M. Andrès Verges, A. Mifsud, C. J. Serna, *J. Chem. Soc. Faraday Trans.* **86** (6), 959 (1990).

[92] M. Ashfold, R. Doherty, N. Ndifor-Angwafor, D. Riley and Y. Sun, *Thin Solid Films* **515**, 8679 (2007).

[93] L. Greene, B. Yuhas, M. Law, D. Zitoun, P. Yang, *Inorg. Chem.***45**, 7535 (2006).

[94] C. Lokhande, P. Gondkar, R. Mane, V. Shinde and S. Han*, J. All. Comp.* **475**, 304 (2009).

[95] L. Vayssieres, *Adv. Mater.* **15** (5), 464 (2003).

[96] S. Yamabi, H. Imai, *J. Mater. Chem.* **12**, 3773 (2002).

[97] L. Greene, M. Law, J. Goldberger, F. Kim, J. Johnson, Y. Zhang, R. Saykally, P. Yang, *Angew. Chem. Int. Ed.* **42**, 3031 (2003).

[98] C. Pacholski, A. Kornowski, H. Weller, *Angew. Chem. Int. Ed.* 41 (7), 1188 (2002).

[99] S. Baruah, J. Dutta, *J. Sol-Gel Sci. Technol.* **50**, 456 (2009).

[100] H. Ghayour, H. R. Rezaie, Sh. Mirdamadi, A. A. Nourbakhsh, *Vacuum* **86**, 101 (2011).

[101] S. Guillemin, V. Consonni, E. Appert, E. Puyoo, L. Rapenne and H. Roussel, *J. Phys. Chem. C* **116**, 25106 (2012).

[102] S. Guillemin, L. Rapenne, H. Roussel, E. Sarigiannidou, G. Brémond, V. Consonni, *J. Phys. Chem. C* **117**, (2013).

[103] M. Guo, P. Diao and S. Cai, *J. Solid State Chem.* **178**, 1864 (2005).

[104] D. Singh, A. Narasimulu, L. Garcia-Gancedo, Y. Fu, N. Soin, G. Shao, J. Luo, *Nanotechnology* **24**, 275601 (2013).

[105] J. Boercker, J. Schmidt and E. Aydil, *Cryst. Growth Des.* **9**, 2783 (2009).

[106] J.Liu, J. She, S. Deng, J. Chen, N. J. Xu, *Phys. Chem. C* **112**, 11685 (2008).

[107] H. T. Ng, J. Li, M. K. Smith, P. Nguyen, A. Cassel, J. Han, M. Meyyappan, *Science* **300**, 1249 (2003).

[108] X. Wang, Y. Ding, Z. Li, J. Song and Z. Wang, *J. Phys. Chem. C* **113**, 1791(2009).

[109] J. Maeng, G. Jo, M. Choe, W. Park, M. Kwon, S. Park and T. Lee, *Thin Solid Films* **518**, 865 (2009).

[110] C. Ye, Y. Bando, G. Shen and D. Golberg, *J. Phys. Chem. B* **110** (31), 15146 (2006).

[111] J. Cheng, X. Zhang and Z. Luo, *Surf. Coat. Tech.* **202**, 4681 (2008).

[112] S. Gao, H. Li, J. Yuan, Y. Li, X. Yang and J. Liu, *Appl. Surf. Sci.* **256**, 2781 (2010).

[113] Y. Koh, M. Lin, C. Tan, Y. Foo, K. Loh, *J. Phys. Chem. B* **108**, 11419 (2004).

[114] A. Nayak, A. M. Katzenmeyer, Y. Gosho, B. Tekin, M. S. Islam, *Appl. Phys. A: Mater. Sci. Process.* 107, 661 (2012).

[115] Z. Liang, R. Gao, J. Lan, O. Wiranwetchayan, Q. Zhang, C. Li, G. Cao, *Sol. Energ. Mat. Sol. C.* **117**, 34 (2013).

[116] K. McPeak, T. Le, N. Britton, Z. Nickolov, Y. Elabd and J. Baxter, *Langmuir* **27**, 3672 (2011).

[117] J. Qiu, X. Li, W. He, S. Park, H. Kim, Y. Hwang, J. Lee and Y. Kim, *Nanotechnology* **20**, 155603 (2009).

[118] S. Xu and Z. Wang, *Nano Res.* **4**, (2011).

[119] Z. Khusaimi, M. Hafiz Mamat, M. Sahdan, N. Abdullah and M. Rusop, *Defect And Diffusion Forum* **312-315**, 99 (2011).

[120] Y. He, T. Yanagida, K. Nagashima, F. Zhuge, G. Meng, B. Xu, A. Klamchuen, S. Rahong, M. Kanai, X. Li, M. Suzuki, S. Kai and T. Kawai, *J. Phys. Chem. C* **117**, 1197 (2013).

[121] Y. Sun, D. Riley and M. Ashfold, *J. Phys. Chem. B* **110**,15186 (2006).

[122] A. Sugunan, H. Warad, M. Boman and J. Dutta, *J. Sol-Gel Sci. Technol.* **39**, 49 (2006).

[123] L. Greene, M. Law, D. Tan, M. Montano, J. Goldberger, G. Somorjai and P. Yang, *Nano Lett*. **5**, 1231 (2005).

[124] R. L. Penn, J. F. Banfield, *American Mineralogist* **83**, 1077 (1998).

[125] Q. Zhang, S. Liu and S. Yu, *J. Mater. Chem*. **19**, 191 (2009).

[126] D. Chu, T. Hamada, K. Kato and Y. Masuda, *Phys. Status Solidi (A)* **206**, 718 (2009).

[127] D. Polsongkram, P. Chamninok, S. Pukird, L. Chow, O. Lupan, G. Chai, H. Khallaf, S. Park and A. Schulte, *Physica B* **403**, 3713 (2008).

[128] V. Strano, R. Urso, M. Scuderi, K. Iwu, F. Simone, E. Ciliberto, C. Spinella and S. Mirabella, *J. Phys. Chem. C* 118, 28189 (2014).

[129] J. Joo, B. Chow, M. Prakash, E. Boyden and J. Jacobson, *Nature Materials* **10**, 596 (2011).

[130] Z. Ren, Z. P. Huang, J. W. Xu, J. H. Wang, P. Bush, M. P. Siegal, P. N. Provencio, *Science* **282**, 1105 (1998).

[131] C. J. Lee, D. W. Kim, T. J. Lee, Y. C. Choi, Y. S. Park, Y. H. Lee, W. B. Choi,; N. S. Lee, G. S. Park, J. M. Kim, *Chem. Phys. Lett*. **312**, 461 (1999).

[132] W. Shockley, H. J. Queisser, J. Appl. Phys. 32 (3), 510 (1961).

[133] F. Dross, K. Baert, T. Bearda, J. Deckers, V. Depauw, O. El Daif, I.Gordon, A. Gougam, J. Govaerts, S. Granata, R. Labie, X. Loozen, R. Martini, A. Masolin, B. O'Sullivan, Y. Qiu, J. Vaes, D. Van Gestel, J. Van Hoeymissen, A. Vanleenhove, K. Van Nieuwenhuysen, S. Venkatachalam, M. Meuris, J. Poortmans, *Prog. Photovoltaics: Res. Appl*. **20**, 770 (2012).

[134] J. Müller, B. Rech, J. Springer and M. Vanecek, *Solar Energy* **77**, 917 (2004).

137

[135] S. Faÿ, U. Kroll, C. Bucher, E. Vallat-Sauvain and A. Shah, *Sol. Energ. Mat. Sol. Cells* **86**, 385 (2005).

[136] H. P. Wang, D. H. Lien, M. L. Tsai, C. A. Lin, H.C. Chang, K.Y. Laib, J.Ha. He, *J. Phys. Chem. C* **2**, 3144 (2014).

[137] Y. Chao, C. Chen, C. Lin and J. He, *Energy Environ. Sci.* **4**, 3436 (2011).

[138] H. Atwater and A. Polman, *Nat. Mater.* **9**, 205 (2010).

[139] F. Priolo, T. Gregorkiewicz, M. Galli and T. Krauss, *Nat. Nanotechnol.* **9**, 19 (2014).

[140] E. Martins, J. Li, Y. Liu, J. Zhou and T. Krauss, *Phys. Rev. B* **86**, 041404(R) (2012).

[141] P. Kowalczewski, M. Liscidini, L. C. Andreani, *Opt. Lett.* 37 (3), 4868 (2012).

[142] S. Morawiec, M. Mendes, S. Filonovich, T. Mateus, S. Mirabella, H. Águas, I. Ferreira, F. Simone, E. Fortunato, R. Martins, F. Priolo and I. Crupi, *Opt. Express* **22**, A1059 (2014).

[143] R. Tena-Zaera, J. Elias and C. Lévy-Clément, *Appl. Phys. Lett.* **93**, 233119 (2008).

[144] H. Lee, M. Kim and J. Yu, *Nanotechnology* **22**, 445602 (2011).

[145] J. Y. Chen and K. W. Sun, *Sol. Energy Mater. Sol. Cells* **94**, 930–934 (2010).

[146] Y. H. Ko and J. S. Yu, *Opt. Express* **19**, 25935 (2011).

[147] T. Shinagawa, K. Shibata, O. Shimomura, M. Chigane, R. Nomura, and M. Izaki, *J. Mater. Chem. C* **2**, 2908 (2014).

[148] R. E. Nowak, M. Vehse, O. Sergeev, K. von Maydell, and C. Agert, *Sol. Energy Mater. Sol. Cells* **125**, 305 (2014).

[149] V. Strano, E. Smecca, V. Depauw, C. Trompoukis, A. Alberti, R. Reitano, I. Crupi, I. Gordon, S. Mirabella, *Appl. Phys. Lett*. **106**, 013901 (2015).

[150] J. Tauc, *Optical properties and electronic structure of amorphous Ge and Si*, *Mater. Res. Bull.* **3**, 37 (1968).

[151] E. A. Davis and N. F. Mott, *Philos. Mag.* **22** 903 (1970).

[152] B. Viezbicke, S. Patel, B. Davis and D. Birnie, *Phys. Status Solidi B* **252**, 1700 (2015).

[153] V. Srikant and D. Clarke, *J. Appl. Phys*. **83**, 5447 (1998).

[154] Thomas A. Germer, *Modeled Integrated Scattering Tool (MIST)*, Sensor Science Division, National Institute of Standards and Technology, Gaithersburg.

[155] V. Depauw, X. Meng, O. El Daif, G. Gomard, L. Lalouat, E. Drouard, C. Trompoukis, A. Fave, C. Seassal, and I. Gordon, *IEEE J. Photovoltaics* **4**, 215 (2014).

[156] Z. C. Holman, M. Filipiĉ, A. Desceudres, S. De Wolf, F. Smole, M. Topiĉ, and C. Ballif, *J. Appl. Phys.* **113**, 013107 (2013).

[157] Z. C. Holman, M. Filipiĉ, B. Lipovsek, S. De Wolf, F. Smole, M. Topiĉ, and C. Ballif, *Sol. Energy Mater. Sol. Cells* **120**, 426–430 (2014).

[158] G. G. Scapellato, M. Rubino, I. Crupi, S. Di Marco, F. Simone, and S. Mirabella, *J. Appl. Phys*. **114**, 053507 (2013).

[159] K. Iwu, V. Strano, A. Di Mauro, G. Impellizzeri and S. Mirabella, *Cryst. Growth Des.* **15**, 4206 (2015).

[160] A. Eftekhari, *Nanostructured Materials In Electrochemistry*, Wiley-VCH, Weinheim (2008).

[161] M. Michalska-Domańska, M. Norek, W. Stępniowski and B. Budner, *Electrochim. Acta* **105**, 424 (2013).

[162] N. N. Bwana, *J. Nanopart. Res.* **10**, 313 (2008).

[163] R. Abdel-Karim and A. F. Waheed*, Nanocoating, Modern Surface Engineering Treatments*, Dr. M. Aliofkhazraei (2013).

[164] Mayer M: SIMNRA user's guide, report IPP 9/113 Garching: Max-Planck-Institut für Plasmaphysik; 1997.

[165] L. Maiolo, S. Mirabella, F. Maita, A. Alberti, A. Minotti, V. Strano, A. Pecora, Y. Shacham-Diamand, and G.Fortunato, *Appl. Phys. Lett.* **105**, 093501 (2014).

[166] A. Fulati, S. M. Usman Ali, M. Riaz, G. Amin, O. Nur, and M. Willander, *Sensors* **9**, 8911–8923 (2009).

[167] B. S. Kang, F. Ren, Y. W. Heo, L. C. Tien, D. P. Norton, and S. J. Pearton, *Appl. Phys. Lett.* **86**, 112105 (2005).

[168] S. Al-Hilli and M. Willander, *Sensors* **9**, 7445 (2009).

[169] S. M. Al-Hilli, A. Öst, P. Strålfors, and M. Willander, *J. Appl. Phys.* **102**, 084304 (2007).

[170] P.-Y. Yang, J.-L. Wang, P.-C. Chiu, J. C. Chou, C.-W. Chen, H.-H. Li, and H.-C. Cheng, *IEEE Electron Device Lett.* **32**, 1603 (2011).

[171] J.-L. Wang, P.-Y. Yang, T.-Y. Hsieh, C.-C. Huang, and M.-H. Juang, *J. Nanomater.* 2013, 152079.

[172] A. Fujishima, T. N. Rao, and D. A. Tryk, J. *Photochem. Photobiol.* **C1**, 1 (2000).

[173] IUPAC. *Compendium of Chemical Terminology*, 2nd ed. (the "Gold Book"); Compiled by A. D. McNaught, A. Wilkinson, Blackwell Scientific Publications: Oxford, UK (1997).

[174] V. Scuderi, G. Impellizzeri, L. Romano, M. Scuderi, G. Nicotra, K. Bergum, A. Irrera,; B. G. Svensson, V. Privitera, *Nanoscale Res. Lett.* **9**, 458 (2014).

[175] M. N.Chong, B. Jin, C. W. K. Chow, C. Saint, *Water Res.* **44**, 2997 (2010).

Appendix

Effect of Seed Solution Concentration

A study of the effects of the seed solution was carried out by varying the molar concentration of zinc acetate dihydrate in ethanol (1mM, 5 mM, 10mM). In addition, we tried to realize a sample without seeding. Figure A.1 shows the sample grown for 1h in an equimolar (25mM) solution of zinc nitrate hexahydrate and HMTA on Si substrates seeded using different seed solution. Only 5mM zinc acetate dehydrate solution provided a suitable seed layer for the growth of oriented ZnO NRs array.
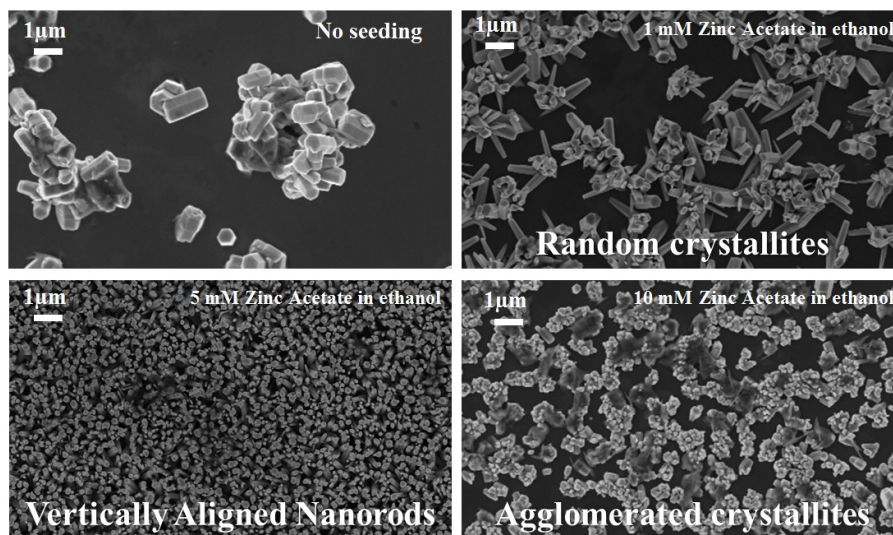
Figure A.1: Sample grown in 25 mM Zinc Nitrate and HMTA solution on substrate seeded using solution with different concentration of zinc acetate dehydrate in ethanol and on unseeded substrate.

Vertical Growth Kinetics of ZnO NRs grown using 50mM HMTA

The vertical growth rate was determined by a linear fit (time range of 0.5-2h) and resulted 13.0 nm/min. The time offset extracted from the data is 7.2 minutes that is about half of that found for the kinetics at 25mM HMTA.
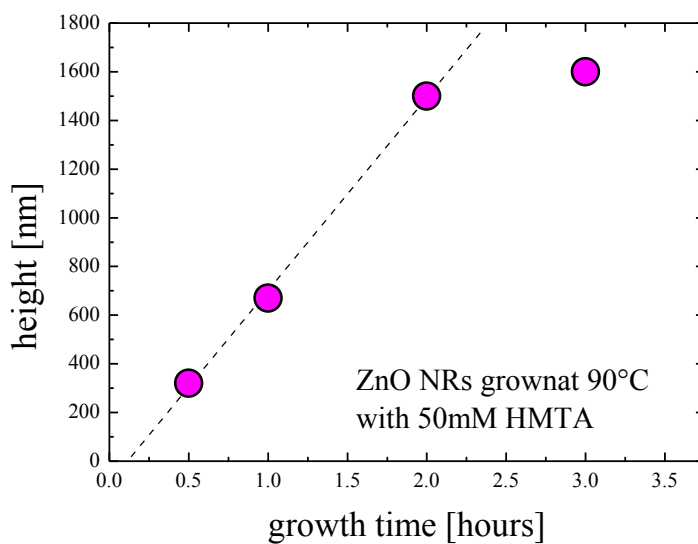
Figure A.2: Time evolution of NRs height grown with 50 mM HMTA concentration (Zn nitrate concentration of 25 mM, temperature of 90 °C, pH = 5.7). Dashed line is the linear fit to extract growth rate and time offset, for data up to 2 h growth time.

144

List of Publications

This thesis is based on the following publications:

- **V. Strano**, E. Smecca, V. Depauw, C. Trompoukis, A. Alberti, R. Reitano, I. Crupi, I. Gordon, S. Mirabella, *Low-cost high-haze films based on ZnO nanorods for light scattering in thin c-Si solar cells*, *Appl. Phys. Lett*. **106**, 013901 (2015).

- K. Iwu, **V. Strano**, A. Di Mauro, G. Impellizzeri and S. Mirabella, *Enhanced Quality, Growth Kinetics, and Photocatalysis of ZnO Nanowalls Prepared by Chemical Bath Deposition*, *Cryst. Growth Des*. **15**, 4206 (2015).

- **V. Strano**, R. Urso, M. Scuderi, K. Iwu, F. Simone, E. Ciliberto, C. Spinella and S. Mirabella, *Double Role of HMTA in ZnO Nanorods Grown by Chemical Bath Deposition*, *J. Phys. Chem. C* **118**, 28189 (2014).

- L. Maiolo, S. Mirabella, F. Maita, A. Alberti, A. Minotti, **V. Strano**, A. Pecora, Y. Shacham-Diamand, and G.Fortunato, *Flexible pH Sensors based on polysilicon thin film transistors and ZnO nanowalls*, *Appl. Phys. Lett.* **105**, 093501 (2014).

Other Publications:

- E. G. Barbagiovanni, R. Reitano, G. Franzò, **V. Strano**, A. Terrasi and S. Mirabella, *Radiative mechanism and surface modification of*

four visible deep level defect states in ZnO nanorods, *Nanoscale* accepted (2015).

- E. G. Barbagiovanni, **V. Strano**, G. Franzò, I. Crupi, and S. Mirabella, *Photoluminescence Transient Study of Surface Defects in ZnO Nanorods grown by Chemical Bath Deposition, Appl. Phys. Lett.* **106**, 093108 (2015).

- L. Maiolo, **V. Strano**, S. Mirabella, F. Maita, A. Minotti, A. Pecora, G. Fortunato, *ZnO nanowalls integrated on ultra-thin flexible TFT based on polysilicon for pH sensing*, in *Nanotechnology Materials and Devices Conference (NMDC), 2014 IEEE 9th* , pp.41-44, 12-15 Oct. 2014

- I. Crupi , S. Boscarino , **V. Strano** , S. Mirabella , F. Simone, A. Terrasi*, Optimization of ZnO:Al/Ag/ZnO:Al Structures for ultra-thin high-performance Transparent Conductive Electrodes*, *Thin Solid Films* **520**, (2012) 4432–4435.

Curriculum Vitae

Vincenzina (Vicky) Strano was born on 9th of June 1982 in Paternò (CT), Italy. She attained her Master Degree in Physics with marks 110/110 from the University of Catania on 11th of December 2011, with a dissertation entitled "Sintesi e caratterizzazione di film sottili AZO/Ag/AZO". In November 2012 she started the Ph.D. course in Science and Technology of Materials at the University of Catania. She is currently working under the supervision of Dr. Salvo Mirabella at the Physics and Astronomy Department of the University of Catania and at the CNR-IMM MATIS group of Catania. The main scientific interests are focused on the synthesis of ZnO nanostructures for photovoltaic and sensing applications. During her Ph.D. course she has been involved in several scientific collaborations with: CNR-IMM, Department of Chemical Sciences of the University of Catania, Tel Aviv University, IMEC- Silicon Photovoltaics (Belgium). She was tutor of the course of Physics for Pharmacists. She presented the results of her research activity, giving both oral or poster contributions, at the following international conferences: 2014 E-MRS spring meeting (Lille), 2014 IEEE nanotechnology materials and devices conference (Acicastello), 2015 E-MRS spring Meeting (Lille), 2015 FISMAT (Italian National Conference on Condensed Matter Physics). She won the graduate student award at 2015 E-MRS spring meeting for the Symposium N: "Synthesis, processing and characterization of nanoscale multi-functional oxide films". She also attended the International School of Solid State Physics on "Materials for Renewable Energy" in 2014. Vincenzina Strano is author or co-author of several articles, published in international referred scientific journals.

Acknowledgments

J.R.R Tolkien's words quoted at the beginning of this thesis, fully express what it means to belong to a community. During these three years of PhD I experienced, once again, how human interaction and relationships have been important to my personal and professional growth.

I would like to thank Prof. Maria Grazia Grimaldi, tutor and coordinator of the PhD, for her availability and support. Heartfelt thanks go to my supervisor Dr. Salvo Mirabella, who guided me, every day, with dynamic enthusiasm, great scientific competence and friendly support. He has always believed in me, pushing me beyond my limits and helping me with valuable advices and encouragements. He initiated the "zinc oxide adventure" that gave me the opportunity to experience the power of the perseverance and the joy of the discovery. Just about zinc oxide, I wish to thank the other components of "ZnO group". My sincere gratitude goes to Dr. Eric Barbagiovanni, example of tireless and passionate researcher, for sharing his scientific knowledge and supporting me with useful suggestions and sincere friendship. Thanks also to Dr. Kingsley Iwu, his expertise and smart intuitions were important for improving my work. I am deeply grateful to Prof. F. Simone who accompanied me for most of this PhD period. With wisdom and kindness, she taught me so much about science and life. A special thanks goes to Prof. Isodiana Crupi for her constant and active scientific support but also for the sincere friendship that she always demonstrated to me.

I want to thank Prof. Francesco Priolo and Prof. Antonio Terrasi, former and current head of CNR- IMM Matis for giving me the possibility to work in this group and to increasing my scientific knowledge. I would like my gratitude to Prof. Enrico Ciliberto, Prof. Riccardo Reitano and Prof. Yosy Shacham- Diamand for enlightening discussion and for providing me original insights within our collaborations. I would like to acknowledge Dr. G. Franzò for her valuable scientific support and Dr. Vittorio Privitera for stimulating conversations and his attentive cordiality. Many thanks to Prof. Lucia Romano for the numerous teachings and to Dr. Simona Boninelli for